# Attitude Control and Dynamics of Solar Sails

Benjamin L. Diedrich

A thesis submitted in partial fulfillment of the requirements for the degree of

Master of Science in Aeronautics & Astronautics

University of Washington

2001

Program Authorized to Offer Degree: Aeronautics & Astronautics

University of Washington

Graduate School

This is to certify that I have examined this copy of a master's thesis by

Benjamin L. Diedrich

and have found that it is complete and satisfactory in all respects,
and that any and all revisions required by the final
examining committee have been made.

Committee Members:

Uy-Loi Ly

Mark Campbell

Date:

University of Washington

Abstract

# Attitude Control and Dynamics of Solar Sails

by Benjamin L. Diedrich

Chair of Supervisory Committee:

Professor Uy-Loi Ly
Aeronautics & Astronautics

Solar sailing is a method of space propulsion whereby radiation pressure from sunlight or artificial sources is used to propel a spacecraft which reflects that radiation. This thesis examines attitude control by means of displacing the center of mass of a solar sail spacecraft with respect to the center of pressure of the sail. The rotational dynamics of this type of solar sail are developed. A simple LQR controller is found by linearizing the sail about an equilibrium point. LQR control is able to provide effective control for the sail even when it is commanded to rotate to an angular position far from the equilibrium point about which the LQR controller was found.

# TABLE OF CONTENTS

# LIST OF FIGURES

# LIST OF TABLES

## ACKNOWLEDGMENTS

There are a number of people I would like to thank for their involvment with this thesis. First and foremost, I want to thank my advisor Professor Uy-Loi Ly for his guidance and patience throughout my research. Colin McInnes [McI99] and Jerome Wright originally pointed out to me the need for research into solar sail attitude control. Professor Mark Campbell gave advice and encouragement during my reasearch. Wanda Frederick, the graduate student coordinator, helped keep me on track to attaining my degree. My many friends among the graduate students in the Aero-Astro department at the U. of Washington were always willing to listen while I voiced concerns over the research. Finally, my parents helped me tremendously throughout my undergraduate and grauate education.

# DEDICATION

To humankind, whose body of knowledge I submit this work into, and which made the creation of this work possible.

# NOMENCLATURE

$(e_1, e_2, e_3)$ Inertial frame for sail attitude dynamics

$(s_1, s_2, s_3)$ Sail body frame

$(c_1, c_2, c_3)$ Control boom body frame

$\phi$ Euler angles between inertial and body frames

$\phi_s$ 2D Euler angle of sail

$\phi_c$ 2D Euler angle of control boom

$(\phi_{s,1}, \phi_{s,2}, \phi_{s,3})$ 3D Euler angles of sail

$(\phi_{c,1}, \phi_{c,2})$ 3D Euler angles of control boom

$(s_1', s_2', s_3')$ Intermediate sail body frame after 1st Euler rotation

$(s_1'', s_2'', s_3'')$ Intermediate sail body frame after 2nd Euler rotation

$(c_1', c_2', c_3')$ Intermediate control boom body frame after 1st Euler rotation

$I_s$ 3D sail inertia tensor

$I_c$ 3D control boom inertia tensor

$w$ Structural boom length

$\sigma_s$ Sail areal density

$\sigma_b$ Structural boom linear density

$l_c$ Control boom length

$\sigma_c$ Control boom linear density

$m_p$ Payload mass

$\vec{r}_s$ Sail position vector

$\vec{q}_s$ Sail generalized coordinate vector

$\vec{r}_c$ Control boom position vector

$\vec{q}_c$ Control boom generalized coordinate vector

$\vec{q}$ System generalized coordinate vector

$l_b$ Distance of control boom center-of-mass from sail center-of-mass

# Chapter 1

## INTRODUCTION

Sailing in the most general sense is the technique of diverting a small portion of a momentum flux for the purpose of propelling a vehicle. Sailing vessels on Earth achieve this with wind sails, which divert a small portion of the massive momentum flux present in moving bodies of air. In space, a vehicle called a solar sail or light sail can achieve the same effect by diverting a small portion of the massive flux of electromagnetic energy put out by the sun as light using large and lightweight mirrored sails. Sunlight has long been known to carry momentum. For almost as long, people such as the Russian space visionary Fridrikh Tsander have envisioned the use of sails for use in space propulsion. Since the 1950s, there has been a wealth of research and papers written on solar sailing. To a large extent, these papers have discussed the orbital dynamics of solar sails and the trajectories they could follow around the sun, planets, and even into interplanetary space. However, very little work has been published on solar sail attitude dynamics. This paper presents an approach for analyzing the attitude dynamics and control of solar sails within the context of a specific, simplified, solar sail design. This is an important field of research because of the dependence of a solar sail trajectory on the attitude of the sail over time. No solar sail has been launched yet, but serious work is progressing in bot the civil and private sectors to launch a solar sail mission. An understanding of the attitude dynamics is essential to making such a mission successful.

Solar sails reflect the incident light falling on them, so that the net force acting on a sail is the vector sum of the forces from the light striking the sail, and the reaction force from the light reflected by the sail. Sails can be made highly reflective ( 85-90%), so that the net force vector has a direction that is close to the vector normal to the sail surface. Therefore, the force acting on the sail is a function of the orientation of the sail normal vector with respect to the incident sunlight. Solar sail trajectories are then determined by the time history of the sail normal vector.

Chapter 2 develops the rotational dynamics of a solar sail spacecraft with a specific attitude control system. The two-dimensional dynamics are developed in full, while the three-dimensional dynamics are developed far enough to illustrate the method. Chapter 3 develops non-linear and linear state models of the solar sail attitude dynamics, and uses the linear model to develop an LQR attitude controller for the angular position of the sail with respect to the incident sunlight. An LQR cost function is developed that will work with a variety of specific sail models. Chapter 4 gives three specific numerical solar sail models of the type specified in chapter 2 and runs them through a series of tests to verify the ability of the attitude controller to respond to reference sail angular position commands and initial conditions. Chapter 5 presents a set of example solar sail trajectories. These trajectories each have a time history of the sail angle required to provide the trajectory. This information and some selected simulations are used to evaluate the ability of the attitude controller to carry out each mission. Finally, chapter 6 summarizes the conclusions regarding the research and offers suggestions for further research.

Appendix A gives a derivation of the inertia tensors used in the example solar sail models. Appendix B gives a full derivation of the two-dimensional orbital dynamics of a solar sail in orbit around the sun. Appendix C briefly describes the optimization method, in particular the cost function, used to calculate the trajectories shown in chapter 5.

# Chapter 2

# ROTATIONAL DYNAMICS

## 2.1 Introduction

The rotational dynamics of a solar sail are developed using Lagrangian dynamics. The procedure involves defining three reference frames - inertial, sail, and control boom, deriving the three-dimensional inertia tensor, then finding the rotational equations of motion. Both the two- and three-dimensional equations of motion are found, but only the two-dimensional case is used for detailed analysis in following chapters. This procedure follows the techniques described in [Ly99b].

The specific solar sail spacecraft modeled consists of a square film of sail material supported by four structural booms radiating from the center. The concept for this spacecraft was detailed by the German aerospace agency, DLR, under the name ODISSEE and is described in [McI99]. Attitude control is provided by a boom with a payload mass on the end extending from the center of the sail. This geometry may be varied, which will change the inertia tensors and acceleration from sunlight. This spacecraft is shown in figure 2.1.

The rotational dynamics of the sail in orbit around the sun are developed using Lagrangian dynamics. They are developed within the reference frames described in section 2.2. One important assumption regarding the reference frames is to assume that the frame $e$ is inertial. This is not actually the case, as the $e$ frame corresponds to the rotating polar reference frame attached to the position of the solar sail spacecraft within the solar system. As the spacecraft travels along its orbit around the sun, the $e$ frame will slowly rotate. However, as the time scale of orbital maneuvers is very

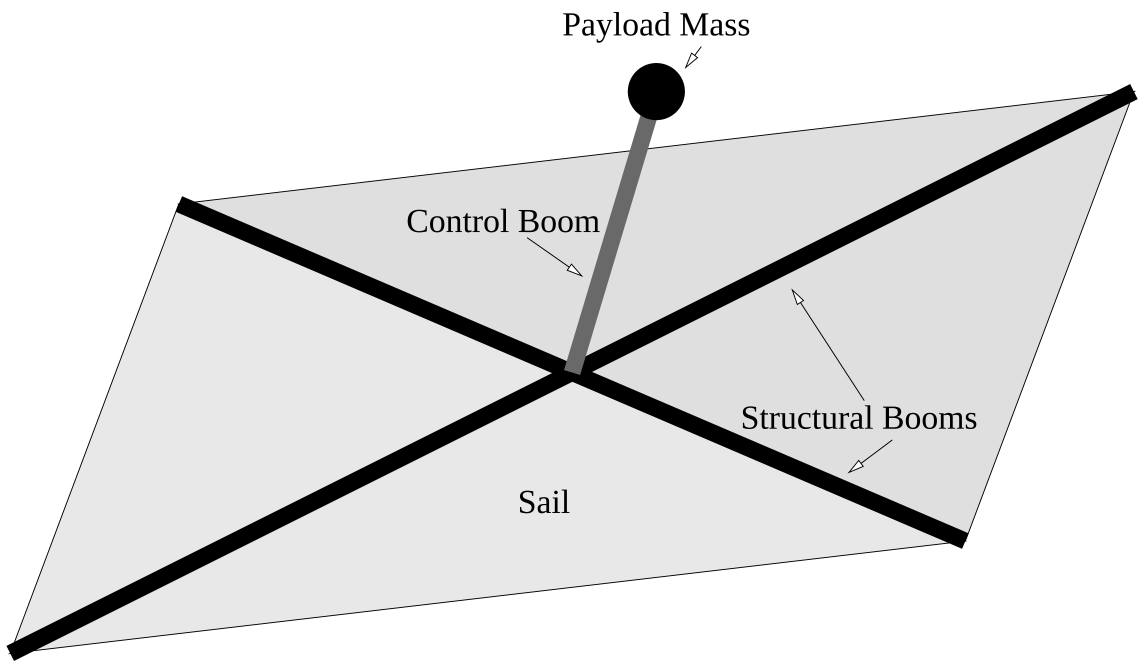


Figure 2.1: Square solar sail spacecraft with control boom

large compared to attitude maneuvers, the contribution of the frame velocities to the dynamics are small enough that they will be neglected in this analysis. Figure 2.2 shows how the inertial frame of the solar system $E$ relates to the polar frame. The orbital dynamics are detailed in appendix B.

The assumption regarding the $e$ frame also leads to the assumption that the only forces acting on the sail are from the sun. Gravity acts in a negative direction along the $e_1$ axis, and solar radiation pressure acts in a positive direction along the same axis. Gravity and solar radiation pressure are both assumed to be inverse square functions of the distance from the sun. More detailed models which differ slightly from this model can be used, but are beyond the scope of this paper. Relativity can be used as more accurate gravitational model. The sun can be treated as a finite disc instead of a point source of sunlight [McI99].

Other assumptions involve the nature of the solar sail spacecraft. The sail is

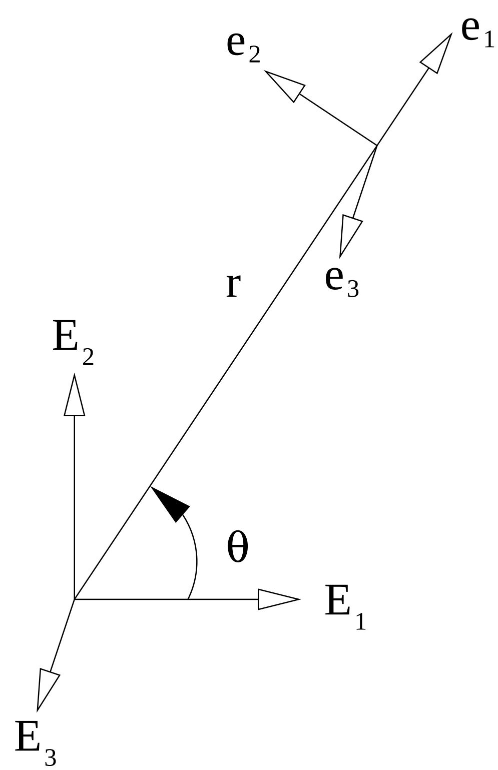


Figure 2.2: Solar system inertial frame $E$ and polar rotating frame $e$

assumed to be perfectly reflecting and perfectly flat, so that the vector sum of the incident and reflected sunlight is normal to the surface of the sail. Flexible dynamics of the sail are not considered. Flexible modes are important, however, due to the large size and light weight of solar sail structures, and may result in low frequency modes that the control system may excite. However, it should be straightforward to introduce flexible modes through careful controller design as discussed in chapter 3.

## 2.2 Reference Frames

The inertial reference frame, sail body frame, and control boom body frame are represented by, respectively, $e$, $s$, and $c$. Angular rotations between the inertial and body frames are represented by $\varphi_s$ for the sail and $\varphi_c$ for the control boom. For the three-dimensional case, $\varphi_s$ and $\varphi_c$ are vectors of the Euler angles.

### 2.2.1 Two-Dimensional Reference Frames

The two-dimensional reference frames are shown in figures 2.3 and 2.4. The angles used for transformation between the inertial and body frames are included in the figures. The angular velocities of the sail and control boom frames are given in equations 2.1 and 2.2, respectively. Together with the transformation operators described in section 2.2.3, this describes the two-dimensional reference frames completely. Again, note that on the scale of the solar system, $e$ is the same frame here as in figure 2.2.

$$\vec{\omega}_s = \dot{\varphi}_s(t)s_3 \tag{2.1}$$

$$\vec{\omega}_c = \dot{\varphi}_c(t)c_3 \tag{2.2}$$

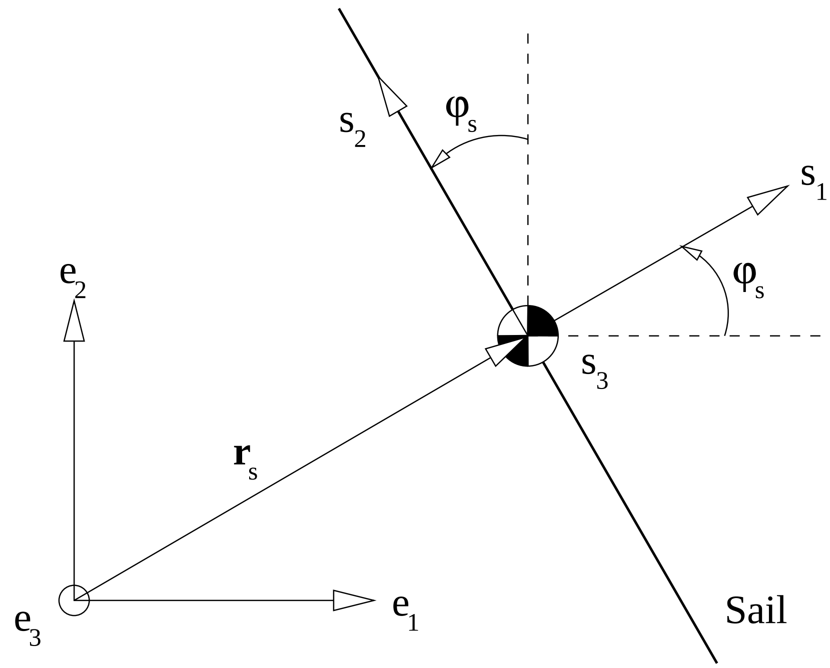


Figure 2.3: 2D inertial and sail reference frames

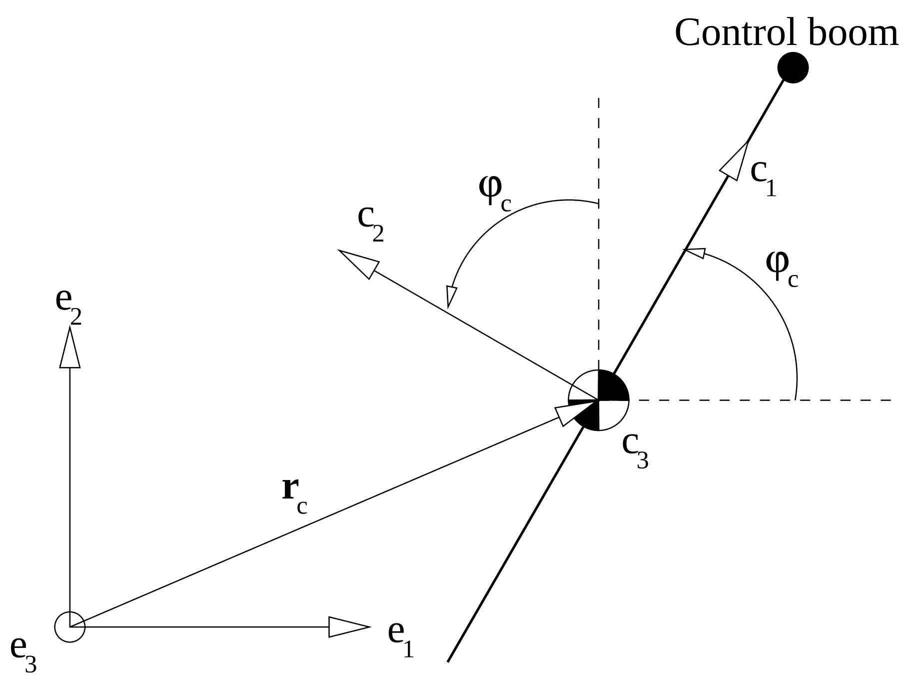


Figure 2.4: 2D inertial and control boom reference frames

### 2.2.2 Three-Dimensional Reference Frames

The three-dimensional reference frames are shown in figures 2.5 and 2.6. The Euler angles to transform between the inertial and body frames are shown in figures 2.7 and 2.8. Intermediate frames are used for the Euler rotations between the inertial frame, $e$, and the body frames, $s$ and $c$. Two intermediate frames are needed for $e$ to $s$, denoted by $s'$ and $s''$, while only one, $c'$, is needed for the transformation from $e$ to $c$.

The angular velocity of the frame is described by the individual angular velocities of each Euler angle as it rotates its respective frame. These angular velocities are given in equations 2.3 and 2.4.

$$\vec{\omega}_s = \dot{\varphi}_{s,1} e_3 + \dot{\varphi}_{s,2} s_2' + \dot{\varphi}_{s,3} s_1'' \tag{2.3}$$

$$\vec{\omega}_c = \dot{\varphi}_{c,1} e_3 + \dot{\varphi}_{c,2} c_2' \tag{2.4}$$

### 2.2.3 Transformations

Transformation between the $e$, $s$, and $c$ reference frames are accomplished via transformation matrices. The matrices, for two and three dimensions, are $C_s$ for the sail frame, and $C_c$ for the control boom frame. The usage of $C_s$ and $C_c$ is that a vector expressed in the $e$ frame, $\vec{r}_e$, can be converted to a vector in the $s$ or $c$ frame, $\vec{r}_s$ or $\vec{r}_c$, by the operation $\vec{r}_s = C_s \vec{r}_e$ or $\vec{r}_c = C_c \vec{r}_e$.

The two-dimensional transformation matrices are simply functions of the single angles, $\varphi_s$ and $\varphi_c$, that the sail and control boom, respectively, are rotated with respect to the inertial frame $e$. The resulting transformation matrices are given in equation 2.5 for the sail and equation 2.6 for the control boom.

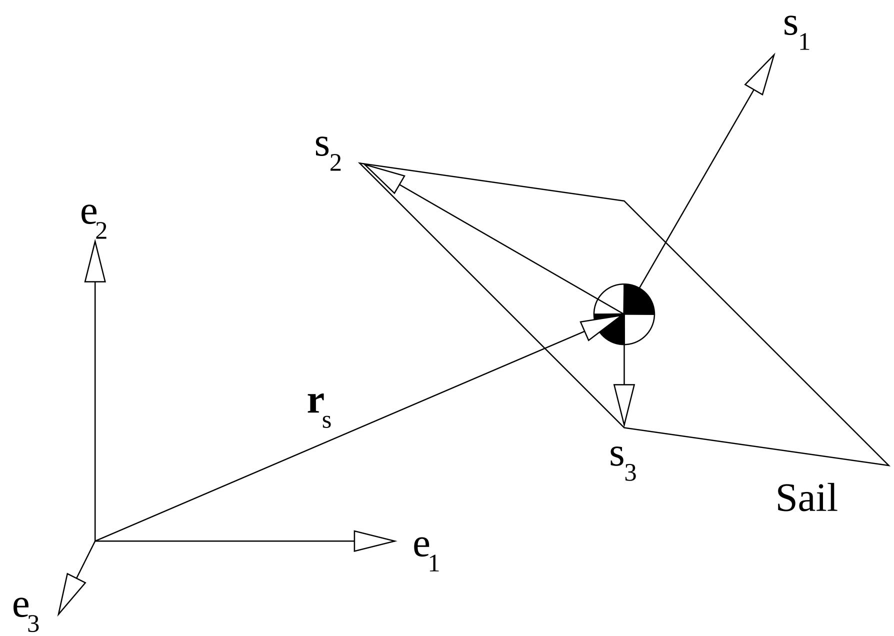


Figure 2.5: 3D inertial and reference frames

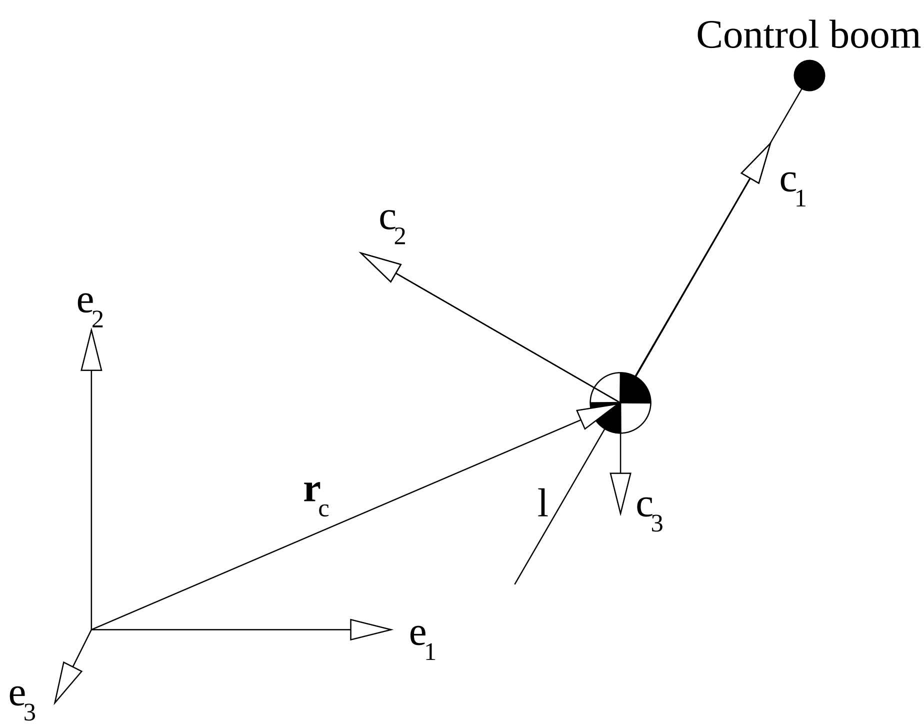


Figure 2.6: 3D inertial and control boom reference frames

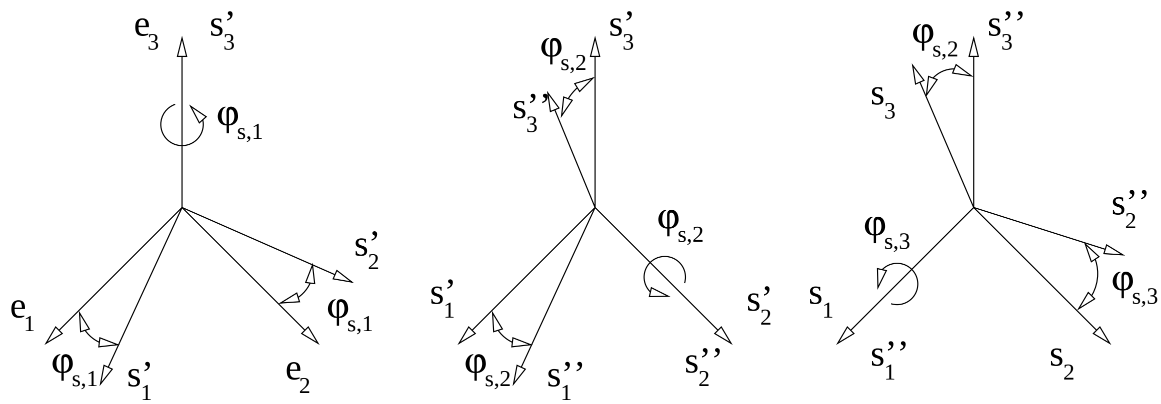


Figure 2.7: Euler angles between inertial frame and sail body frame

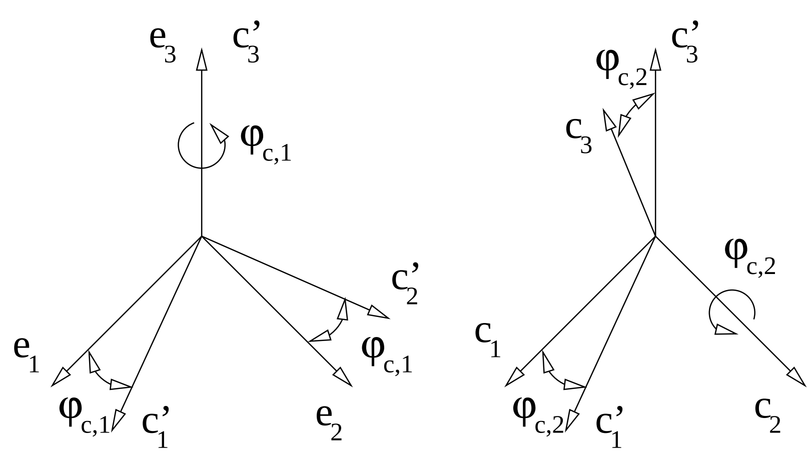


Figure 2.8: Euler angles between inertial frame and control boom body frame

$$C_s = \begin{bmatrix} \cos\varphi_s(t) & \sin\varphi_s(t) & 0 \\ -\sin\varphi_s(t) & \cos\varphi_s(t) & 0 \\ 0 & 0 & 1 \end{bmatrix} \tag{2.5}$$

$$C_c = \begin{bmatrix} \cos\varphi_c(t) & \sin\varphi_c(t) & 0 \\ -\sin\varphi_c(t) & \cos\varphi_c(t) & 0 \\ 0 & 0 & 1 \end{bmatrix} \tag{2.6}$$

The three dimensional transformation matrices are performed by three successive rotations for the sail, as shown in figure 2.7, and two successive rotations for the control boom, which is shown in figure 2.8.

The three successive transformation matrices for the sail frame are given in equations 2.7, 2.8, and 2.9.

$$C_{s,1} = \begin{bmatrix} \cos\varphi_{s,1} & \sin\varphi_{s,1} & 0 \\ -\sin\varphi_{s,1} & \cos\varphi_{s,1} & 0 \\ 0 & 0 & 1 \end{bmatrix} \tag{2.7}$$

$$C_{s,2} = \begin{bmatrix} \cos\varphi_{s,2} & 0 & -\sin\varphi_{s,2} \\ 0 & 1 & 0 \\ \sin\varphi_{s,2} & 0 & \cos\varphi_{s,2} \end{bmatrix} \tag{2.8}$$

$$C_{s,3} = \begin{bmatrix} 1 & 0 & 0 \\ 0 & \cos\varphi_{s,3} & \sin\varphi_{s,3} \\ 0 & -\sin\varphi_{s,3} & \cos\varphi_{s,3} \end{bmatrix} \tag{2.9}$$

These transformations work such that the reference frames transform as $s' = C_{s,1}e$, $s'' = C_{s,2}s'$, and $s = C_{s,3}s''$. Thus, a single transformation from the $e$ to $s$ frame can be formed by the matrix multiplication $C_s = C_{s,3}C_{s,2}C_{s,1}$.

### *2.3 Inertia Tensors*

Complete three-dimensional inertia tensors are developed for the two pieces of the solar sail - the sail (including booms) and the control boom (including payload). The full derivation is given in appendix A.

The derivation assumes that the sail is a very thin flat, square plate with four booms of very thin width extending from the center of the sail to the four corners. Thus, the final sail inertia tensor depends on the areal density of the sail, sail dimensions, linear density of the structural booms, and length of the booms. It is independent of sail thickness and structural boom width.

The control boom inertia tensor is derived under the assumption that the control boom is very thin and that the payload mass at the end of the boom is very small in all dimensions. Thus, the control boom inertia tensor depends only on the linear density of the control boom, control boom length, and mass of the payload. It is independent of control boom width and payload dimensions.

The inertia tensor calculations begin by assuming that all parts (sail, booms, and payload) are rectangular solids for ease of derivation. Then, the assumptions of very small sail thickness, boom width, and payload size simplify the inertia tensor to its final form. Because the sail is extremely thin (1-8 $\mu$m) and the other structural members are very slender, these are valid assumptions. However, the rotational dynamics are developed such that any inertia tensor can be used, with or without simplifying assumptions. These assumptions are used, however, for the example solar sail spacecraft.

The inertia tensor is derived from the fundamental formula for the mass moment of inertia, given in equation 2.10. This integral is carried out over the sail and control boom as described in figures 2.5 and 2.6.

$$I = \int_m r^2 dm \tag{2.10}$$

The resulting inertia tensor of the combined sail film and structural booms is in equation 2.11. The $\sigma_s$ terms correspond to the sail film, while the $\sigma_b$ terms come from the structural booms.

$$I_s = \begin{bmatrix} \frac{2}{3}w^4\sigma_s + \frac{4}{3}w^3\sigma_b & 0 & 0 \\ 0 & \frac{1}{3}w^4\sigma_s + \frac{2}{3}w^3\sigma_b & 0 \\ 0 & 0 & \frac{1}{3}w^4\sigma_s + \frac{2}{3}w^3\sigma_b \end{bmatrix} \tag{2.11}$$

The resulting inertia tensor for the combined control boom and payload in the control boom reference frame is in equation 2.12. The $\sigma_c$ terms refer to the control boom, while the $m_p$ terms come from the payload mass.

$$I_c = \begin{bmatrix} 0 & 0 & 0 \\ 0 & l_c^2 m_p + \frac{1}{3}l_c^3\sigma_c & 0 \\ 0 & 0 & l_c^2 m_p + \frac{1}{3}l_c^3\sigma_c \end{bmatrix} \tag{2.12}$$

## 2.4 Two-dimensional Dynamics

The planar rotational dynamics of the solar sail described in section 2.1 are developed.

### 2.4.1 Reference Frames

The dynamics are developed by starting with the two-dimensional reference frames shown in figures 2.3 and 2.4 and discussed in section 2.2.

### 2.4.2 Position Vectors and Constraints

Next, position vectors and generalized coordinate vectors are defined for the sail and control boom. The position vectors, $\vec{r}_s$ and $\vec{r}_c$, contain coordinates in the $e_1$ and $e_2$ plane of the inertial frame, given as values of $x_{s,1}$, $x_{s,2}$, $x_{c,1}$, and $x_{c,2}$. These vectors are shown graphically in figures 2.3 and 2.4. The generalized coordinate vectors, $\vec{q}_s$

and $\vec{q}_c$, contain these same coordinates, plus the angular positions of the sail and control boom, $\varphi_s$ and $\varphi_c$. Each of these coordinates is a function of time.

The position and generalized coordinate vectors for the sail are given in equations 2.13 and 2.14. The position and generalized coordinate vectors for the control boom are given in equations 2.15 and 2.16. The total generalized coordinate vector is given in equation 2.17.

$$\vec{r}_s = x_{s,1}(t)\, e_1 + x_{s,2}(t)\, e_2 \tag{2.13}$$

$$\vec{q}_s = \begin{bmatrix} x_{s,1}(t) & x_{s,2}(t) & \varphi_s(t) \end{bmatrix} \tag{2.14}$$

$$\vec{r}_c = x_{c,1}(t)\, e_1 + x_{c,2}(t)\, e_2 \tag{2.15}$$

$$\vec{q}_c = \begin{bmatrix} x_{c,1}(t) & x_{c,2}(t) & \varphi_c(t) \end{bmatrix} \tag{2.16}$$

$$\vec{q} = \begin{bmatrix} x_{s,1}(t) & x_{s,2}(t) & \varphi_s(t) & x_{c,1}(t) & x_{c,2}(t) & \varphi_c(t) \end{bmatrix} \tag{2.17}$$

Next, the constraints of the system are defined. The control boom is attached to the center of the sail, with a distance $l_c$ from the control boom center-of-mass to the sail center-of-mass. This sets both the relative positions of the sail and control boom, as well as the orientation of the control boom. The boom must be aligned along the vector describing the difference between the positions of sail and control boom. These requirements define the vector that describes the difference between the control boom and sail positions. This vector must have a magnitude of $l_b$, which is equal to the distance between the center of masses of the control boom and sail. The direction of the vector is the same as the vector that lies along the axis of the boom, $c_1$. This equality constraint ($\vec{g} = 0$) can be described in one vector equation, as given in equation 2.18. Note that this equation can be used in two or three dimensions. The component form of $\vec{g}$ is given in equation 2.19, expressed in the $e$ frame.

$$\vec{g} = \vec{r}_c - \vec{r}_s - l_b\, c_1 = \vec{0} \tag{2.18}$$

$$\begin{aligned}\vec{g} &= \left(-l_b \cos\varphi_c(t) + x_{c,1}(t) - x_{s,1}(t)\right) e_1 + \\ &\quad \left(-l_b \sin\varphi_c(t) + x_{c,2}(t) - x_{s,2}(t)\right) e_2 = \vec{0} \end{aligned} \tag{2.19}$$

In the two-dimensional problem, this will result in two scalar constraint equations, corresponding to the two dimensions of the constraint vector. Thus, two Lagrange multipliers, named $\lambda_1$ and $\lambda_2$, are necessary for the dynamics.

### *2.4.3 Velocity Vectors*

The linear velocities are simply the time derivatives of the positions. The angular velocities are the same as those of the reference frames, in equations 2.1 and 2.2. The linear velocities are given in equations 2.20 and 2.21.

$$\vec{v}_s = \dot{x}_{s,1}(t)\, e_1 + \dot{x}_{s,2}(t)\, e_2 \tag{2.20}$$

$$\vec{v}_c = \dot{x}_{c,1}(t)\, e_1 + \dot{x}_{c,2}(t)\, e_2 \tag{2.21}$$

### *2.4.4 Kinetic Energy*

The kinetic energy is derived from the fundamental formula for rigid bodies. This is given in equation 2.22.

$$T = \frac{1}{2}\, m\, \vec{v} \cdot \vec{v} + \frac{1}{2}\, \vec{\omega} \cdot I\, \vec{\omega} \tag{2.22}$$

The kinetic energy of the sail, control boom, and the sum of the two are given in equations 2.23, 2.24, and 2.25 respectively. Note that the terms $I_{s,3}$ and $I_{c,3}$ are the third elements of the diagonal inertia tensor. These calculations assume a symmetric sail and control boom, so that off-diagonal terms are zero. However, the form given is general and it can be used with any diagonal inertia tensor, not just the tensor described in section 2.3.

$$\begin{aligned}
T_s &= \frac{1}{2}m_s\vec{v}_s\cdot\vec{v}_s + \frac{1}{2}\vec{\omega}_s\cdot I_s\vec{\omega}_s \\
&= \frac{1}{2}m_s\left(\dot{x}_{s,1}^2 + \dot{x}_{s,2}^2\right) + \frac{1}{2}I_{s,3}\dot{\varphi}_s^2 \qquad (2.23)\\
T_c &= \frac{1}{2}m_c\vec{v}_c\cdot\vec{v}_c + \frac{1}{2}\vec{\omega}_c\cdot I_c\vec{\omega}_c \\
&= \frac{1}{2}m_c\left(\dot{x}_{c,1}^2 + \dot{x}_{c,2}^2\right) + \frac{1}{2}I_{c,3}\dot{\varphi}_c^2 \qquad (2.24)\\
T &= T_s + T_c \\
&= \frac{1}{2}m_s\left(\dot{x}_{s,1}^2 + \dot{x}_{s,2}^2\right) + \frac{1}{2}I_{s,3}\dot{\varphi}_s^2 + \frac{1}{2}m_c\left(\dot{x}_{c,1}^2 + \dot{x}_{c,2}^2\right) + \frac{1}{2}I_{c,3}\dot{\varphi}_c^2 \qquad (2.25)
\end{aligned}$$

### *2.4.5 Free-Body Diagram and Forces*

Free-body diagrams of the sail and control boom are shown in figures 2.10 and 2.11. Gravity acts on both bodies, and is a conservative force. Radiation pressure from sunlight acts on the sail and is a non-conservative force.

#### *Gravity*

Gravity is a conservative force, as it varies only with the distance from the sun. Gravity is proportional to the inverse square of the distance from the sun, $r$. The magnitude is the product of the gravitational parameter of the sun, $\mu_s$, and the mass of the body, $m$, which may be the sail, $m_s$, or the control boom, $m_c$. The gravitational force is given by equation 2.26. See B.3 in appendix B for detail.

$$\vec{F}_g = -\frac{\mu_s\, m}{r^2}e_1 \qquad (2.26)$$

The gravitational force will change as the sail moves around the sun if the distance from the sun, $r$, changes. This is accounted for in the trajectory simulations in chapter 4, but for purposes of linearizing the system and calculating an LQR controller for attitude control, $r$ is assumed to be constant over short time periods.

*Radiation Pressure*

This section draws heavily from the "Solar radiation pressure" chapter of [McI99]. Solar radiation pressure is non-conservative because the force produced by the sunlight varies with the angle of the sail as well as the inverse square of the distance from the sun.

Solar radiation pressure arises from the momentum present in any flux of electromagnetic radiation. The momentum carried by a quantity of energy can be derived from the mass-energy equivalence of special relativity. Equation 2.27 shows this relationship, where $E$ is energy, $m_0$ is the rest mass (zero for energy), $c$ is the speed of light, and $p$ is the momentum.

$$E^2 = m_0^2 c^4 + p^2 c^2 \tag{2.27}$$

Taking the time derivative, setting $m_0 = 0$, and dividing through by area gives the simple result shown in equation 2.28, where $P$ is the pressure acting on an object and $W$ is the intensity (power per unit area) of the electromagnetic energy absorbed by the object.

$$P = \frac{W}{c} \tag{2.28}$$

In the case of a solar sail, the force is proportional to the sail area, $A_s$, and the intensity is proportional to the inverse square of the distance from the sun, $r$. The intensity at some reference radius from the sun is given by $W_0$, so that $W = \frac{W_0}{r^2}$. Perfectly reflected sunlight will give an equal and opposite reaction, thus doubling the force and acceleration for a sail oriented normal to the incident sunlight. The force acting on a sail in this orientation can then be given by equation 2.29.

$$\vec{F}_s = \frac{2\, A_s\, W_0}{r^2} e_1 \tag{2.29}$$

A useful way to express solar sail performance is to use the ratio of solar to gravitational forces, which will be called $\beta$. Thus, $\beta$ can be expressed as given in equation 2.30. The nominal magnitude of the force due to sunlight is then given by equation 2.31.

$$\beta = \frac{2\, A_s\, W_0}{\mu_s\, m_s} \tag{2.30}$$

$$\left|\vec{F}_s\right| = \frac{\beta\, \mu_s\, m_s}{r^2} \tag{2.31}$$

The solar force vector, $\vec{F}_{s,r}$, is the vector sum of the sunlight incident on the sail and the sunlight reflected from the sail. Assuming perfect reflection, the magnitude of the incident and reflected sunlight will vary as $e_1 \cdot s_1$ or $\cos\varphi_s(t)$, because the frontal area presented to the sunlight will vary as such with the sails angle with respect to the sunlight.

Figure 2.9 shows how the incident and reflected force vectors add together. $\vec{f_i}$ is the incident sunlight force vector, and $\vec{f_r}$ is the reaction force vector from the reflected sunlight. By the law of cosines, the total radiation pressure force is found to have a magnitude equal to that of the nominal force multiplied by $cos\varphi_s$, which is given in equation 2.32.

$$\vec{F}_{s,r} = \frac{\beta\, \mu_s\, m_s}{r^2} \cos^2\varphi_s(t)\, s_1 \tag{2.32}$$

*Control Moment*

The control input torque, $M(t)$, is applied at the joint between the sail and control boom, for the purposes of rotating the boom to offset the center of gravity from the center of radiation pressure. $M(t)$ acts in a positive polar direction ($\varphi_c$) on the control boom, and a negative direction ($\varphi_s$) on the sail.

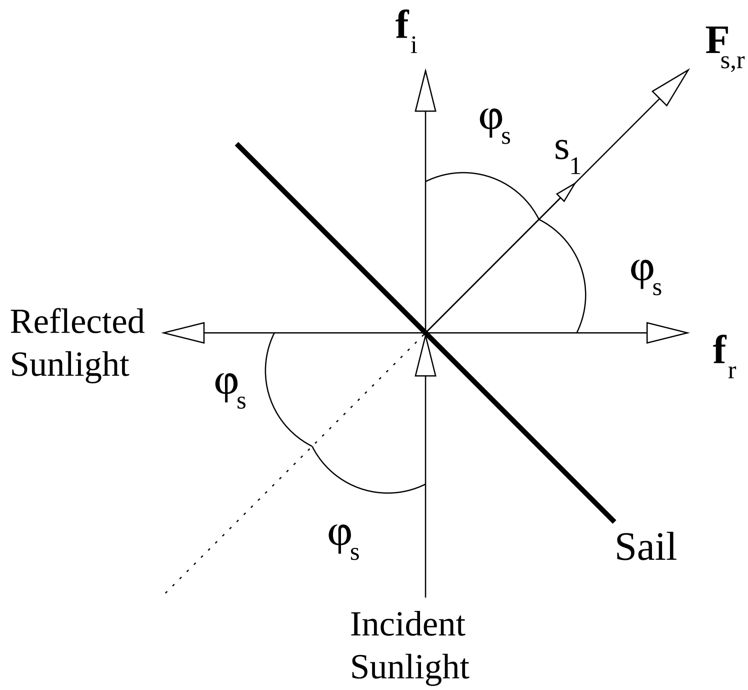


Figure 2.9: Solar radiation pressure force vector

*Total Forces and Moments*

The forces and moments, expressed in the inertial $e$ frame, are shown in equations 2.33, 2.34, 2.35, 2.36, and 2.37.

$$\vec{F}_{s,g} = -\frac{\mu_s m_s}{r^2}\, e_1 \tag{2.33}$$

$$\vec{F}_{c,g} = -\frac{\mu_s m_c}{r^2}\, e_1 \tag{2.34}$$

$$\vec{M}_s = -M(t)\, e_3 \tag{2.35}$$

$$\vec{M}_c = M(t)\, e_3 \tag{2.36}$$

$$\vec{F}_{s,r} = \frac{\beta \mu_s m_s}{r^2} \cos^3 \varphi_s(t)\, e_1 + \frac{\beta \mu_s m_s}{r^2} \cos^2 \varphi_s(t) \sin \varphi_s(t)\, e_2 \tag{2.37}$$

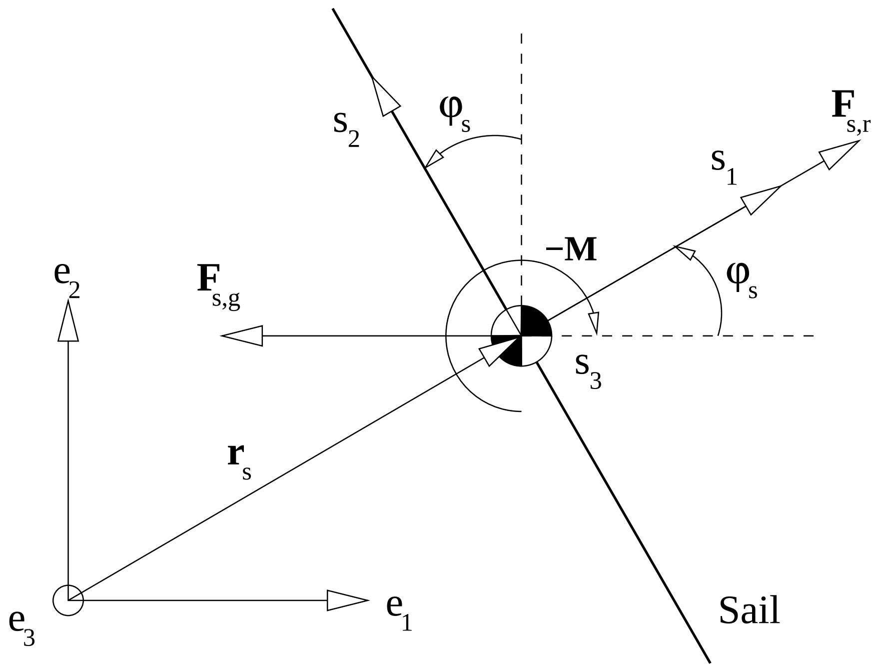


Figure 2.10: 2D sail free-body diagram

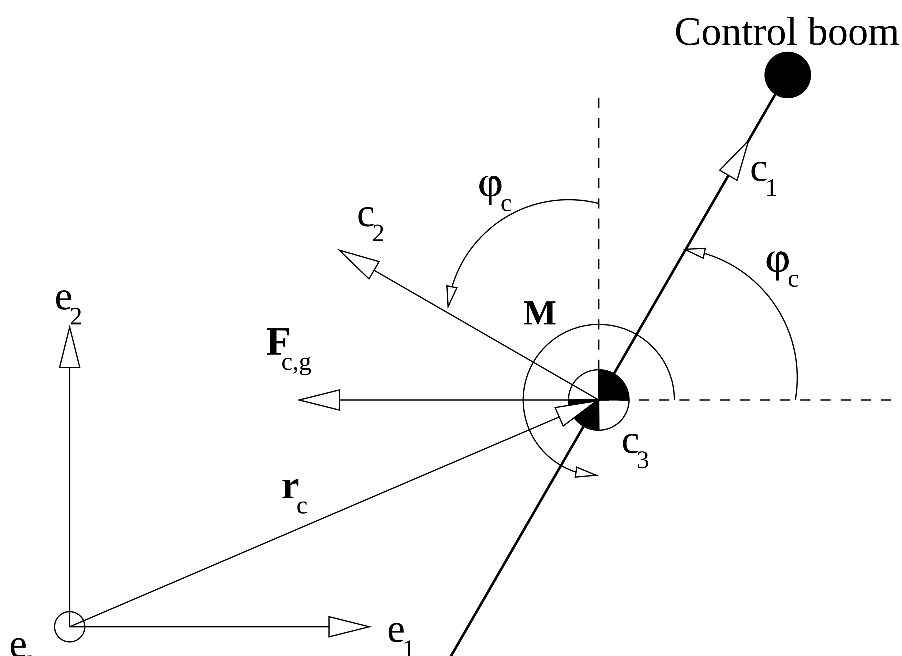


Figure 2.11: 2D control boom free-body diagram

### 2.4.6 Potential Energy

The potential energy is a function of the conservative forces $-\vec{F}_c$ and the position vector $\vec{R}$ over which the conservative force acts. For both the sail and control boom, the conservative force is gravity. The position vector must begin at the source of the conservative force. Because gravity begins at the center of the solar system, $\vec{R}$ must be the sum of the vector from the center of the solar system to the $e$ frame–$r\ e_1$ (see appendix B)–and the position of the sail or control boom in the $e$ frame, $\vec{r}_s$ and $\vec{r}_c$ respectively. The potential energy is calculated using the relation given in equation 2.38.

$$V = -\int \vec{F}_c \cdot \delta\vec{R} \tag{2.38}$$

Because $r\ e_1$ is constant for this problem, the variation $\delta\vec{R}$ is only a function of $\vec{r}_s$ for the sail and $\vec{r}_c$ for the control boom. The potential energy of the sail, control boom, and the total are given in equations 2.39, 2.40, and 2.41.

$$\begin{aligned} V_s &= -\int \vec{F}_{s,g} \cdot \delta\vec{r}_s \\ &= \frac{\mu_s m_s}{r^2}\, x_{s,1}(t) && (2.39) \\ V_c &= -\int \vec{F}_{c,g} \cdot \delta\vec{r}_c \\ &= \frac{\mu_s m_c}{r^2}\, x_{c,1}(t) && (2.40) \\ V &= \frac{\mu_s m_s}{r^2}\, x_{s,1}(t) + \frac{\mu_s m_c}{r^2}\, x_{c,1}(t) && (2.41) \end{aligned}$$

### 2.4.7 Non-Conservative Generalized Force Vector

The non-conservative generalized force vector, $\vec{Q}_{nc}$, is found from the virtual work performed by the non-conservative moments and force $\vec{M}_s$, $\vec{M}_c$, and $\vec{F}_{s,r}$. The virtual work, $\delta W$, done by the non-conservative forces is given in equation 2.42.

$$\begin{aligned}
\delta W &= \vec{F}_{s,r} \cdot \delta \vec{r}_s + \vec{M}_c \cdot \delta \varphi_c e_3 + \vec{M}_s \cdot \delta \varphi_s e_3 \\
&= \frac{\beta \mu_s m_s}{r^2} \cos^3 \varphi_s(t) \delta x_{s,1} + \frac{\beta \mu_s m_s}{r^2} \cos^2 \varphi_s(t) \sin \varphi_s(t) \delta x_{s,2} + \\
& \quad M(t) \delta \varphi_c - M(t) \delta \varphi_s
\end{aligned} \tag{2.42}$$

The general form of $\vec{Q}_{nc}$ is given in equation 2.43. $\vec{Q}_{nc}$ for the two-dimensional solar sail problem is given in equation 2.44

$$\vec{Q}_{nc} = \frac{\delta W}{\delta \vec{q}} \tag{2.43}$$

$$\vec{Q}_{nc} = \begin{bmatrix} \frac{\beta \mu_s m_s}{r^2} \cos^3 \varphi_s(t) \\ \frac{\beta \mu_s m_s}{r^2} \cos^2 \varphi_s(t) \sin \varphi_s(t) \\ -M(t) \\ 0 \\ 0 \\ M(t) \end{bmatrix} \tag{2.44}$$

*2.4.8 Lagrange's Equations of Motion*

The Lagrangian equations of motion are found from the Lagrangian, $\mathcal{L}$, the constraints, $\vec{g}$, and their corresponding Lagrange multipliers, $\vec{\lambda}$, and the generalized non-conservative force vector. The Lagrangian is the difference between the kinetic and potential energies, $\mathcal{L} = T - V$. The formula for Lagrange's equations is given in equation 2.45. The variable $p$ is the number of scalar constraint equations on the system.

$$\frac{\partial \mathcal{L}}{\partial q_k} - \frac{d}{dt}\left(\frac{\partial \mathcal{L}}{\partial \dot{q}_k}\right) + Q_{nc,k} \sum_{j=1}^{p} \lambda_j \frac{\partial g_j}{\partial q_k} = 0\,,\ k = 1 \ldots 6 \tag{2.45}$$

The result of substituting in $T$, $V$, $\vec{g}$, $\vec{\lambda}$, and $\vec{Q}_{nc}$ is given in equations 2.46 through 2.51.

$$
\begin{aligned}
\frac{\beta\mu_s m_s}{r^2}\cos^3\varphi_s(t) - \lambda_1 - \frac{\mu_s m_s}{r^2} - m_s\ddot{x}_{s,1}(t) &= 0 && (2.46)\\
-\lambda_2 + \frac{\beta\mu_s m_s}{r^2}\cos^2\varphi_s(t)\sin\varphi_s(t) - m_s\ddot{x}_{s,2}(t) &= 0 && (2.47)\\
-M(t) - I_{s,3}\ddot{\varphi}_s(t) &= 0 && (2.48)\\
\lambda_1 - \frac{\mu_s m_c}{r^2} - m_c\ddot{x}_{c,1} &= 0 && (2.49)\\
\lambda_2 - m_c\ddot{x}_{c,2} &= 0 && (2.50)\\
-l_b\lambda_2\cos\varphi_c(t) + l_b\lambda_1\sin\varphi_c(t) + M(t) - I_{c,3}\ddot{\varphi}_c(t) &= 0 && (2.51)
\end{aligned}
$$

We are only interested in the angular accelerations, $\ddot{\varphi}_s(t)$ and $\ddot{\varphi}_c(t)$. The solution is found by using these six equations for the six unknown state accelerations, and the two constraint equations for the unknown Lagrange multipliers. This solution is given in equations 2.52 and 2.53.

$$
\begin{aligned}
\ddot{\varphi}_s(t) &= -\frac{M(t)}{I_{s,3}} && (2.52)\\
\ddot{\varphi}_c(t) &= \frac{m_s M(t) + m_c\left[\frac{\beta\mu_s m_s}{r^2} l_b\cos^2\varphi_s(t)\sin\left(\varphi_c(t) - \varphi_s(t)\right) + M(t)\right]}{m_s I_{c,3} + m_c\left(l_b^2 m_s + I_{c,3}\right)} && (2.53)
\end{aligned}
$$

## 2.5 *Three-Dimensional Dynamics*

The three-dimensional dynamics of the solar sail are developed. The same procedure that was used for the two-dimensional case in section 2.4 are used here.

### *2.5.1 Reference Frames*

The three-dimensional reference frames described in section 2.2 are used to develop the dynamics.

### *2.5.2 Position Vectors and Constraints*

As in the two-dimensional case (section 2.4.2), position and generalized coordinate vectors are defined for the sail and control boom. Each position vector, $\vec{r}_s$ and $\vec{r}_c$, has one more term in the $e_3$ direction. The generalized coordinate vector adds two linear position terms for the third dimension of the sail and control boom, two more Euler angles for the sail, and one more Euler angle for the control boom. These terms are represented graphically in figures 2.5, 2.6, 2.7, and 2.8.

The position and generalized coordinate vectors for the sail and control boom are given in equations

$$
\begin{aligned}
\vec{r}_s &= x_{s,1}(t)e_1 + x_{s,2}(t)e_2 + x_{s,3}(t)e_3 && (2.54)\\
\vec{q}_s &= [x_{s,1}(t),\, x_{s,2}(t),\, x_{s,3}(t),\, \varphi_{s,1}(t),\, \varphi_{s,2}(t),\, \varphi_{s,3}(t)] && (2.55)\\
\vec{r}_c &= x_{c,1}(t)e_1 + x_{c,2}(t)e_2 + x_{c,3}(t)e_3 && (2.56)\\
\vec{q}_c &= [x_{c,1}(t),\, x_{c,2}(t),\, x_{c,3}(t),\, \varphi_{c,1}(t),\, \varphi_{c,2}(t)] && (2.57)\\
\vec{q} &= [x_{s,1}(t),\, x_{s,2}(t),\, x_{s,3}(t),\, \varphi_{s,1}(t),\, \varphi_{s,2}(t),\, \varphi_{s,3}(t), \\
&\quad\; x_{c,1}(t),\, x_{c,2}(t),\, x_{c,3}(t),\, \varphi_{c,1}(t),\, \varphi_{c,2}(t)] && (2.58)
\end{aligned}
$$

The three-dimensional constraints use the same generalized constraint on the sail control boom as the two-dimensional case, which is given in equation 2.18. The constraint vector specific to three-dimensions is then found by substituting in the three-dimensional position vectors, giving the result in equation 2.59.

$$
\begin{aligned}
\vec{g} = \; & (x_{c,1}(t) - x_{s,1}(t) - l_b \cos\varphi_{c,2}(t)\cos\varphi_{c,1}(t))\, e_1 + \\
& (x_{c,2}(t) - x_{s,2}(t) - l_b \cos\varphi_{c,2}(t)\sin\varphi_{c,1}(t))\, e_2 + \\
& (x_{c,3}(t) - x_{s,3}(t) + l_b \sin\varphi_{c,2}(t))\, e_3 && (2.59)
\end{aligned}
$$

### *2.5.3 Velocity Vectors*

The three-dimensional velocities are the time derivatives of the positions. These are given in equation 2.60 for the sail and equation 2.61 for the control boom. The angular velocity vectors are given in equations 2.3 and 2.4.

$$\vec{v}_s = \dot{x}_{s,1}(t)e_1 + \dot{x}_{s,2}(t)e_2 + \dot{x}_{s,3}(t)e_3 \tag{2.60}$$

$$\vec{v}_c = \dot{x}_{c,1}(t)e_1 + \dot{x}_{c,2}(t)e_2 + \dot{x}_{c,3}(t)e_3 \tag{2.61}$$

### *2.5.4 Kinetic Energy*

The three-dimensional kinetic energy is found using the same fundamental formula as the two-dimensional case, which is given by equation 2.22. The kinetic energies of the sail, control boom, and total for the three dimensional case are given by equations 2.62, 2.63, and 2.64.

$$\begin{aligned} T_s &= \frac{1}{2}m_s\vec{v}_s \cdot \vec{v}_s + \frac{1}{2}\vec{\omega}_s \cdot I_s\vec{\omega}_s \\ &= \frac{1}{2}m_s\left[\dot{x}_{s,1}^2(t) + \dot{x}_{s,2}^2(t) + \dot{x}_{s,3}^2(t)\right] + \\ &\quad \frac{1}{2}\Big\{I_{s,1}\left[-\sin\varphi_{s,1}(t)\dot{\varphi}_{s,2}(t) + \cos\varphi_{s,1}(t)\cos\varphi_{s,2}(t)\dot{\varphi}_{s,3}(t)\right]^2 + \\ &\quad I_{s,2}\left[\cos\varphi_{s,1}(t)\dot{\varphi}_{s,2}(t) + \sin\varphi_{s,1}(t)\cos\varphi_{s,2}(t)\dot{\varphi}_{s,3}(t)\right]^2 + \\ &\quad I_{s,3}\left[\dot{\varphi}_{s,1}(t) - \sin\varphi_{s,2}(t)\dot{\varphi}_{s,3}(t)\right]^2\Big\} \end{aligned} \tag{2.62}$$

$$\begin{aligned} T_c &= \frac{1}{2}m_c\vec{v}_c \cdot \vec{v}_c + \frac{1}{2}\vec{\omega}_c \cdot I_c\vec{\omega}_c \\ &= \frac{1}{2}m_c\left(\dot{x}_{c,1}^2(t) + \dot{x}_{c,2}^2(t) + \dot{x}_{c,3}^2(t)\right) + \\ &\quad \frac{1}{2}\left[I_{c,1}\sin^2\varphi_{c,1}(t)\dot{\varphi}_{c,2}^2(t) + I_{c,2}\cos^2\varphi_{c,1}\dot{\varphi}_{c,2}^2(t) + I_{c,3}\dot{\varphi}_{c,1}^2(t)\right] \end{aligned} \tag{2.63}$$

$$T = T_s + T_c \tag{2.64}$$

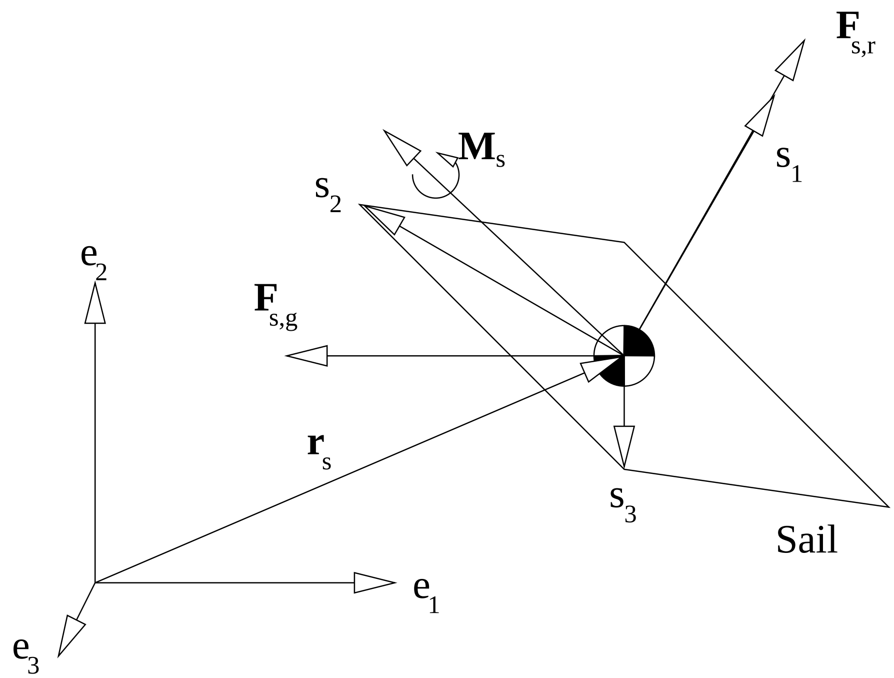


Figure 2.12: 3D Sail Free-Body Diagram

### *2.5.5 Free-Body Diagram and Forces*

Free-body diagrams of the sail and control boom are shown in figures 2.12 and 2.13. Except for being expressed in three-dimensions, these forces are the same as those in the two-dimensional problem.

The conservative forces are gravity acting on the sail and control boom. These follow an identical model to the two-dimensional case, because gravity acts along the $e_1$ axis regardless of whether the problem is two- or three-dimensional.

The non-conservative forces are the solar radiation force acting on the sail and a control moment vector. The solar radiation force is almost identical to the two-dimensional case, in that it acts along the $s_1$ axis. Thus, $\vec{F}_{s,r}$ for the three-dimensional case has the form given in equation 2.32. The only difference is that the $s_1$ axis is different, because of the two additional Euler angles. The control moment vector now has two magnitude components, each of which acts on one of the Euler angles of the

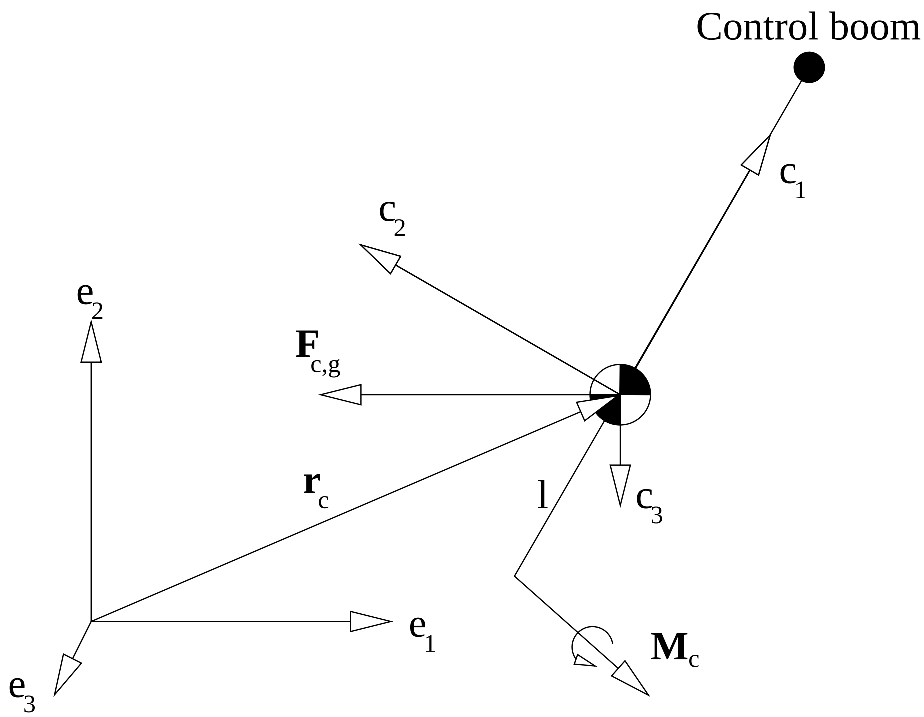


Figure 2.13: 3D Control Boom Free-Body Diagram

control boom. $M_1(t)$ acts on $e_3$, and $M_2(t)$ acts on $c_2'$. An equal and opposite torque acts on the sail. This allows the center of mass of the entire system to be moved over a hemisphere on the side of the sail which the control boom is mounted.

The forces and moments are shown in equations 2.65, 2.66, 2.68, 2.67, and 2.69.

$$
\begin{aligned}
\vec{F}_{s,g} &= -\frac{\mu_s m_s}{r^2}\, e_1 && (2.65)\\
\vec{F}_{c,g} &= -\frac{\mu_s m_c}{r^2}\, e_1 && (2.66)\\
\vec{M}_c &= M_1(t) e_3 + M_2(t) c_2' \\
&= -M_2(t)\sin\varphi_{c,1}(t)\, e_1 + M_2(t)\cos\varphi_{c,2}(t)\, e_2 + M_1(t)\, e_3 && (2.67)\\
\vec{M}_s &= -\vec{M}_c \\
&= M_2(t)\sin\varphi_{c,1}(t)\, e_1 - M_2(t)\cos\varphi_{c,2}(t)\, e_2 - M_1(t)\, e_3 && (2.68)\\
\vec{F}_{s,r} &= \frac{\beta\mu_s m_s}{r^2}\cos^3\varphi_{s,1}(t)\cos^3\varphi_{s,2}(t)\, e_1 + \\
&\quad \frac{\beta\mu_s m_s}{r^2}\cos^2\varphi_{s,1}(t)\cos^3\varphi_{s,2}(t)\sin\varphi_{s,1}(t)\, e_2 + \\
&\quad \frac{\beta\mu_s m_s}{r^2}\cos^2\varphi_{s,1}(t)\cos^2\varphi_{s,2}(t)\sin\varphi_{s,2}(t)\, e_3 && (2.69)
\end{aligned}
$$

### *2.5.6 Potential Energy*

The potential energy of the three-dimensional case is calculated from the general expression given in equation 2.38. As with the gravitational forces, the three-dimensional potential energy terms are identical to the two-dimensional case. The sail, control boom, and total potential energy are given in equations 2.70, 2.71, and 2.72.

$$
\begin{aligned}
V_s &= -\int \vec{F}_{s,g}\cdot\delta\vec{r}_s \\
&= \frac{\mu_s m_s}{r^2}\, x_{s,1}(t) && (2.70)\\
V_c &= -\int \vec{F}_{c,g}\cdot\delta\vec{r}_c \\
&= \frac{\mu_s m_c}{r^2}\, x_{c,1}(t) && (2.71)
\end{aligned}
$$

$$V = \frac{\mu_s m_s}{r^2} x_{s,1}(t) + \frac{\mu_s m_c}{r^2} x_{c,1}(t) \tag{2.72}$$

### *2.5.7 Non-Conservative Generalized Force Vector*

At this point, the three-dimensional calculations become far more cumbersome than the two-dimensional case. As part of this work, the calculations were carried out to their conclusion using Mathematica [mat00]. For this document, however, the rest of the three-dimensional dynamics derivation will be outlined, with important results presented in detail.

The virtual work done by the three-dimensional non-conservative forces and moments is found from equation 2.73.

$$\begin{aligned} \delta W = \; & \vec{F}_{s,r} \cdot \delta \vec{r}_s + \\ & \vec{M}_c \cdot (\delta\varphi_{c,1} e_3 + \delta\varphi_{c,2} c_2') + \\ & \vec{M}_s \cdot (\delta\varphi_{s,1} e_3 + \delta\varphi_{s,2} s_s' + \delta\varphi_{s,3} s_1'') \end{aligned} \tag{2.73}$$

The non-conservative generalized force vector is then found from $\delta W$ using the general equation 2.43. The elements of $\vec{Q}_{nc}$ are given in equations 2.74 to 2.84

$$Q_{nc,x_{s,1}} = \frac{\beta \mu_s m_s}{r^2} \cos^3 \varphi_{s,1}(t) \cos^3 \varphi_{s,2}(t) \tag{2.74}$$

$$Q_{nc,x_{s,2}} = \frac{\beta \mu_s m_s}{r^2} \cos^2 \varphi_{s,1}(t) \cos^2 \varphi_{s,2}(t) \sin \varphi_{s,1}(t) \tag{2.75}$$

$$Q_{nc,x_{s,3}} = -\frac{\beta \mu_s m_s}{r^2} \cos^2 \varphi_{s,1}(t) \cos^2 \varphi_{s,2}(t) \sin \varphi_{s,2}(t) \tag{2.76}$$

$$Q_{nc,\varphi_{s,1}} = -M_1(t) \tag{2.77}$$

$$\begin{aligned} Q_{nc,\varphi_{s,2}} = \; & -M_2(t) \left[\cos \varphi_{c,1}(t) \cos \varphi_{s,1}\right] + \\ & -M_2(t) \left[\sin \varphi_{c,1}(t) \sin \varphi_{s,1}(t)\right] \end{aligned} \tag{2.78}$$

$$\begin{aligned} Q_{nc,\varphi_{s,3}} = \; & M_1(t) \sin \varphi_{s,2}(t) + \\ & M_2(t) \left[\cos \varphi_{s,1}(t) \cos \varphi_{s,2}(t) \sin \varphi_{c,1}(t)\right] + \end{aligned}$$

$$-M_2(t)\left[\cos\varphi_{c,1}(t)\cos\varphi_{s,2}(t)\sin\varphi_{s,1}(t)\right] \quad (2.79)$$

$$Q_{nc,x_{c,1}} = 0 \quad (2.80)$$

$$Q_{nc,x_{c,2}} = 0 \quad (2.81)$$

$$Q_{nc,x_{c,3}} = 0 \quad (2.82)$$

$$Q_{nc,\varphi_{c,1}} = M_1(t) \quad (2.83)$$

$$Q_{nc,\varphi_{c,2}} = M_2(t)\left[\cos^2\varphi_{c,1}(t) + \sin^2\varphi_{c,1}(t)\right] \quad (2.84)$$

### *2.5.8 Lagrange's Equations of Motion*

The equations of motion of the three-dimensional sail are then found from Lagrange's equations as given in equation 2.45.

# Chapter 3

# ATTITUDE CONTROLLER DESIGN

## *3.1 Introduction*

This chapter begins where the chapter on rotational dynamics left off. Chapter 2 finished by developing differential equations describing the angular accelerations of the sail and the control boom. This chapter continues by developing a rotational state model of the sail. The non-linear model is linearized, and the process of developing an LQR controller for the angular position of the sail is detailed.

## *3.2 Model*

The rotational solar sail model is developed using the reference frames and equations of motion from chapter 2. First, a state vector is defined of the angular positions and velocities of the sail. These states are identical to the generalized coordinates of the same name described in equations 2.14 and 2.16. This state vector is given in equation 3.1.

$$\vec{x}(t) = \begin{bmatrix} x_1(t) \\ x_2(t) \\ x_3(t) \\ x_4(t) \end{bmatrix} = \begin{bmatrix} \varphi_s(t) \\ \varphi_c(t) \\ \dot{\varphi}_s(t) \\ \dot{\varphi}_c(t) \end{bmatrix} \tag{3.1}$$

A state model of the form described in equation 3.2 is desired for the solar sail. Note that the model is a linear combination of non-linear functions of the state, $\vec{x}(t)$, and the control, $\vec{u}(t)$. This is a consequence of the solar sail dynamics, as will be shown, and not a simplifying assumption. This helps simplify the process of linearizing the system. The vector functions $\vec{a}$ and $\vec{b}$, which may be non-linear, correspond to the $A$ and $B$ matrices of linear state-space models.

$$\dot{\vec{x}}(t) = \vec{f}(\vec{x}, u, t) = \vec{a}(\vec{x}, t) + \vec{b}(\vec{u}, t) \tag{3.2}$$

### *3.2.1 Nonlinear State Model*

The non-linear state model includes the equations of motion from chapter 2, which are the time rate of change of the angular velocity states, $x_3(t)$ and $x_4(t)$. Added to this are equations for the time rate of change of the angular position states, $x_1(t)$ and $x_2(t)$. Before separating the model into state and control input responses as in equation 3.2, the non-linear model is expressed as in equation 3.3. In the two-dimensional case, $\vec{u}(t)$ is simply the scalar function $M(t)$.

$$\vec{f}(\vec{x}, \vec{u}, t) = \begin{bmatrix} \dot{\varphi}_s(t) \\ \dot{\varphi}_c(t) \\ -\frac{M(t)}{I_{s,3}} \\ \frac{m_s\, M(t) + m_c\left[\frac{\beta\, \mu_s\, m_s}{r^2} l_b \cos^2\varphi_s(t) \sin(\varphi_c(t) - \varphi_s(t)) + M(t)\right]}{m_s\, I_{c,3} + m_c\left(l_b^2 m_s + I_{c,3}\right)} \end{bmatrix} \tag{3.3}$$

The control input, $M(t)$, can be separated out from the state responses. The non-linear model is given once more in equation 3.4 with the control input separated out and represented by $u(t)$, and the states represented by $\vec{x}(t)$. This matches the form of equation 3.2.

$$\vec{f}(\vec{x}, u, t) = \begin{bmatrix} x_3(t) \\ x_4(t) \\ 0 \\ \frac{m_c \frac{\beta\mu_s m_s}{r^2} l_b \cos^2 x_1(t) \sin(x_2(t) - x_1(t))}{m_s I_{c,3} + m_c\left(l_b^2 m_s + I_{c,3}\right)} \end{bmatrix} + \begin{bmatrix} 0 \\ 0 \\ -\frac{1}{I_{s,3}} \\ \frac{m_s + m_c}{m_s I_{c,3} + m_c\left(l_b^2 m_s + I_{c,3}\right)} \end{bmatrix} u(t) \tag{3.4}$$

### 3.2.2 Linearized State Model

The linearized model is found by determining equilibrium points of the non-linear dynamics, then linearizing the dynamics over small displacements in the states using a Taylor series expansion of each state equation. The end result will be the general linear system model given in equation 3.5. Note the similarities to equation 3.2.

$$\dot{\vec{x}}(t) = \vec{f}(\vec{x}, u, t) = A\,\vec{x}(t) + B\,\vec{u}(t) \tag{3.5}$$

The equilibrium points are found by setting $\vec{a}(\vec{x}, u, t) + \vec{b}(u, t) = 0$ and solving for the states. The solution is a set of equilibrium states, $\vec{x}_{eq}$, which are given in equation 3.6.

$$\vec{x}_{eq} = \begin{bmatrix} x_{1,eq} \\ x_{2,eq} \\ x_{3,eq} \\ x_{4,eq} \end{bmatrix} = \begin{bmatrix} x_{1,eq} \\ x_{1,eq} \\ 0 \\ 0 \end{bmatrix} \tag{3.6}$$

Note that $x_1$ ($\varphi_s$) is arbitrary, and that $x_{2,eq} = x_{1,eq}$. This results from the fact that no net torque will act on the sail at any angle so long as the center of mass of the control boom and sail are aligned. The equilibrium control, $u_{eq}$, is equal to zero. Thus, the state equations can be linearized about almost any desired solar sail angle. Note from the non-linear state model (equation 3.4), however, that as $x_{1,eq}$ approaches $\frac{\pi}{2}$, the $\dot{x}_4$ term approaches zero. This will be shown to limit the range of sail angles, $\varphi_s$, that LQR control can handle.

The model is linearized by taking the first order terms of the Taylor series expansion of $\vec{f}(\vec{x}, u, t)$ about $\vec{x}_{eq}$. The series is carried out by the expression in equation 3.7. Note that for this case, $n = 4$, the number of states. Only partial derivatives of $\vec{x}$ are carried out, as $u_{eq} = 0$ and the equations are autonomous, i.e. not functions of the time $t$. $\Delta\vec{x}$ is the variation of $\vec{x}(t)$ away from equilibrium. $\Delta u$ is the variation of $u(t)$

away from equilibrium.

$$f_i(\vec{x},\vec{u},t) \simeq f_i(\vec{x}_{eq},\vec{u}_{eq},t_{eq}) + \sum_{j=1}^{n} \left.\frac{\partial f_i}{\partial x_j}\right|_{\vec{x}=\vec{x}_{eq}} \delta x_j \text{ for i=1...n} \tag{3.7}$$

Carrying out the linearization of equations 3.3 or 3.3 results in the linearized plant model. The initial results are given in equation 3.8. Note that the part of equation 3.4 corresponding to the control input ($\vec{b}(u,t)$) is already linear, so only $\vec{a}(\vec{x},t)$ needs to be linearized.

$$\vec{f}_{lin}(\vec{x},u,t) = \begin{bmatrix} \Delta x_3 \\ \Delta x_4 \\ 0 \\ \frac{m_c l_b \cos^2 x_{1,eq} \frac{\beta\mu_s m_s}{r^2}}{m_s I_{c,3} + m_c\left(l_b^2 m_s + I_{c,3}\right)} (\Delta x_2 - \Delta x_1) \end{bmatrix} + \begin{bmatrix} 0 \\ 0 \\ -\frac{1}{I_{s,3}} \\ \frac{m_s + m_c}{m_s I_{c,3} + m_c\left(l_b^2 m_s + I_{c,3}\right)} \end{bmatrix} \Delta u(t) \tag{3.8}$$

The final model is formed by separating out the $\vec{x}$ vector from the first term of equation 3.8. This result is given in equation 3.9.

$$\begin{aligned} \vec{f}_{lin}(\Delta\vec{x},\Delta u,t) &= \begin{bmatrix} 0 & 0 & 1 & 0 \\ 0 & 0 & 0 & 1 \\ 0 & 0 & 0 & 0 \\ -\frac{m_c l_b \cos^2 x_{1,eq} \frac{\beta\mu_s m_s}{r^2}}{m_s I_{c,3} + m_c\left(l_b^2 m_s + I_{c,3}\right)} & \frac{m_c l_b \cos^2 x_{1,eq} \frac{\beta\mu_s m_s}{r^2}}{m_s I_{c,3} + m_c\left(l_b^2 m_s + I_{c,3}\right)} & 0 & 0 \end{bmatrix} \Delta\vec{x}(t) + \dots \\ & \dots + \begin{bmatrix} 0 \\ 0 \\ -\frac{1}{I_{s,3}} \\ \frac{m_s + m_c}{m_s I_{c,3} + m_c\left(l_b^2 m_s + I_{c,3}\right)} \end{bmatrix} \Delta u(t) \end{aligned} \tag{3.9}$$

For the purposes of this analysis, the $C$ matrix is assumed to be identity, and the $D$ matrix is assumed to be all zeros. Thus, the output $\vec{y}(t)$ is simply equal to $\vec{x}(t)$.

These are given in equation 3.10. Equations 3.9 and 3.10 provide a complete state space description of the linearized rotational dynamics of the solar sail about $\vec{x}_{eq}$.

$$\vec{y}(t) = \begin{bmatrix} 1 & 0 & 0 & 0 \\ 0 & 1 & 0 & 0 \\ 0 & 0 & 1 & 0 \\ 0 & 0 & 0 & 1 \end{bmatrix} \Delta\vec{x}(t) + \begin{bmatrix} 0 \\ 0 \\ 0 \\ 0 \end{bmatrix} \Delta u(t) \tag{3.10}$$

## 3.3 System Analysis

The linear solar sail model given in equations 3.9 and 3.10 is now analyzed to determine controllability, system poles, and system zeros. The techniques used here are described in detail in [Ly00].

### *3.3.1 Controllability*

Controllability is determined from the rank of the controllability matrix. The rank must equal the number of states in the system, which is four for the two-dimensional case. The controllability matrix for the system is built from the state space matrices $A$ and $B$ using equation 3.11. The specific controllability matrix for the solar sail is shown in equation 3.12.

$$\mathcal{C} = \begin{bmatrix} B & A\,B & A^2\,B & A^3\,B \end{bmatrix} \tag{3.11}$$

$$\mathcal{C} = \left[ \begin{matrix} 0 & -\frac{1}{I_{s,3}} \\ 0 & \frac{m_s+m_c}{m_c\left(l_b^2\,m_s+I_{c,3}\right)+I_{c,3}\,m_s} \\ -\frac{1}{I_{s,3}} & 0 \\ \frac{m_s+m_c}{m_c\left(l_b^2\,m_s+I_{c,3}\right)+I_{c,3}\,m_s} & 0 \end{matrix} \right. \quad \cdots$$

$$
\begin{matrix}
\cdots & 0 & \cdots \\
& 0 & \\
& 0 & \\
& \frac{\beta\, l_b\, m_c\, m_s\, \mu_s\, \cos^2 x_{1,eq}}{I_{s,3}\left(m_c\left(l_b^2\, m_s+I_{c,3}\right)+I_{c,3}\, m_s\right) r^2}+\frac{\beta\, l_b\, m_c\, m_s\, (m_s+m_c)\, \mu_s\, \cos^2 x_{1,eq}}{\left(m_c\left(l_b^2\, m_s+I_{c,3}\right)+I_{c,3}\, m_s\right)^2 r^2} & \\
& 0 & \\
\cdots & \frac{\beta\, l_b\, m_c\, m_s\, \mu_s\, \cos^2 x_{1,eq}}{I_{s,3}\left(m_c\left(l_b^2\, m_s+I_{c,3}\right)+I_{c,3}\, m_s\right) r^2}+\frac{\beta\, l_b\, m_c\, m_s\, (m_s+m_c)\, \mu_s\, \cos^2 x_{1,eq}}{\left(m_c\left(l_b^2\, m_s+I_{c,3}\right)+I_{c,3}\, m_s\right)^2 r^2} & \\
& 0 & \\
& 0 &
\end{matrix}
\Bigg] \tag{3.12}
$$

All parameters except $x_{1,eq}$ in the controllability matrix are constants dependent on the solar sail characteristics and the distance from the sun, $r$. At all values of $x_{1,eq}$ except for $\frac{\pi}{2}$, the controllability matrix has a rank of four. At $\frac{\pi}{2}$, the controllability matrix has a rank of only two. Thus, the sail is only uncontrollable when the angular position of the sail is $\frac{\pi}{2}$. This can be clearly seen by looking at $\mathcal{C}$ in equation 3.13.

$$
\mathcal{C}\big|_{x_{1,eq}=\frac{\pi}{2}} = \begin{bmatrix}
0 & -\frac{1}{I_{s3}} & 0 & 0 \\
0 & \frac{m_s+m_c}{m_c\left(l_b^2\, m_s+I_{c3}\right)+I_{c3}\, m_s} & 0 & 0 \\
-\frac{1}{I_{s3}} & 0 & 0 & 0 \\
\frac{m_s+m_c}{m_c\left(l_b^2\, m_s+I_{c3}\right)+I_{c3}\, m_s} & 0 & 0 & 0
\end{bmatrix} \tag{3.13}
$$

This can be explained by the fact that the sail will be edge-on to the sun at $x_{1,eq} = \frac{\pi}{2}$, and not receive any torque from sunlight. However, as can be seen from the non-linear equations of motion (equations 2.52 and 2.53), a torque can be exerted purely from the control boom. Thus, although feedback control as with LQR will not work, we can expect that some form of feed-forward control will allow control of the sail around $x_{1,eq} = \frac{\pi}{2}$. For other values of $x_{1,eq}$ that are sufficiently removed from $\frac{\pi}{2}$, the system is controllable and LQR control can be expected to work.

### 3.3.2 System Poles

The system poles are found by calculating the eigenvalues of the $A$ matrix. This result, called $\vec{\lambda}$, is given in equation 3.14. There is a double-pole at the origin, and two other poles which will either be zero, negative, or positive depending on the value of $x_{1,eq}$. Clearly, a controller is necessary for stability.

$$\vec{\lambda} = \begin{bmatrix} -\frac{\cos x_{1,eq}}{r}\sqrt{\frac{\beta\, l_b\, m_c\, m_s\, \mu_s}{l_b^2\, m_c\, m_s + I_{c,3}\, m_s + I_{c,3}\, m_c}} \\ \frac{\cos x_{1,eq}}{r}\sqrt{\frac{\beta\, l_b\, m_c\, m_s\, \mu_s}{l_b^2\, m_c\, m_s + I_{c,3}\, m_s + I_{c,3}\, m_c}} \\ 0 \\ 0 \end{bmatrix} \tag{3.14}$$

## 3.4 LQR Controller

A linear quadratic regulator (LQR) is now developed to control the solar sail attitude. The technique used is detailed in [Bur99].

### 3.4.1 Implementation

A steady state LQR is found using the linear plant given in equation 3.15 and quadratic cost function given in equation 3.16. Note that the cost function does not use $\vec{y}(t)$, as the $C$ matrix is assumed to be identity from equation 3.10.

$$\dot{\vec{x}}(t) = A\,\vec{x}(t) + B\,\vec{u}(t) \tag{3.15}$$

$$J\left(\vec{x}(t), \vec{u}(t)\right) = \frac{1}{2}\int_0^\infty \left[\vec{x}^T(t)\, Q\, \vec{x}(t) + \rho\, \vec{u}^T(t)\, R\, \vec{u}(t)\right] dt \tag{3.16}$$

The $Q$ and $R$ matrices are chosen to weight the cost of the states and inputs, respectively. The scalar parameter $\rho$ is chosen to weight the states in relation to the control. In the case of the solar sail, $\vec{u}(t)$ is a scalar, so the $R$ matrix is simply a constant.

The $Q$ matrix is chosen to set costs which will retain the states within desired or mechanical limits of the system about equilibrium (equation 3.6). Very tight tolerances are desired on the sail angular position, to ensure accurate pointing of the solar radiation force vector. The control boom can be more relaxed, in order to allow some range of motion to induce control torques. There is a physical limitation of $\frac{\pi}{2}$, to prevent the control boom from impacting the sail. The sail angular velocity should be low, in order to avoid excitation of vibrational modes. The control boom angular velocity can be more relaxed as well to allow for quicker response times.

With these conditions in mind, the $Q$ matrices can be constructed by choosing reasonable maximums. These are given in equation 3.17. It will be shown in the examples that these values will work for a variety of specific solar sail models. An iterative approach was, however, used to verify these results.

$$\begin{bmatrix} \varphi_{s,max} \\ \varphi_{c,max} \\ \dot{\varphi}_{s,max} \\ \dot{\varphi}_{c,max} \end{bmatrix} = \begin{bmatrix} 0.01 \text{ radian} \\ \frac{\pi}{2} \text{ radian} \\ 0.1 \text{ radians/sec} \\ 0.2 \text{ radians/sec} \end{bmatrix} \tag{3.17}$$

From these maxima, the $Q$ matrix is constructed as a diagonal matrix of the inverse squares of the maximum states. This result is shown in equation 3.18.

$$Q = \begin{bmatrix} \frac{1}{\varphi_{s,max}^2} & 0 & 0 & 0 \\ 0 & \frac{1}{\varphi_{c,max}^2} & 0 & 0 \\ 0 & 0 & \frac{1}{\dot{\varphi}_{s,max}^2} & 0 \\ 0 & 0 & 0 & \frac{1}{\dot{\varphi}_{c,max}^2} \end{bmatrix} = \begin{bmatrix} 10000 & 0 & 0 & 0 \\ 0 & \frac{4}{\pi^2} & 0 & 0 \\ 0 & 0 & 100 & 0 \\ 0 & 0 & 0 & 25 \end{bmatrix} \tag{3.18}$$

The value of $R$ and $\rho$ are not so straightforward to find. First, a reasonable maximum torque for the control boom was assumed to be 10 N m ($R = 1/u_{max} = \frac{1}{10}$), and a control weight ($\rho$) of 1 were selected. However, these values resulted in control torques that were much higher than desired when the system was given a step command to the sail and control boom positions. Through the testing discussed in chapter 4, it was found that a very heavy cost on the control was required to keep the control torque below 10 N m for unit step reference commands. The values for $R$ and $\rho$ are shown in equations 3.19 and 3.20.

$$R = 1 \tag{3.19}$$

$$\rho = 100 \tag{3.20}$$

The specific cost function used is then given by equation 3.21.

$$J\left(\vec{x}(t), u(t)\right) = \frac{1}{2}\int_0^{\infty} \vec{x}^T(t) \begin{bmatrix} 10000 & 0 & 0 & 0 \\ 0 & \frac{4}{\pi^2} & 0 & 0 \\ 0 & 0 & 100 & 0 \\ 0 & 0 & 0 & 25 \end{bmatrix} \vec{x}(t) + 100\, u^2(t)\, dt \tag{3.21}$$

The steady-state LQR gain matrix $K$ can then be calculated for specific solar sails from the cost function $J$ and specific system $A$ and $B$ matrices using different techniques, such as the Ricatti equation, an eigenvector solution algorithm of the Hamiltonian system [Bur99], or Schur decomposition [mat99]. The Matlab Control Systems Toolbox [mat99] was used to carry out this calculation in chapter 4 for a number of specific solar sail models. These models are then run through a series of tests to study the effectiveness of the LQR method in controlling a solar sail.

### *3.4.2 Closed Loop System*

The closed-loop system for controlling the sail attitude is now described. The system includes the non-linear system in equation 3.4, the LQR gain matrix, the desired reference input sail position, and the radius from the sun. The block diagram for this system is shown in figure 3.1. Note the conversion factor on the control, u, from any unspecified time unit, TU, to a torque with seconds in the units.

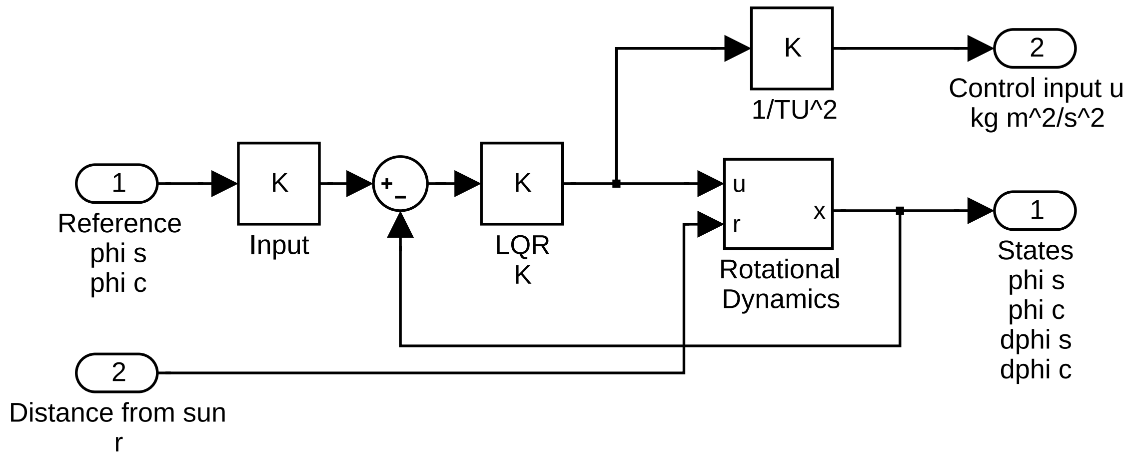


Figure 3.1: Block diagram of 2D closed-loop solar sail rotational dynamics control.

The radius from the sun is actually included as an input for modeling the interaction with the orbital dynamics. This allows the non-linear rotational dynamics to continually change as the radius from the sun changes, even though the LQR gain was found for one particular solar radius.

The reference input allows the desired sail orientation angle to be specified, and for the controller to move the sail to that location. As was seen in equation 3.6, the equilibrium position of the sail is any point where the sail and control boom angular positions are equal. Thus, the reference sail position is applied to both the sail position, $x_1(t)$, and the control boom position, $x_2(t)$. This is achieved by the "Input" block in figure 3.1, which multiplies the reference input, $\varphi_{s,ref}$ $(x_{1,ref})$ by $[1\ 1\ 0\ 0]^T$. The state, $\vec{x}(t)$, is subtracted from the reference, $[x_{1,ref}\ x_{1,ref}\ 0\ 0]^T$, to give the the error which is sent to the controller, $K$.

# Chapter 4

# ATTITUDE CONTROL SIMULATION

## 4.1 Introduction

This chapter runs the solar sail rotational system and LQR controller through a series of test to determine the effectiveness of the LQR method and characterize the behavior of the sail described in chapter 2. Three example solar sail spacecraft are presented and used for the tests. These tests examine the short-term ability of the controller to respond to step reference inputs, initial conditions, and the step response at varying radii from the sun. Chapter 5 examines the ability of the controller to track solar sail trajectories.

## 4.2 Example Solar Sail Spacecraft

Three solar sails models are used for examples. The first is a low-performance (higher mass to area ratio) spacecraft modeled exactly after the ODISSEE spacecraft discussed in [McI99]. The other two models are modified from the first to have lower mass, and thus higher acceleration and lower moments of inertia. Note that the gravitational parameter $\mu_s$ is common to all of the models. The numerical value is $\mu_s = 1.3272\text{E}20\frac{\text{m}^3}{\text{s}^2}$ $(1.3272 \times 10^{20}\frac{\text{m}^3}{\text{s}^2})$.

### *4.2.1 Sail Characteristics*

For each example sail, there is a set of physical characteristics which are used to determine the dynamic model parameters. For example, the lengths and masses of the booms, area and mass of the sail, and payload mass are used to calculate the

| Physical characteristics | |
|---|---|
| Sail area | $A_s$ |
| Sail film mass | $m_{sf}$ |
| Structural boom mass | $m_{sb}$ |
| Payload mass | $m_{cp}$ |
| Control boom mass | $m_{cb}$ |
| Sail reflectivity | $\eta$ |
| Control boom length | $l_b$ |
| **Dynamic model parameters** | |
| Total control boom mass | $m_c : m_{cp} + m_{cb}$ |
| Total sail mass | $m_s : m_{sf} + m_{sb}$ |
| Control boom length | $l_b$ |
| Ratio of solar:gravitational acceleration | $\beta$ |
| Sail moment of inertia about $e_3$ | $I_{s,3}$ |
| Control boom moment of inertia about $e_3$ | $I_{c,3}$ |

inertia tensors using equations 2.11 and 2.12. The total mass of the spacecraft, sail area, and reflectivity are used to determine the performance of each sail, $\beta$, which is the ratio of solar to gravitational acceleration. The physical characteristics and model parameters are listed in table 4.2.1.

The specific values of the physical characteristics and dynamic model parameters are given in table 4.1. As was mentioned previously, there are three example sail models. The first is a low-performance sail, the second is a medium-performance sail, and the third is a high-performance sail. Performance is measured by the area-to-mass ratio, which is reflected by the parameter $\beta$.

Table 4.1: Example solar sail physical characteristics and dynamic model parameters

| Sail performance | Low | Medium | High | Units |
|---|---|---|---|---|
| Physical characteristics | | | | |
| $A_s$ | 1600 | 1600 | 1600 | $m^2$ |
| $m_{sf}$ | 25 | 2.075 | 1 | kg |
| $m_{sb}$ | 11 | 3 | 1.429 | kg |
| $m_{cp}$ | 36 | 5 | 1 | kg |
| $m_{cb}$ | 5 | 1 | 1 | kg |
| $\eta$ | 0.85 | 0.90 | 0.90 | |
| $l_b$ | 10 | 10 | 10 | m |
| Dynamic model parameters | | | | |
| $m_s$ | 36 | 5.070 | 2.429 | kg |
| $m_c$ | 41 | 6 | 2 | kg |
| $l_b$ | 10 | 10 | 10 | m |
| $\beta$ | 0.0272 | 0.200 | 0.500 | |
| $I_{s,3}$ | 4800 | 676.667 | 323.867 | kg $m^4$ |
| $I_{c,3}$ | 3767 | 533.333 | 133.333 | kg $m^4$ |

Table 4.2a: Low Performance Solar Sail State Model and Controller Gain

$$A = \begin{bmatrix} 0 & 0 & 1 & 0 \\ 0 & 0 & 0 & 1 \\ 0 & 0 & 0 & 0 \\ -1.1620\text{E-5} & 1.1620\text{E-5} & 0 & 0 \end{bmatrix} \qquad B = \begin{bmatrix} 0 \\ 0 \\ -2.0833\text{E-4} \\ 1.7595\text{E-4} \end{bmatrix}$$

$$\vec{a}(\vec{x},t) = \begin{bmatrix} x_3(t) \\ x_4(t) \\ 0 \\ 1.509\text{E-7}\cos^2\left(x_2(t) - x_1(t)\right) \end{bmatrix} \qquad \vec{b}(u,t) = \begin{bmatrix} 0 \\ 0 \\ -2.083\text{E-4}\,u(t) \\ 1.759\text{E-4}\,u(t) \end{bmatrix}$$

$$K = \begin{bmatrix} -2.0485 & 12.0487 & 2.6425\text{E3} & 3.5345\text{E3} \end{bmatrix}$$

### *4.2.2 State Models and Controller Gains*

For a majority of the tests, specific sail models are found for an equilibrium position of $\varphi_{s,eq} = \varphi_{c,eq} = 0$ and a radius from the sun of $r = 1$ AU (1.4959965E8 km). The state models (linear and non-linear) and controller gain matrices for the example sails are shown in table 4.2.2. As was discussed in chapter 3, the $C$ and $D$ matrices of the linear model are as given in equation 3.10.

## *4.3 Short-Term Rotational Responses*

The example solar sail systems and controllers in section 4.2 are run through a series of simulations to test the short-term responses to reference input commands and initial conditions. Except for the tests of varying radius from the sun, the tests are performed on sails that are the same distance from the sun as the Earth, that is $r = 1$ AU.

Table 4.2b: Medium Performance Solar Sail State Model and Controller Gain

$$
A = \begin{bmatrix} 0 & 0 & 1 & 0 \\ 0 & 0 & 0 & 1 \\ 0 & 0 & 0 & 0 \\ -8.8025\text{E-}5 & 8.8025\text{E-}5 & 0 & 0 \end{bmatrix} \quad B = \begin{bmatrix} 0 \\ 0 \\ -1.478\text{E-}3 \\ 1.237\text{E-}3 \end{bmatrix}
$$

$$
\vec{a}(\vec{x},t) = \begin{bmatrix} x_3(t) \\ x_4(t) \\ 0 \\ 7.955\text{E-}6\cos^2\left(x_2(t) - x_1(t)\right) \end{bmatrix} \quad \vec{b}(u,t) = \begin{bmatrix} 0 \\ 0 \\ -1.478\text{E-}3\,u(t) \\ 1.237\text{E-}3\,u(t) \end{bmatrix}
$$

$$
K = \begin{bmatrix} -2.139 & 12.140 & 954.166 & 1.2939\text{E}3 \end{bmatrix}
$$

Table 4.2c: High Performance Solar Sail State Model and Controller Gain

$$
A = \begin{bmatrix} 0 & 0 & 1 & 0 \\ 0 & 0 & 0 & 1 \\ 0 & 0 & 0 & 0 \\ -2.440\text{E-}4 & 2.440\text{E-}4 & 0 & 0 \end{bmatrix} \quad B = \begin{bmatrix} 0 \\ 0 \\ -3.088\text{E-}3 \\ 4.115\text{E-}3 \end{bmatrix}
$$

$$
\vec{a}(\vec{x},t) = \begin{bmatrix} x_3(t) \\ x_4(t) \\ 0 \\ 5.510\text{E-}5\cos^2\left(x_2(t) - x_1(t)\right) \end{bmatrix} \quad \vec{b}(u,t) = \begin{bmatrix} 0 \\ 0 \\ -3.088\text{E-}3\,u(t) \\ 4.115\text{E-}3\,u(t) \end{bmatrix}
$$

$$
K = \begin{bmatrix} 0.280 & 9.720 & 738.584 & 622.202 \end{bmatrix}
$$

### *4.3.1 Reference Input Responses*

Three different reference step commands are used to test the controller. Step commands are issued to the sail and control boom positions of 0.2, 0.5, and 1 radian. Also, tests with ramp inputs up to a final reference value of 1 radian were performed to improve the sail position overshoot with the 1 radian step input. This is to test how well the controller is able to respond to small, medium, and large reference inputs. This also tests the ability of the controller to operate very far from the equilibrium position at which the system was linearized for generating the LQR gain matrix.

For each test, the reference input begins at 1000 seconds. Each figure represents a single test, with three plots showing the angular position of the sail and control boom compared to the reference input, the angular velocities, and the control torque output by the controller.

#### *Small Reference Input* - $\varphi_{s,ref} = \varphi_{c,ref} = 0.2$ *radian*

The low performance sail ($\beta = 0.0272$) responses are shown in figure 4.1. The response shows that the control boom moves initially towards the desired direction, and the sail reacts by rotating in the opposite direction. This shows that no net change in the equilibrium position can be accomplished by the control boom alone. To accomplish a net change in the equilibrium position ($\varphi_s = \varphi_c$), the control boom must be positioned out of line with the sail for an extended period of time. This creates an offset between the center-of-pressure of the sail and the center-of-mass of the whole spacecraft that allows the equilibrium position to change. This response will be seen to be characteristic of all the step input responses. The control torque is well within the limit of 10 N m used for the cost function, the angular velocities are kept low, and the sail and control boom angular positions move to the reference input within $\approx$ 2000 seconds without overshoot.

The medium performance solar sail ($\beta = 0.2$) response is shown in figure 4.2.

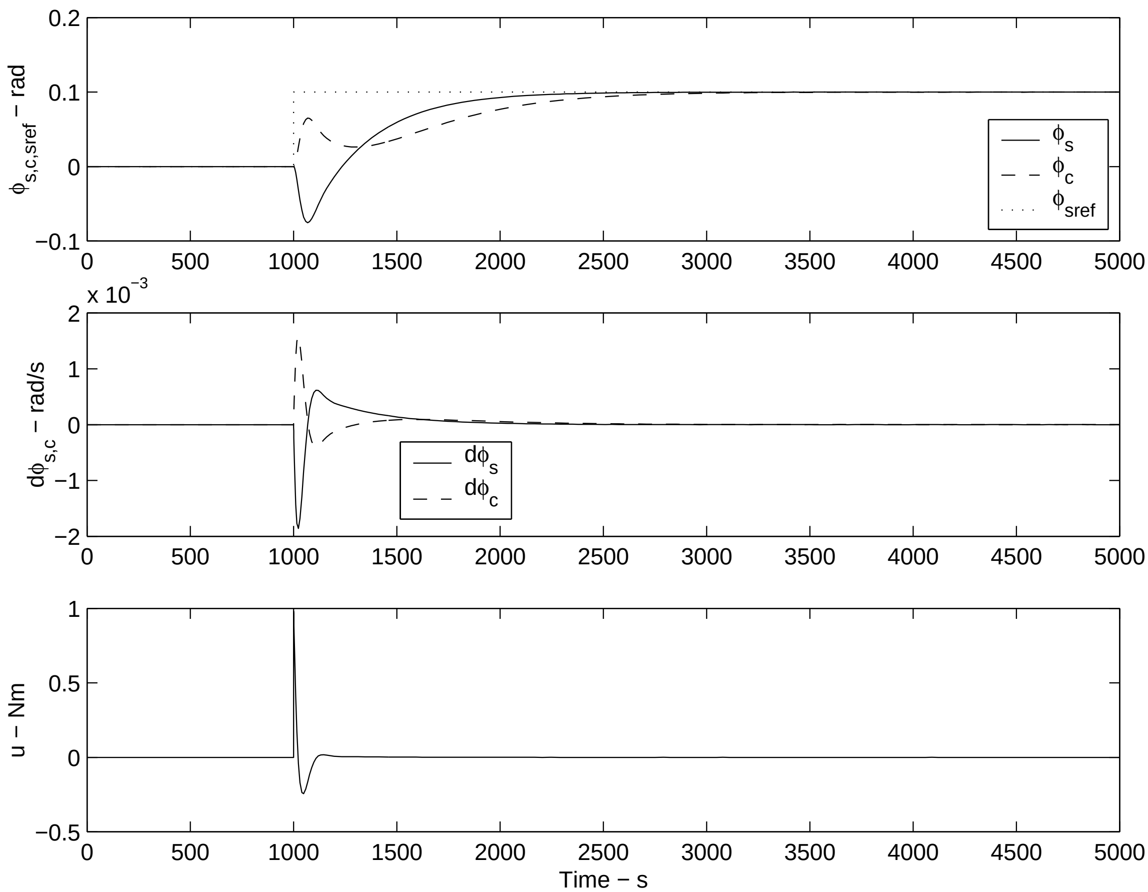


Figure 4.1: Low performance solar sail responses to 0.2 radian step input

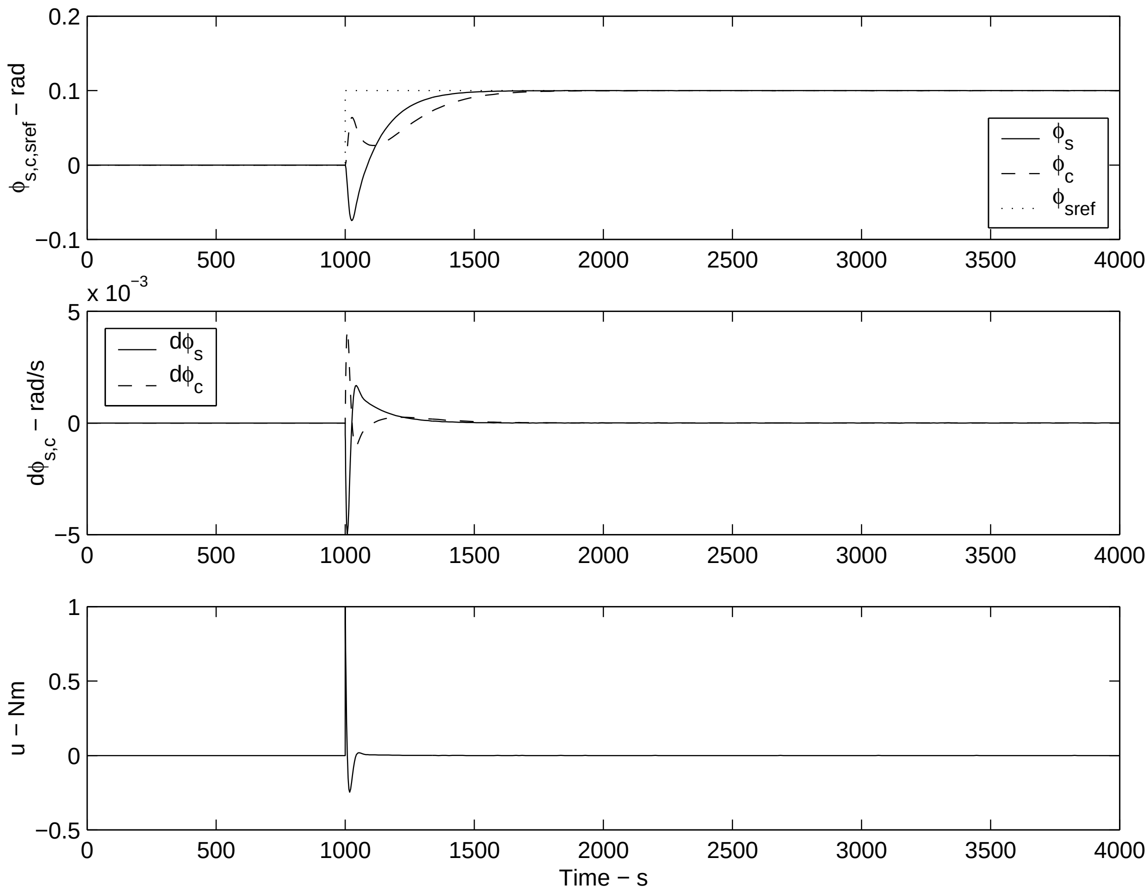


Figure 4.2: Medium performance solar sail responses to 0.2 radian step input

Aside from a quicker response time (< 1000 seconds), the response is very similar to that of the low performance sail.

The high performance solar sail ($\beta = 0.5$) response is shown in figure 4.3. Again, the response is similar, except for a $\approx 600$ second response time.

*Medium Reference Input* - $\varphi_{s,ref} = \varphi_{c,ref} = 0.5$ *radian*

The low performance sail responses are shown in figure 4.4. Like the 0.2 radian response, the control is smooth with no overshoot The angular velocities are a little larger, and the control torque is about 5 times larger, but they are still well within the

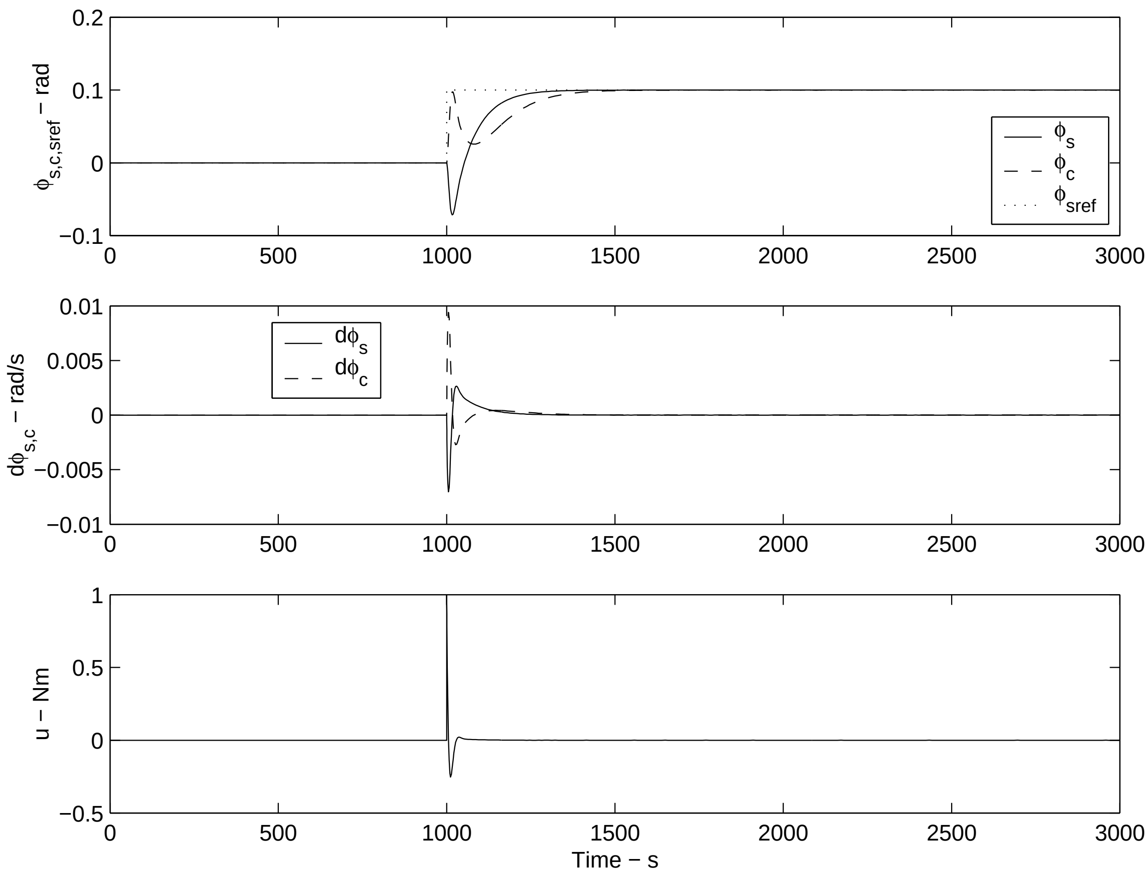


Figure 4.3: High performance solar sail responses to 0.2 radian step input

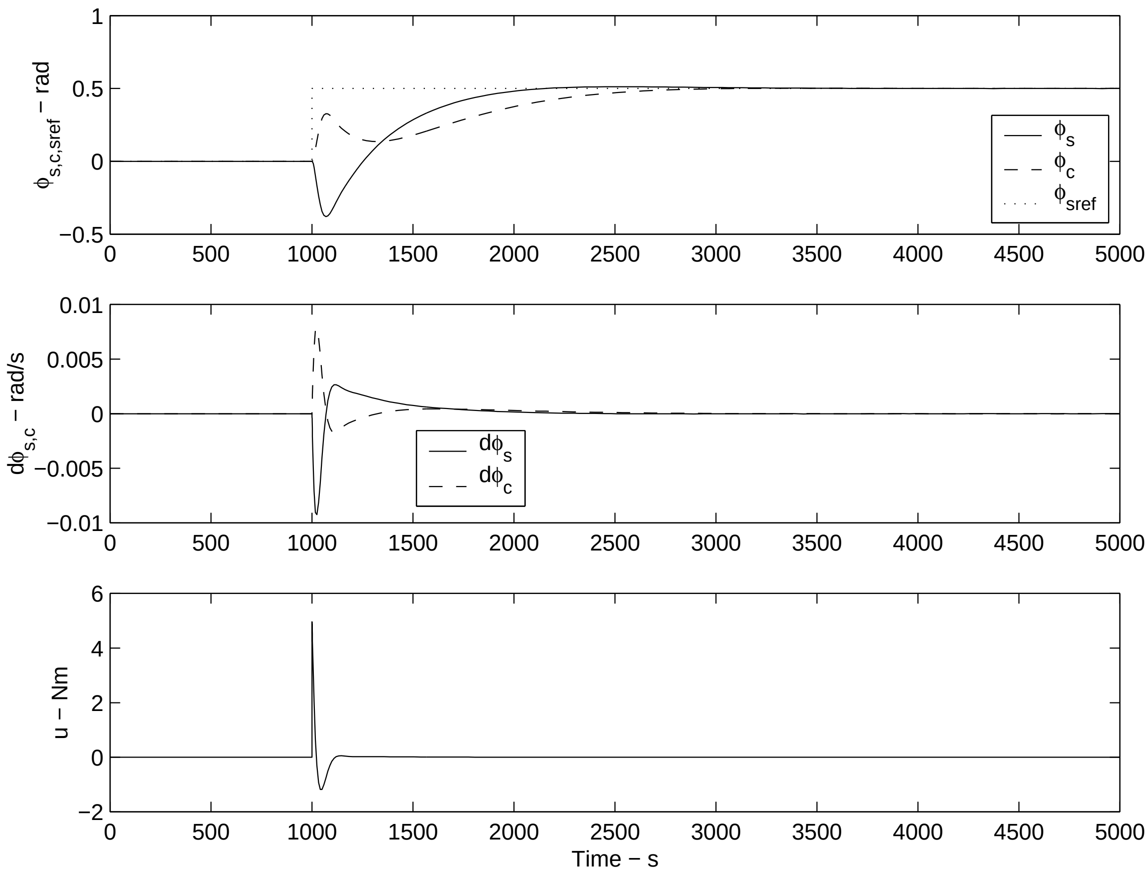


Figure 4.4: Low performance solar sail responses to 0.5 radian step input

tolerances used for the cost function. Note that this represents a significant departure from the equilibrium ($\varphi_s = \varphi_c = 0$) about which the system was linearized, but that the controller is still functioning without any apparent problems.

The medium performance sail responses are shown in figure 4.5. Like the response to a 0.2 radian step input, the response is similar except for the response time.

The high performance responses are shown in figure 4.6. Again, the response is similar except for a quicker rise time.

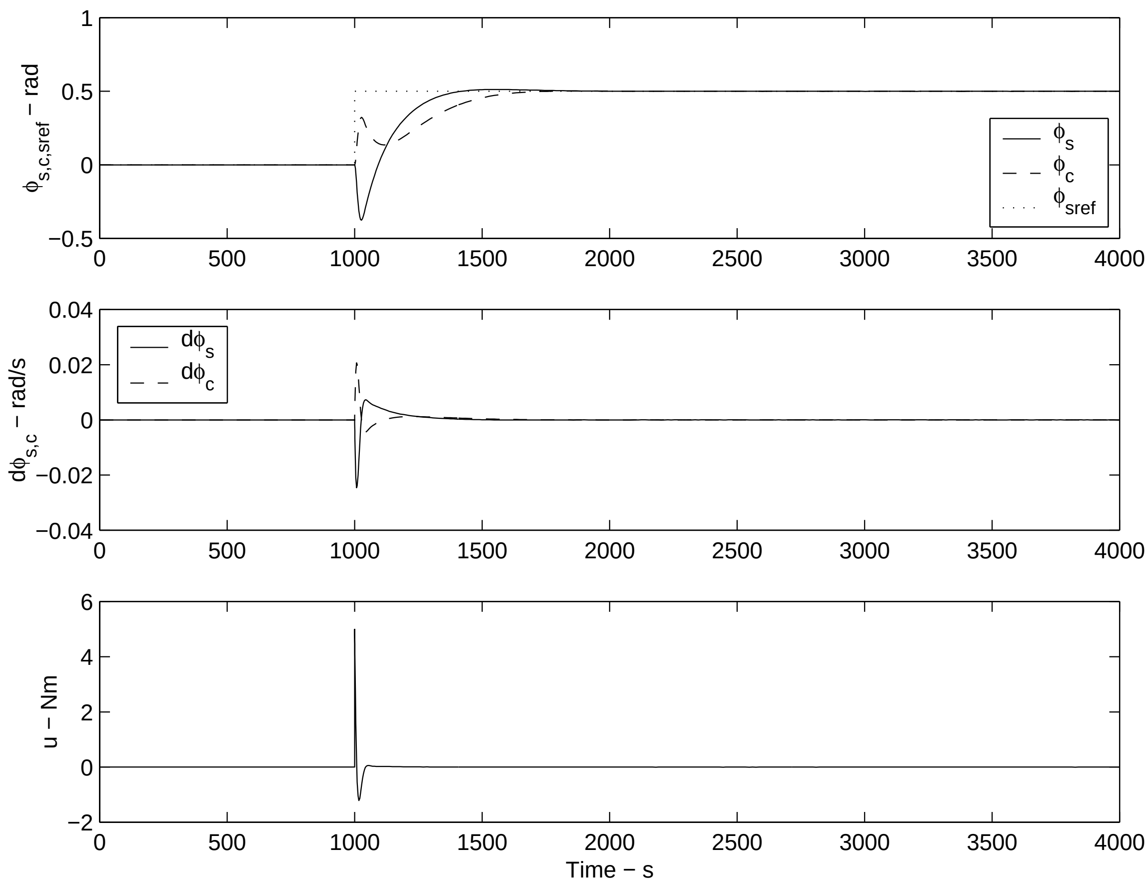


Figure 4.5: Medium performance solar sail responses to 0.5 radian step input

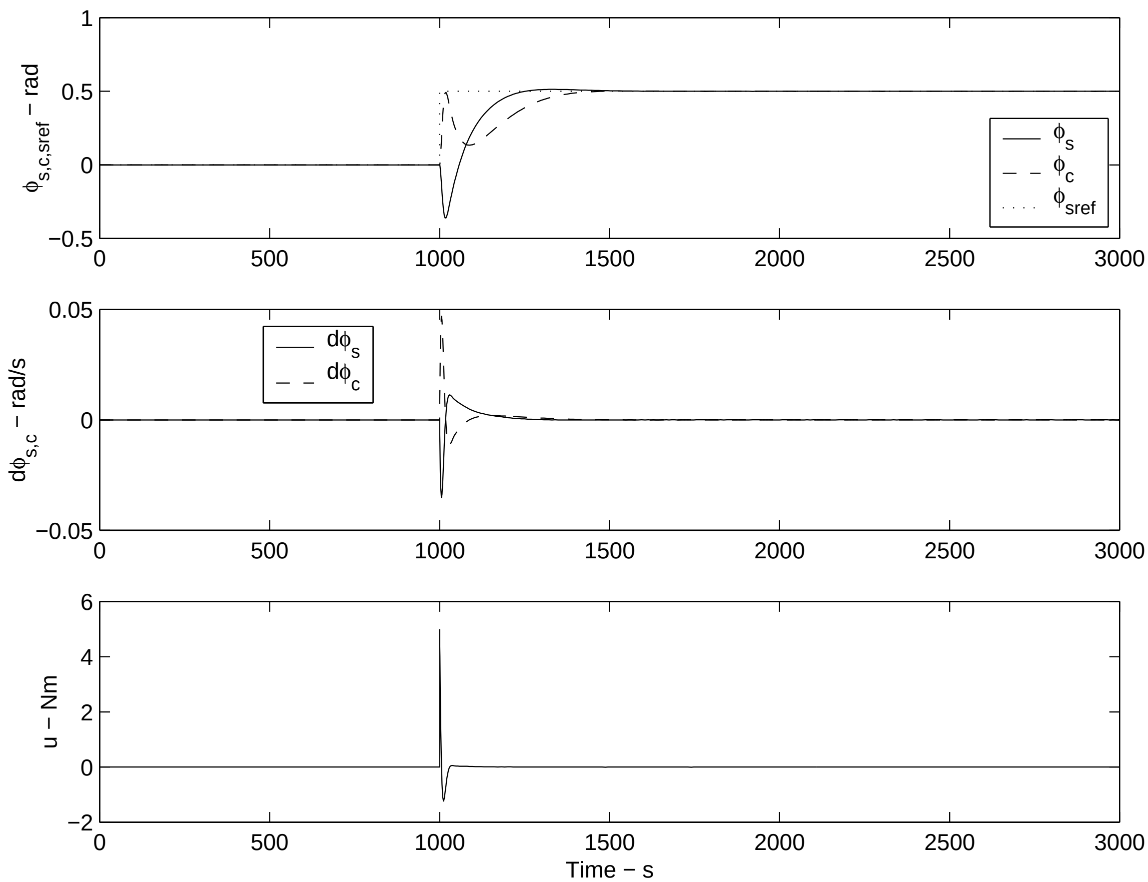


Figure 4.6: Low performance solar sail responses to 0.5 radian step input

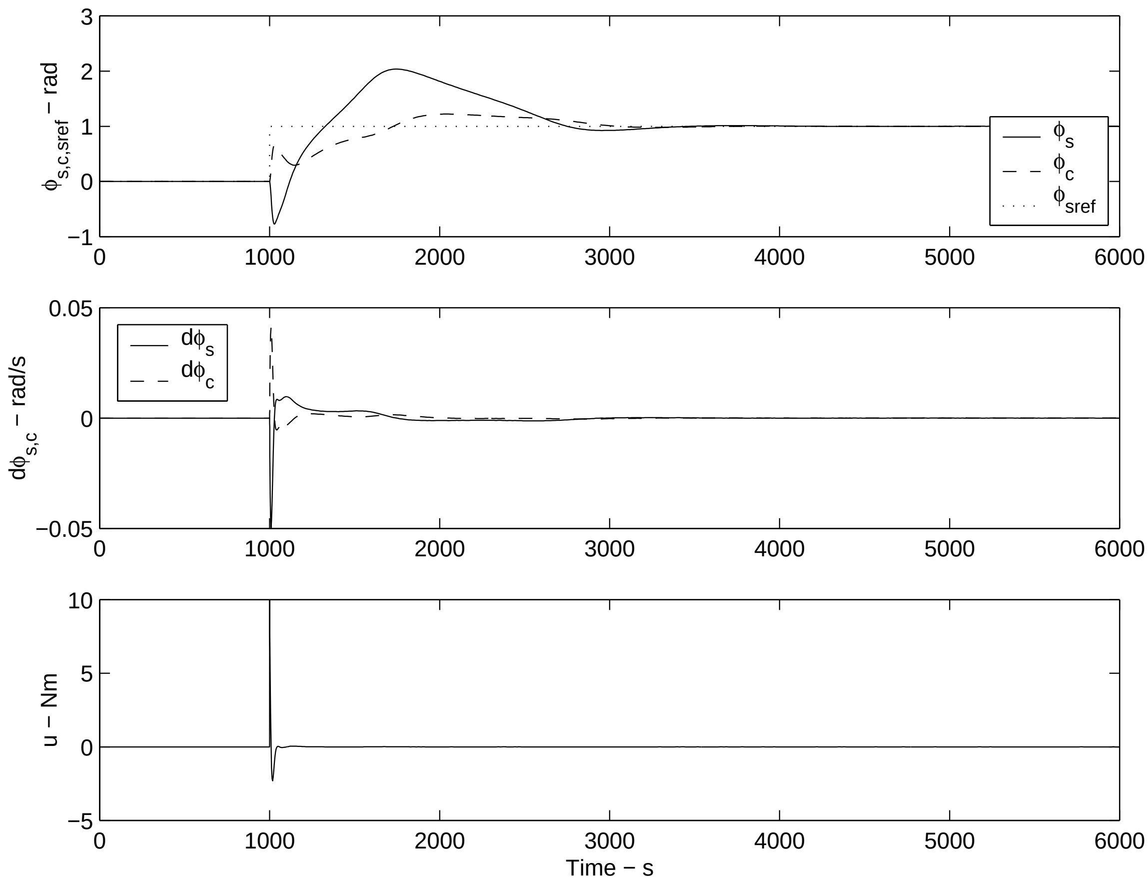


Figure 4.7: Medium performance solar sail responses to 1 radian step input

*Large Reference Input -* $\varphi_{s,ref} = \varphi_{c,ref} = 1$ *radian*

For all performance levels, the step response is very similar except for rise time. For the sake of brevity, only the medium performance sail response to a 1 radian step input will be shown. The responses of the low and high performance sails were similar.

The medium performance sail response to a 1 radian step input is shown in figure 4.7. On first glance, it is obvious that the overshoot is substantial. However, the sail does settle to the reference input within a reasonable time (relative to the responses to smaller step inputs). This suggests that there is a chance of improving the response.

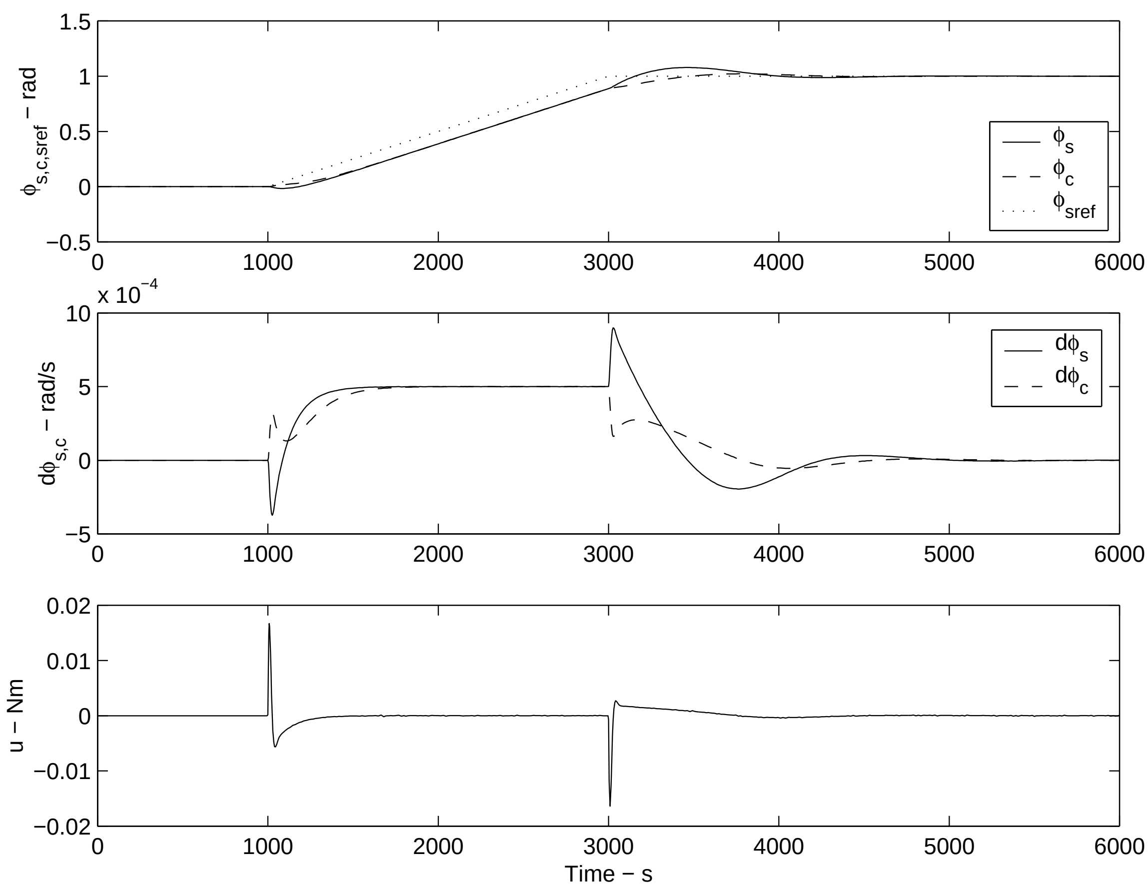


Figure 4.8: Medium performance solar sail responses to 1 radian ramp input

If a ramp input is fed to the controller that stops at 1 radian and takes about the same time to reach 1 radian as the sail takes to settle to 1 radian with a step response, it seems likely that the sail's response can be dramatically improved. This response is shown in figure 4.8. This method works very well. The sail position does have a small overshoot, but is quite manageable. Other attractive features of this method are the extremely low control torque and long time scale of the changes in the angular velocities. This suggests that the cost placed on the control input can be significantly relaxed if ramp inputs were used for all maneuvers.

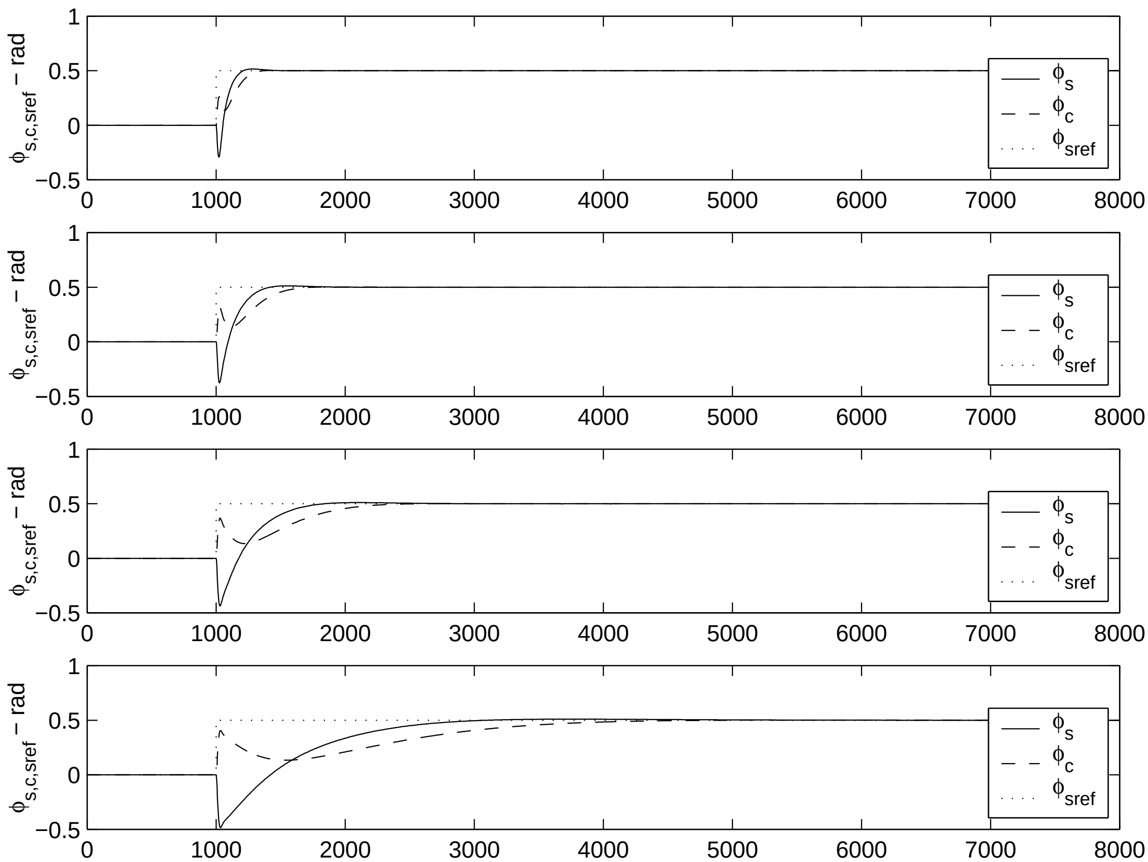


Figure 4.9: Medium performance solar sail responses to 0.5 radian ramp input at radii from the sun of 0.5, 1, 2, and 5 AU

### *4.3.2 Reference Input Responses at Varying Radius from the Sun*

The medium performance sail is tested at various radii from the sun. A reference input of 1 radian is used, and the radii tested are 0.5, 1, 2, and 5 radians. The angular position responses are shown, in order of increasing distance from the sun, in figure 4.9. These responses recalculated the state-space model and controller gain for the different radii. The only change present is the rise time, which is expected, as the solar radiation pressure available to turn the spacecraft decreases with increasing radius.

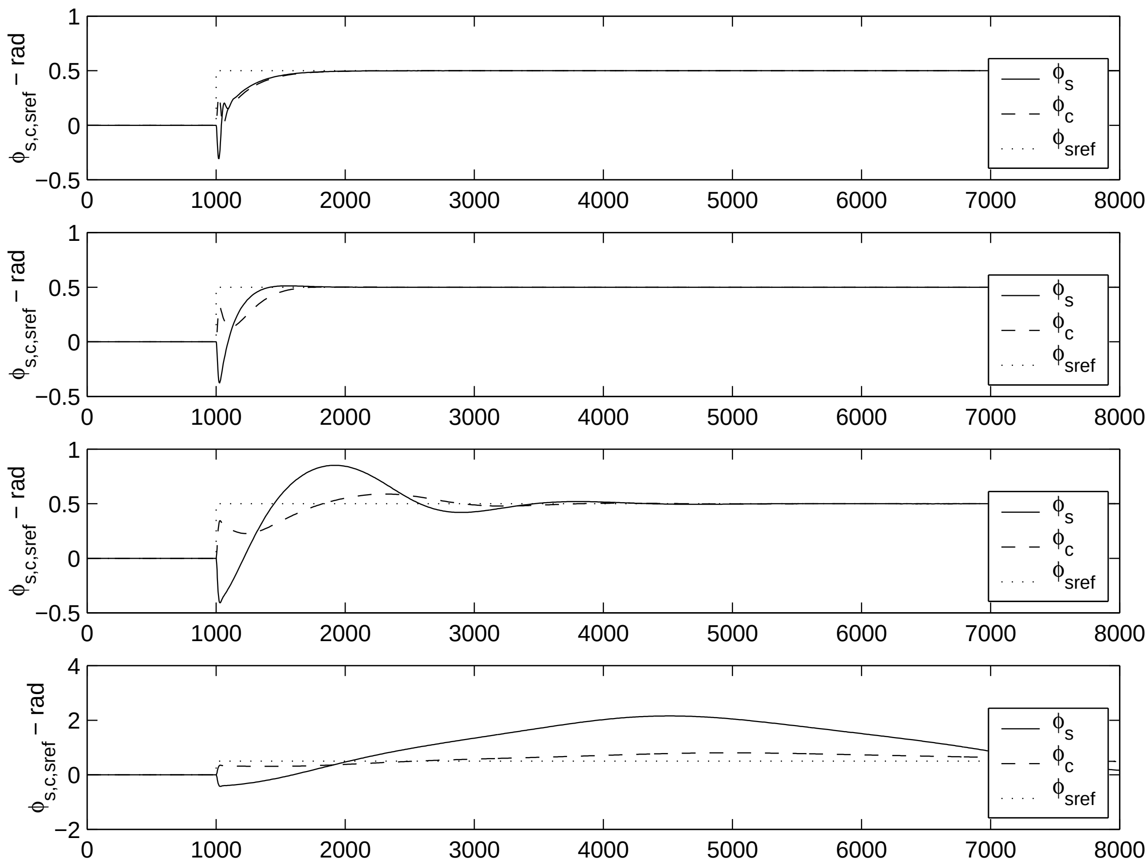


Figure 4.10: Medium performance solar sail responses with 1 AU controller to 0.5 radian ramp input at radii from the sun of 0.5, 1, 2, and 5 AU

Another interesting case to examine is how well a controller that was calculated at only one radius from the sun will behave at varying radii. This result, for a controller calculated at $r = 1$ AU, is shown in figure 4.10. Clearly, the LQR controller will need to be racalculated as the radius from the sun changes significantly.

### *4.3.3 Initial Condition Responses*

The initial condition responses of the system are now tested. Two sets of tests are run, one which tests the response to angular position initial conditions, and the second which tests the response to angular velocity initial conditions.

*Initial Angular Position Tests*

Figure 4.11 shows the response of the low-performance sail to an initial condition of $\varphi_s = \varphi_c = 0.5$ radian. The system responds by settling back to zero within $\approx 2000$ seconds, which is about the same time the system took to respond to a step command of 0.5 radian. The control torque is somewhat large (-5 N m), but still well within the 10 N m tolerance. The angular velocities are also kept low. This is something of a "worst-case" scenario, because rotating the boom to correct for the initial condition initially makes it much worse. However, as was the case with step responses, this was necessary to change the equilibrium position.

As with the step input responses, the medium and high performance solar sails responded almost identically except for settling time. Therefore, these responses will not be shown.

Figure 4.12 shows the low performance solar sail response to an initial condition of $\varphi_s = 0.5$ and $\varphi_c = -0.5$ radian. The sail is able to respond very quickly, because simply rotating the control boom back to zero brings the sail almost back. Some correction is needed, however, because the sail and control boom do not have identical moments of inertia, so both will not rotate exactly back to a zero equilibrium position from the same initial condition.

Figure 4.13 shows the response to an initial condition of $\varphi_s = 0.5$ and $\varphi_c = 0$ radian. The system is able to respond very nicely to this initial condition because moving the control boom into position to change the equilibrium position also moves the sail in the desired direction. Thus, the sail angular position never becomes larger than the initial condition. However, the settling time is still about the same as for other initial condition responses.

Figure 4.14 shows the response to an initial condition of $\varphi_s = 0$ and $\varphi_c = 0.5$. This is another "worst-case" scenario, because although the sail angle starts out at zero, it must be displaced by about 0.5 radian to return the control boom to equilibrium.

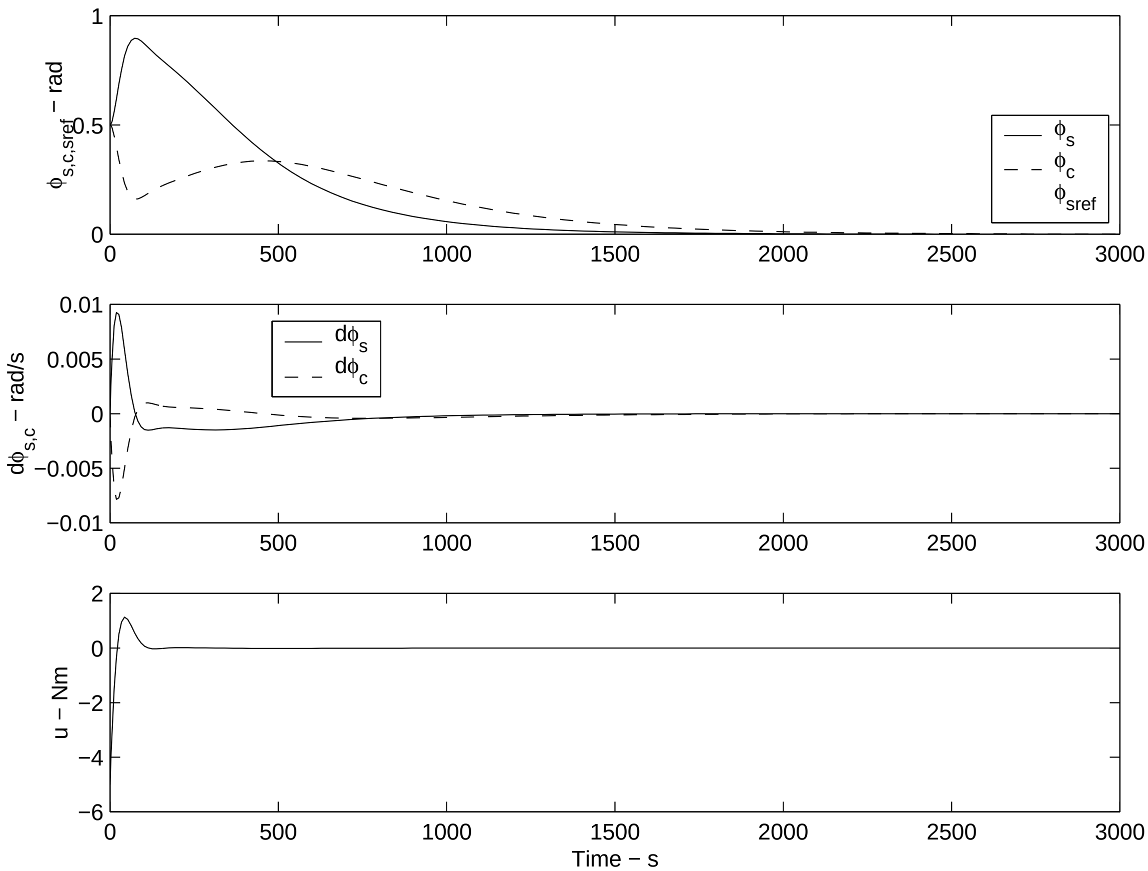


Figure 4.11: Low performance solar sail responses to $\varphi_s = \varphi_c = 0.5$ radian initial condition.

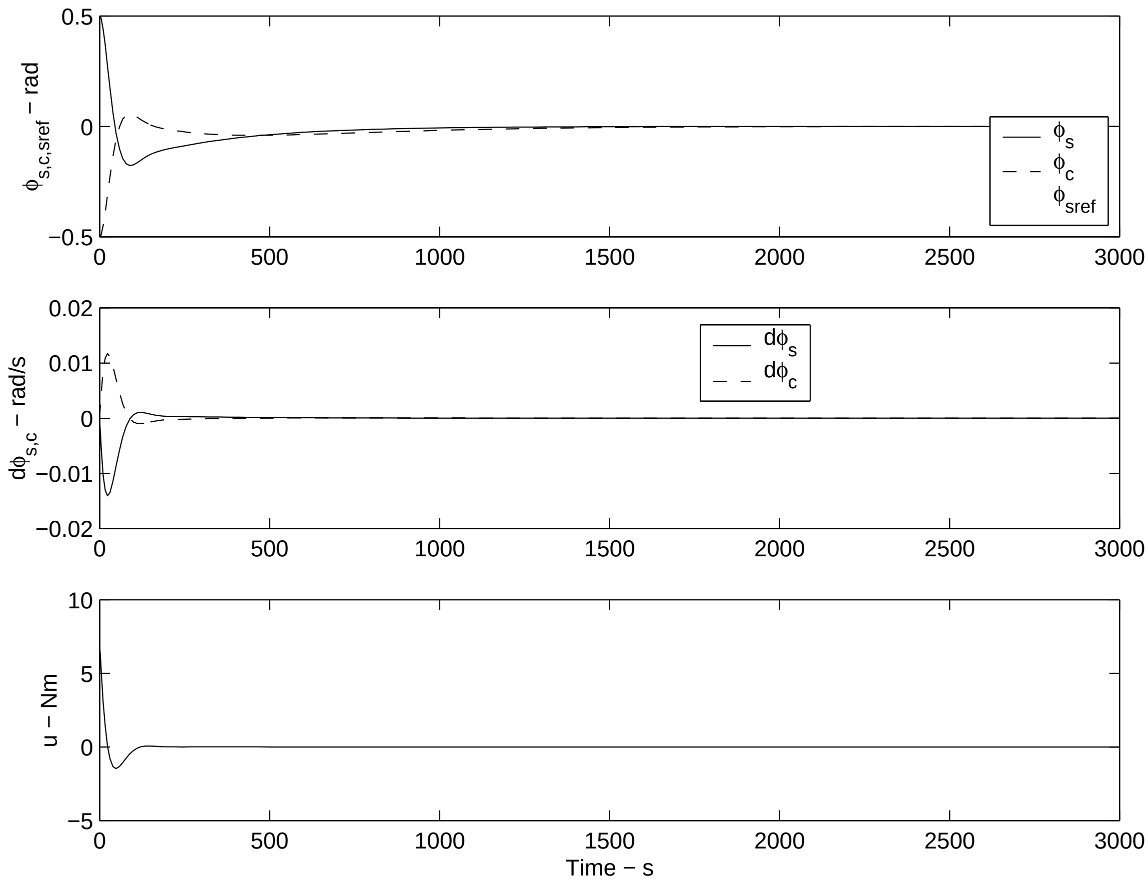


Figure 4.12: Low performance solar sail responses to $\varphi_s = \varphi_c = 0.5$ radian initial condition.

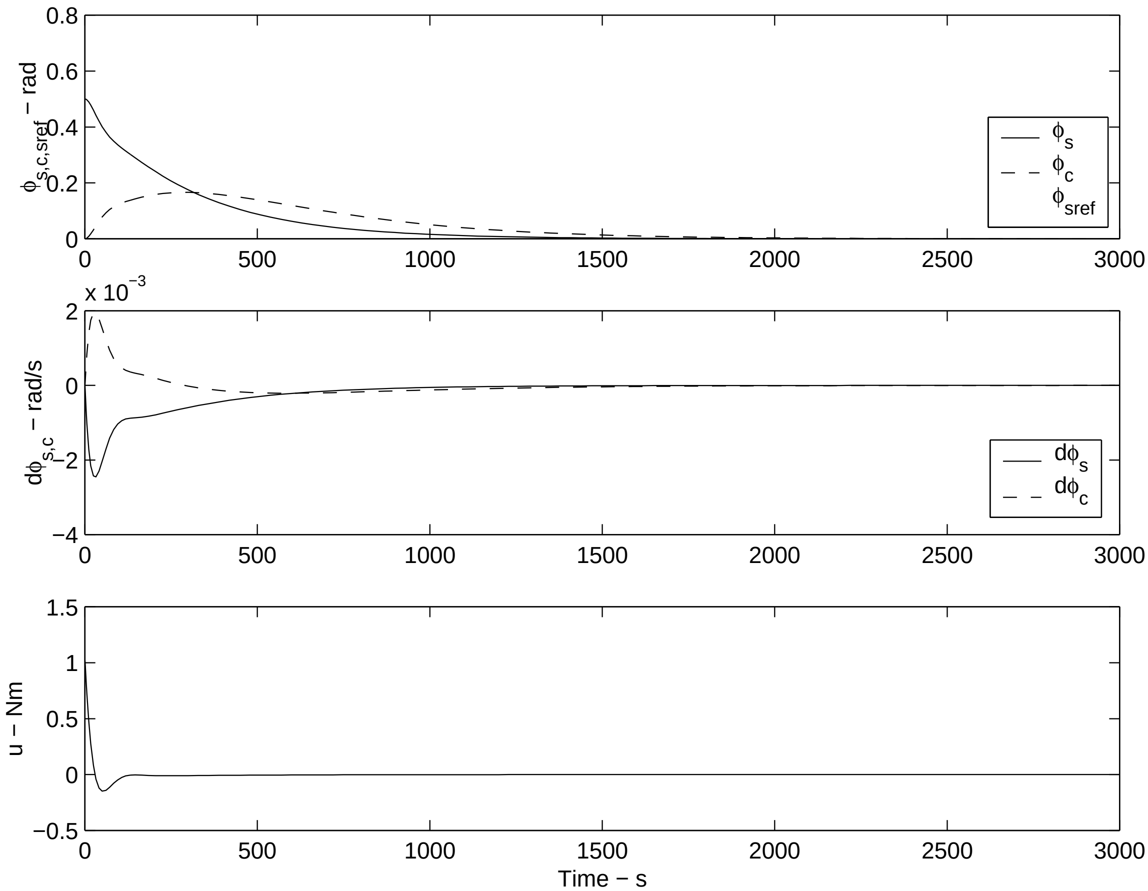


Figure 4.13: Low performance solar sail responses to $\varphi_s = \varphi_c = 0.5$ radian initial condition.

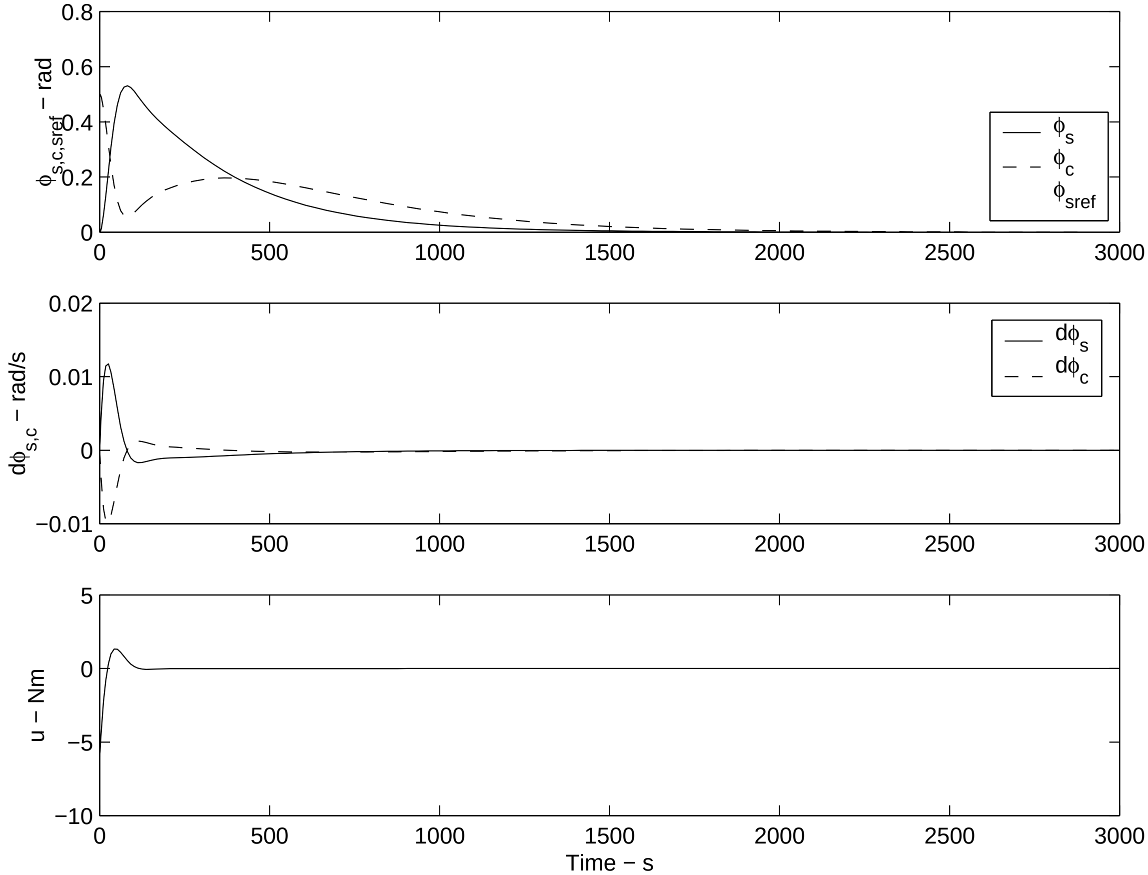


Figure 4.14: Low performance solar sail responses to $\varphi_s = \varphi_c = 0.5$ radian initial condition.

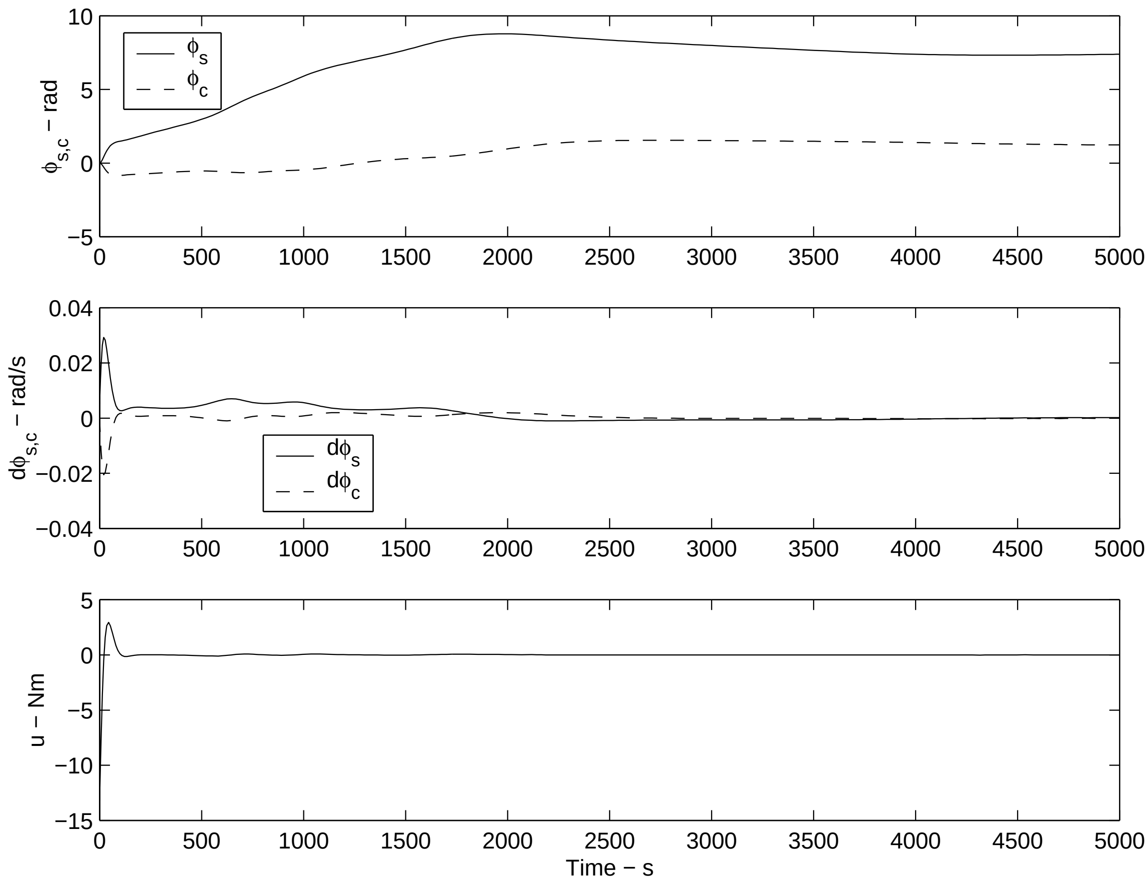


Figure 4.15: Low performance solar sail responses to $\dot{\varphi}_s = 0.005$ radian per second initial condition.

These tests show that the system is able to respond very well to initial angular positions.

*Initial Angular Velocity Tests*

Figure 4.15 shows the response of the low performance sail to an initial condition of $\dot{\varphi}_s = 0.005$ and $\dot{\varphi}_c = 0$ radian per second. Clearly, the system is unable to compensate for this initial condition, as the sail position increases steadily, and the angular velocities remain non-zero over time.

Figure 4.16 shows the response when the initial velocity is reduced to $\dot{\varphi}_s = 0.002$

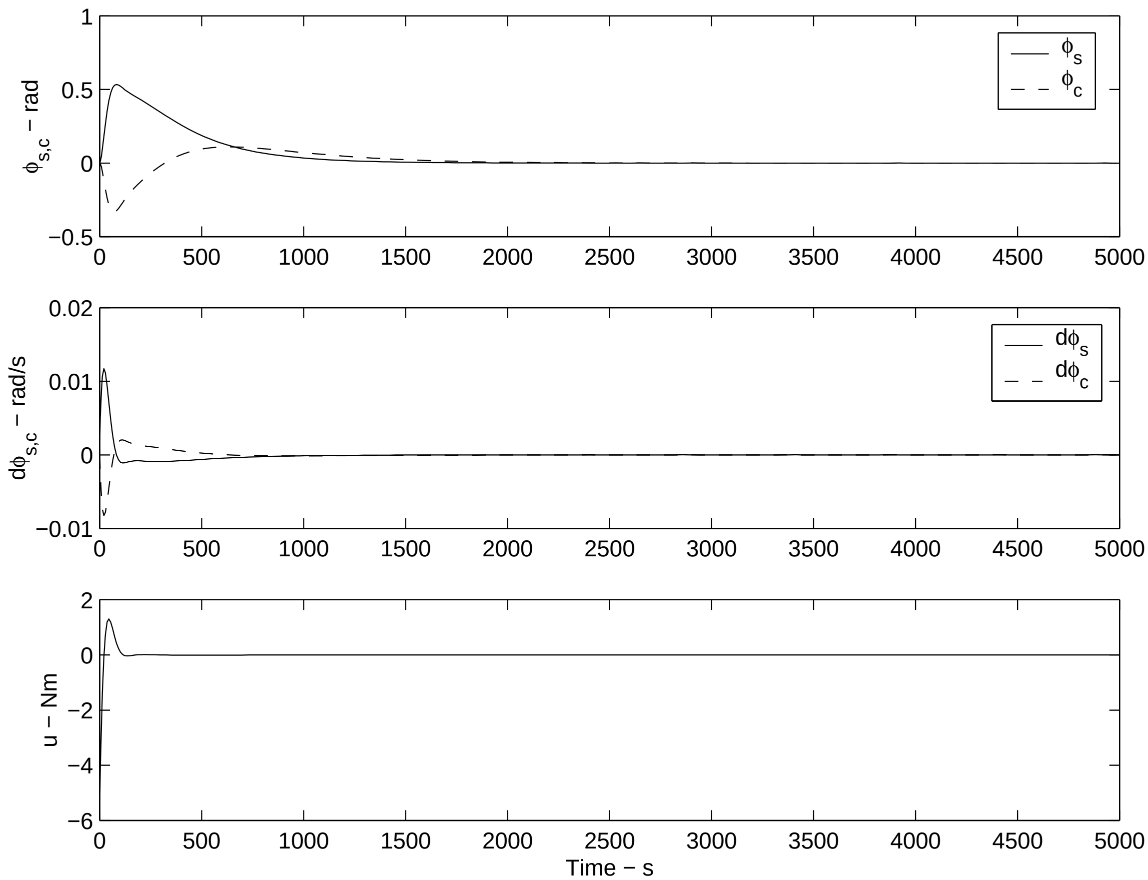


Figure 4.16: Low performance solar sail responses to $\dot{\varphi}_s = 0.002$ radian per second initial condition.

radian per second. This time, the system is able to compensate for the initial condition in a reasonable amount of time and control torque.

The responses to an initial control boom position are very similar. These are shown in figures 4.17 and 4.18.

If there is an initial angular velocity on both the sail and control boom, in the same direction, the effect is added. Figure 4.19 shows the effect of an initial condition of $\dot{\varphi}_s = \dot{\varphi}_c = 0.0025$ radian per second. The response is almost identical to that with an initial condition of 0.005 radian per second on either the sail or control boom angular velocity.

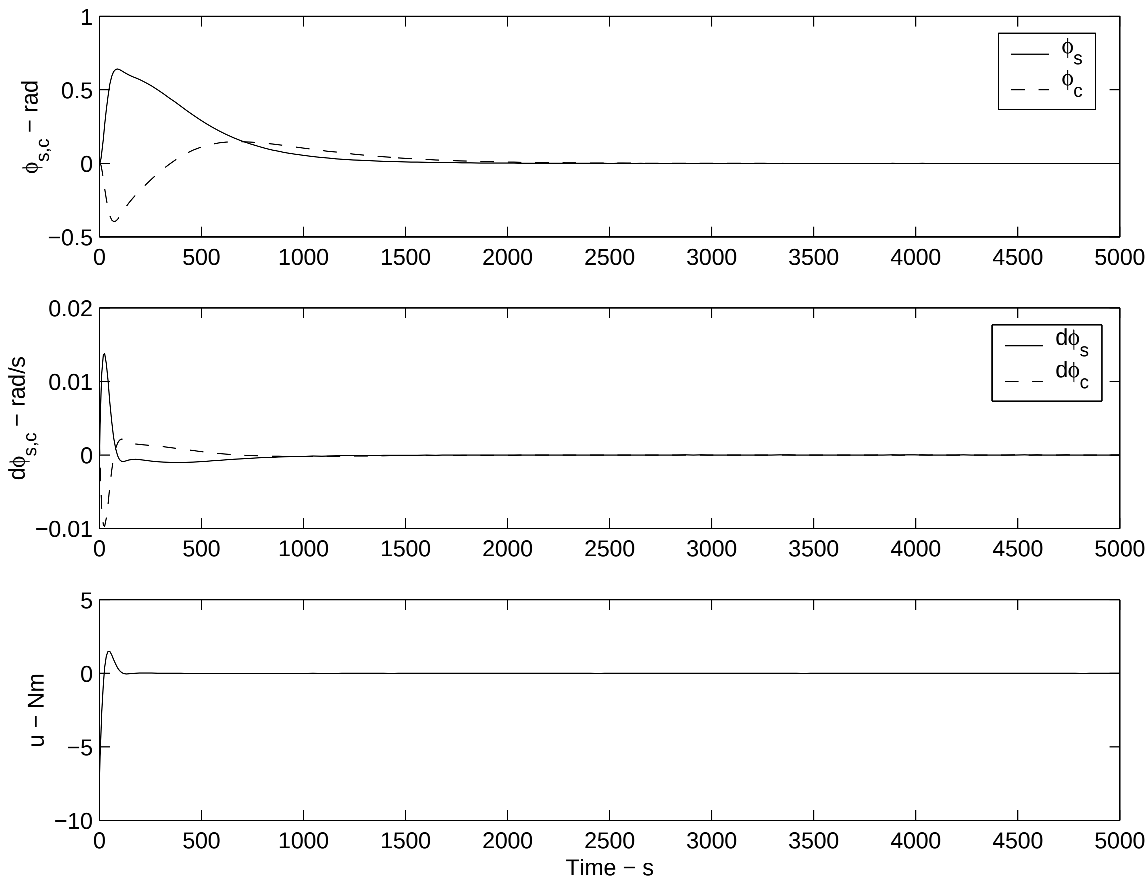


Figure 4.17: Low performance solar sail responses to $\dot{\varphi}_c = 0.002$ radian per second initial condition.

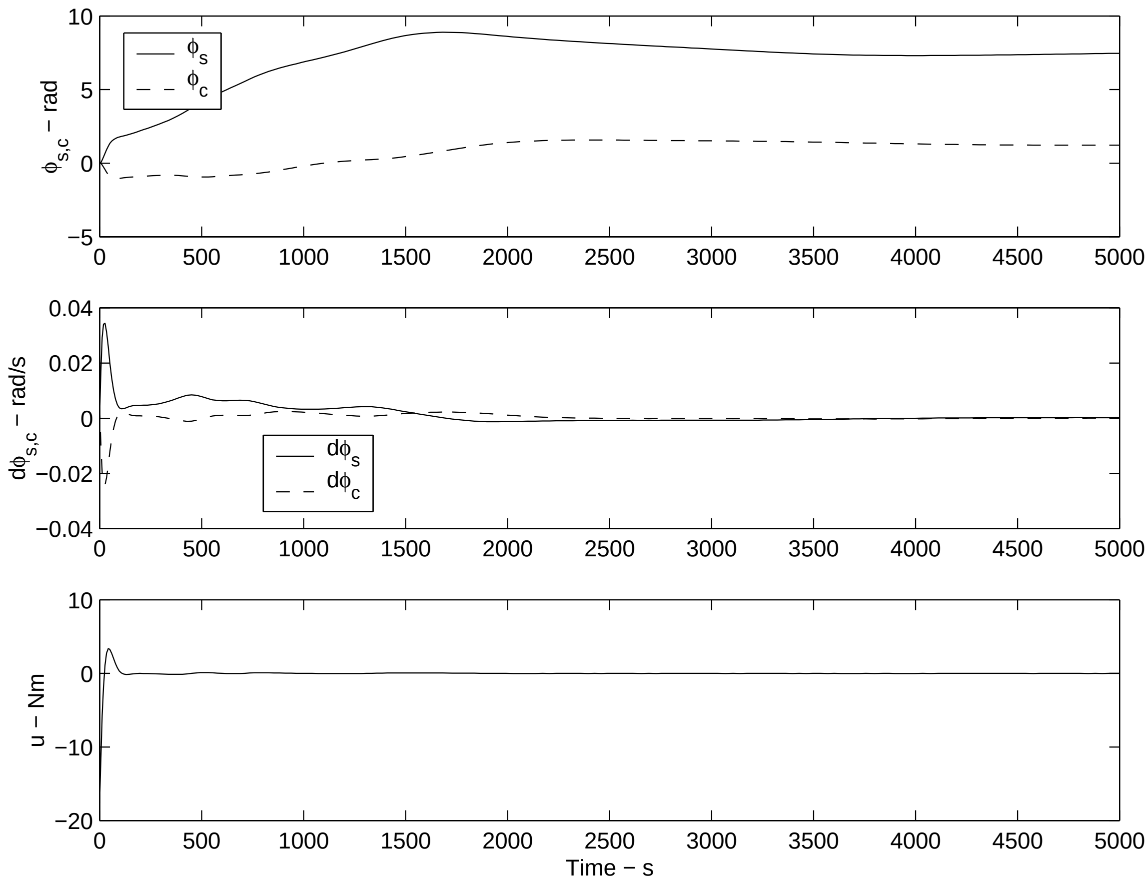


Figure 4.18: Low performance solar sail responses to $\dot{\varphi}_c = 0.005$ radian per second initial condition.

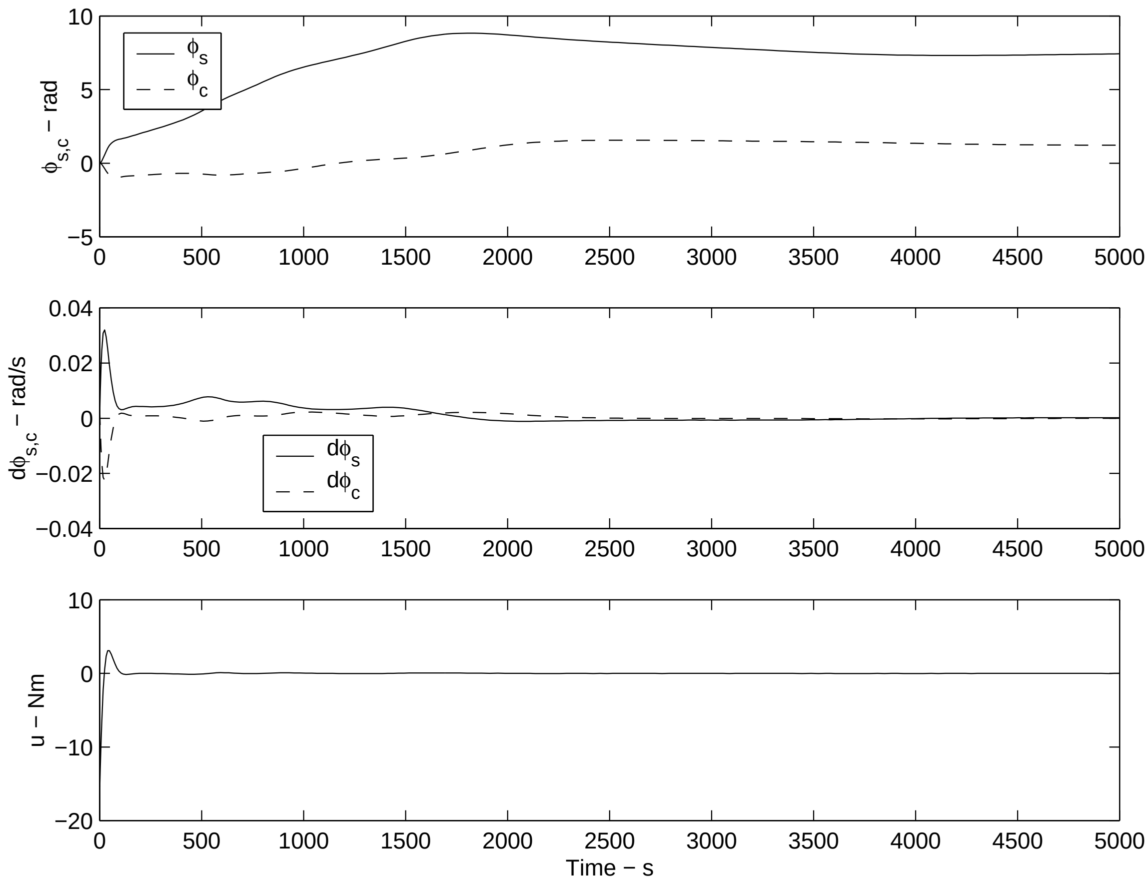


Figure 4.19: Low performance solar sail responses to $\dot{\varphi}_s = \dot{\varphi}_c = 0.0025$ radian per second initial condition.

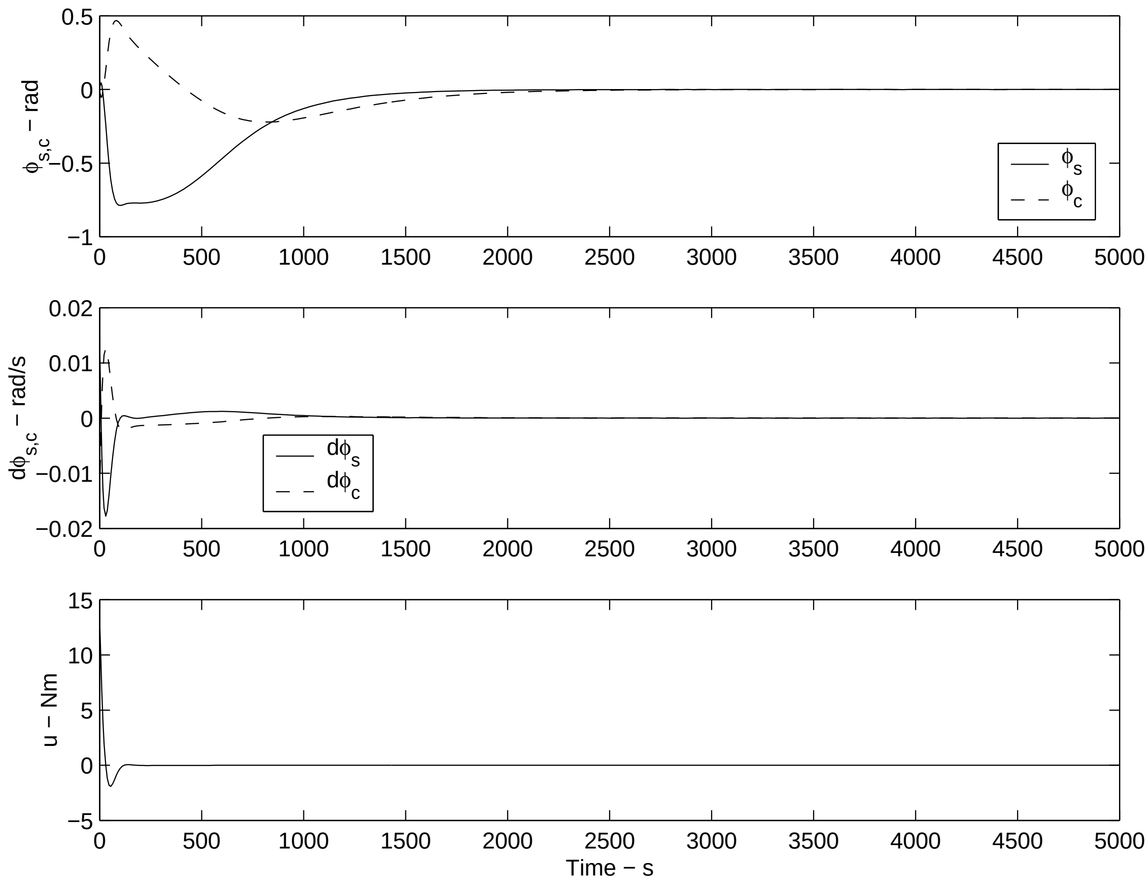


Figure 4.20: Low performance solar sail responses to $\dot{\varphi}_s = 0.015$ and $\dot{\varphi}_c = -0.015$ radian per second initial condition.

Initial sail and control boom velocities in opposite directions have the effect of cancelling each other out, like the initial position responses. Figure 4.20 shows the response to initial angular velocities of $\dot{\varphi}_s = 0.015$ and $\dot{\varphi}_c = -0.015$ radian per second. Even at this high of angular velocities, the system is able to compensate.

Higher performance solar sails allow for larger initial angular velocities before losing control. This can be explained by the quicker response time, which can damp out larger initial angular velocities. An example of this is shown in figure 4.21 for the medium performance sail and an initial condition of $\dot{\varphi}_s = 0.005$ radian per second.

This controller clearly cannot compensate for large angular velocities. This can

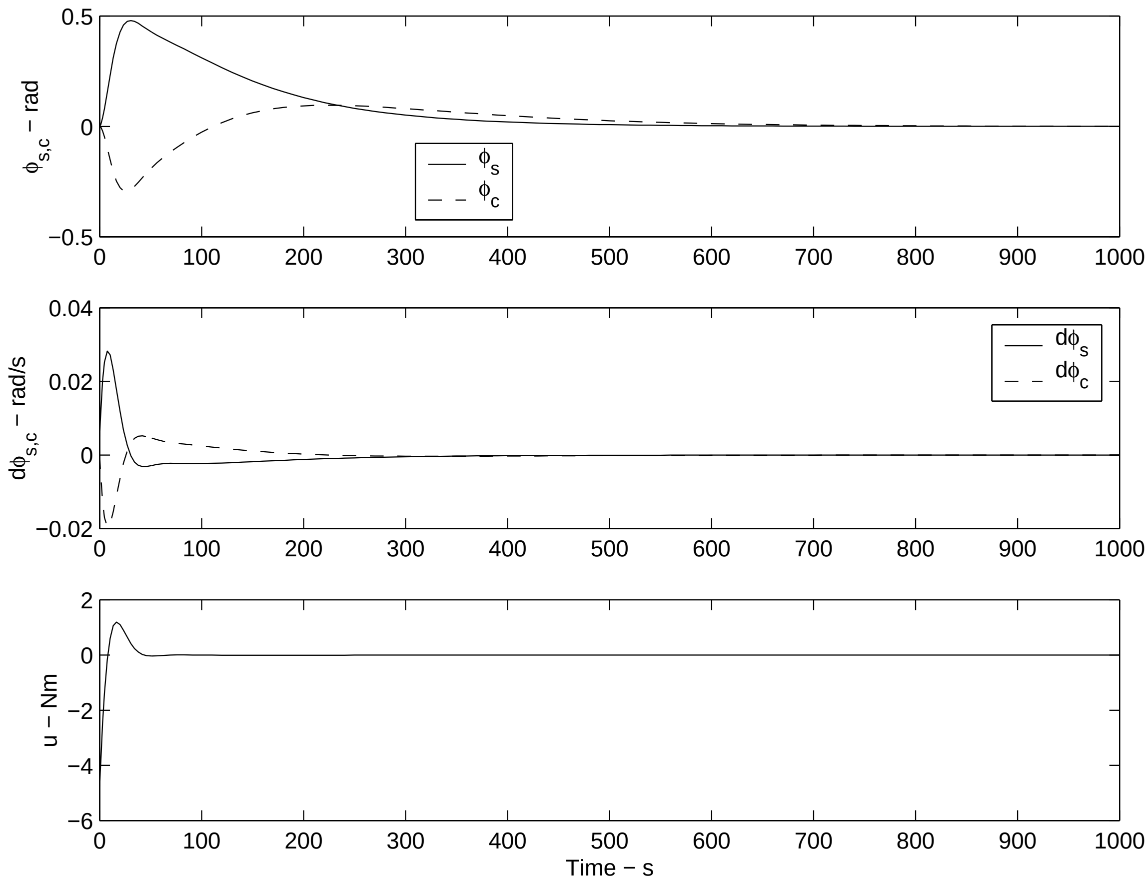


Figure 4.21: Medium performance solar sail responses to $\dot{\varphi}_s = 0.005$ radian per second initial condition.

be attributed to the slow response of the system to changing the equilibrium condition. Further work may be needed to increase the tolerance, however, as the angular velocities seen in the step responses (section 4.3.1) were an order of magnitude for some cases.

# Chapter 5

# ORBITAL SIMULATION

## *5.1 Introduction*

Ultimately, the purpose of a solar sail attitude control system is to guide a solar sail along a trajectory in space for particular missions. Solar sail orbital dynamics are derived in appendix B. The control input required to guide a solar sail through space is the angle of the sail with respect to the incident sunlight. This angle determines the force vector acting on the sail, and thus the trajectory.

In this section, solar sail trajectories are presented, along with the time history of the sail angle required to give the trajectory. This control time history is fed into the solar sail attitude control system as the reference position, and the performance is evaluated. The time scale over which the trajectories occur is much longer than the time scale over which attitude control maneuvers are performed, so only select areas of the trajectory will be simulated with the attitude controller.

The trajectories presented are optimal time of flight trajectories that were found using the two-dimensional solar sail orbital dynamics from appendix B, trajectory optimization cost function developed in appendix C, and the dynamic gradient optimization techniques presented in [Ly99a] and [Bry99]. All orbits are assumed to be circular and two-dimensional. Thus, eccentricity and inclination of orbits are not considered.

Units of time (TU) and distance (DU) which are based on the orbit of the Earth are used to simplify calculations and results. DU is the mean radius of Earth's orbit, which is 1.4960E8 kilometers. TU is the time it takes the Earth to travel one radian around it's orbit, assuming a circular orbit, which is 5.0227E6 seconds, or 58.133 days. This allows the Earth's velocity to be 1 $\frac{DU}{TU}$, and the sun to have a gravitational parameter of 1 $\frac{DU^3}{TU^2}$.

These units also allow for much simplified initial condition vectors. The polar coordinates and velocities used in the solar sail orbital dynamics in appendix B apply equally to the planets. The initial conditions or final constraints for leaving or arriving at Earth are simply $r = 1\,\mathrm{DU}$, $v_r = 1\,\frac{DU}{TU}$, and $v_\theta = 0\,\frac{DU}{TU}$. The angular position $\theta$ can be set to zero for initial conditions.

## 5.2 Earth–Mars Trajectories

Earth–Mars trajectories are of significant interest for near-term solar system exploration, and possibly human colonization. Trajectories for the low, medium, and high performance sails presented in chapter 4 are presented. Mars is assumed to have a circular orbit of radius $r = 1.5\,\mathrm{DU}$.

The low performance Earth to Mars trajectory is given in figure 5.1. All of the plots displaying the trajectory graphically display the sail angle at periodic points. The time history of the sail angle to give this orbit is given in figure 5.2. The control stays within a narrow range of sail angles ( 0.6 to 0.66 radian) which the control system proved very capable of providing in chapter 4. The Mars to Earth trajectory using a low performance sail has a very similar, but negative, control time history.

The medium and high performance Earth-Mars trajectories are quite different, because of the increased thrust available. These trajectories take less than a complete circuit of the sun to complete, so do not have the gently oscillating control profile. The medium performance Earth to Mars trajectory and control time history are shown in figures 5.3 and 5.4. This trajectory has a critical maneuver where the sail angle goes from 0 to 1.3438 radians in 1.5276E6 seconds. This time rate of change of the sail position is well within the capabilities of the controller. The high performance

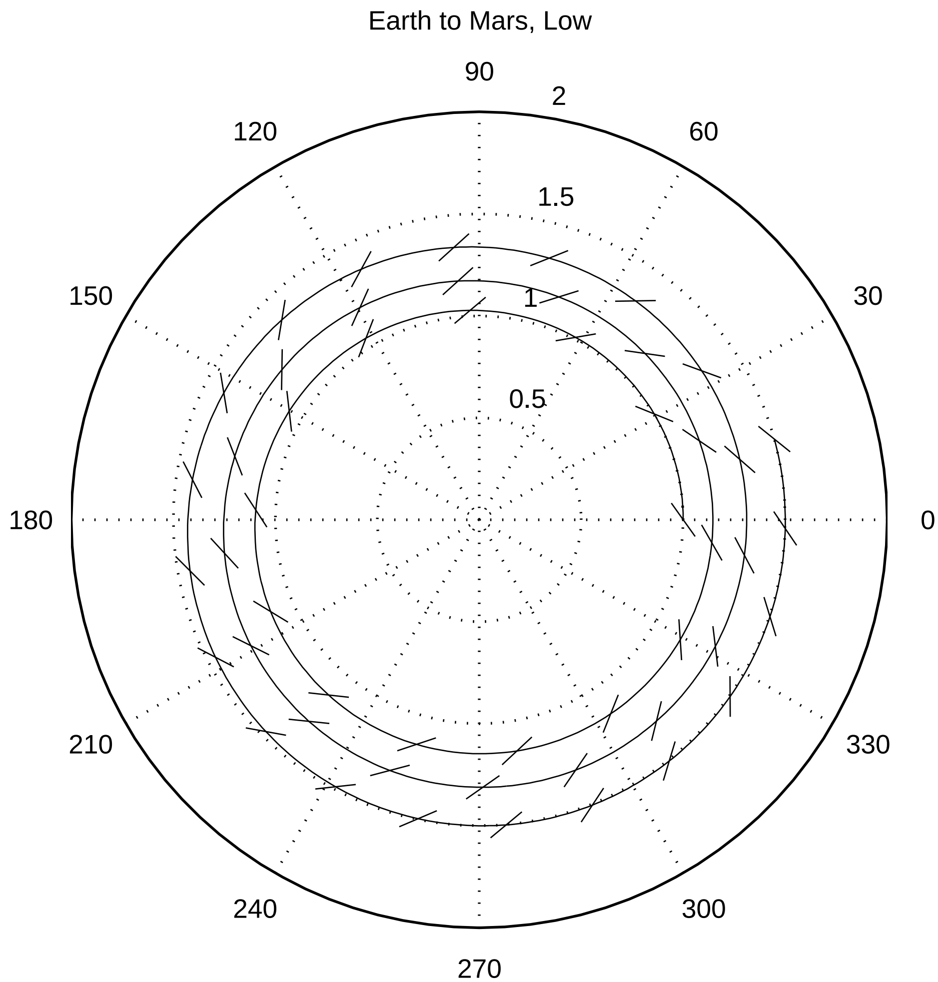


Figure 5.1: Low performance Earth to Mars trajectory

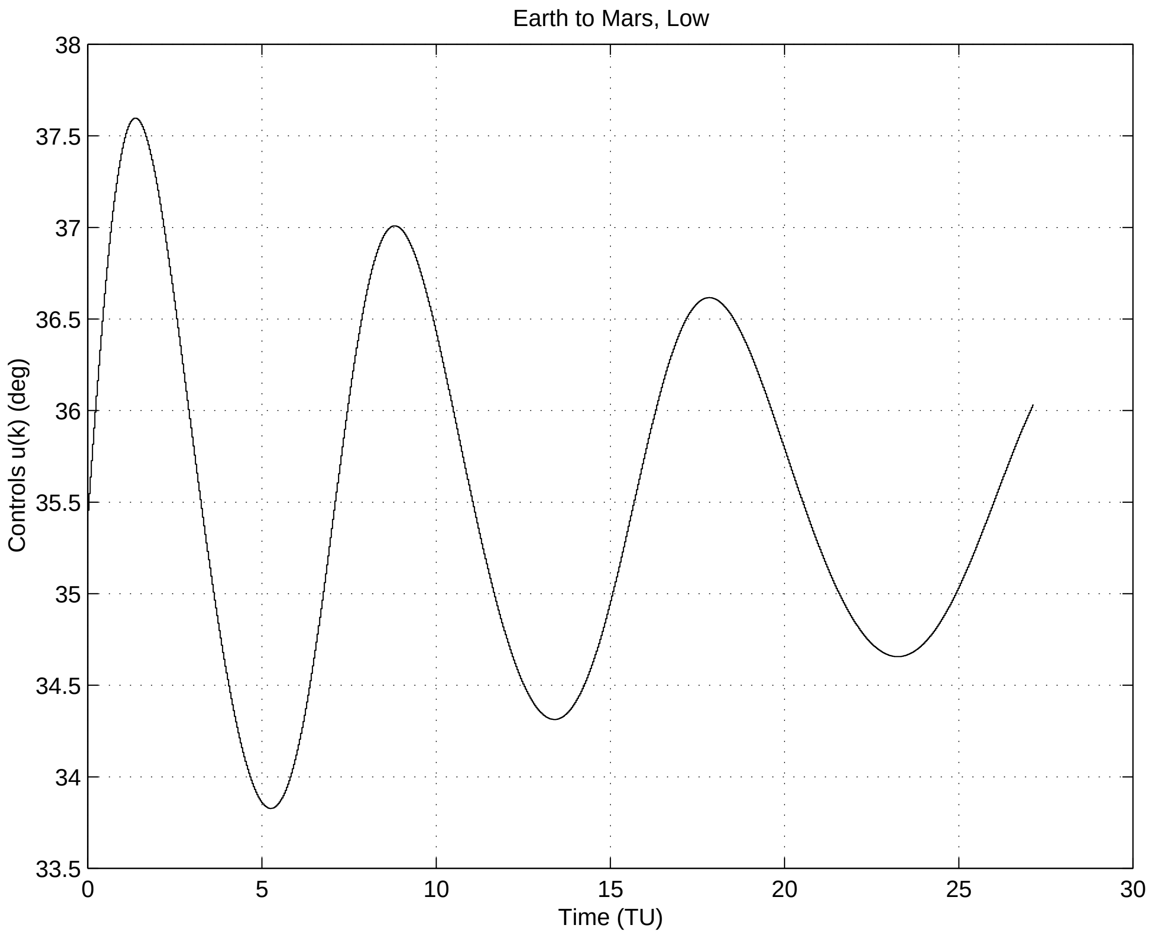


Figure 5.2: Low performance Earth to Mars control

sail has a very similar flight and control time histories, but a shorter overall time of flight. Like the low performance trajectory, the return flight to Earth has a similar, but mirror-image and negative control profile.

As a test, the area shortly before and after the peak attitude control angle is examined. The LQR controller gain matrix is calculated given the radius at that point, 1.8124E8 km. The equilibrium position is still assumed to be a sail and control boom position of $\varphi_{s,eq} = \varphi_{c,eq} = 0$ radians. The result is shown in figure 5.5. The small magnitude oscillation at the beginning shows where the controller corrects for the initial condition which is slightly different from the reference input. This oscillation would be eliminated for a controller calculated at an equilibrium point closer to this operating point. For the rest of the trajectory segment, the sail holds very closely to the reference input sail position, and the control input and angular velocities are very small.

This represents a "worst-case" scenario, as the control input is somewhat close to $\frac{\pi}{2}$, but the controller is still able to function quite well, given the long time periods available for maneuvers.

## 5.3 Earth–Venus Trajectories

Low and medium performance Venus-Earth trajectories do not pose any additional challenge to the control system than the Earth-Mars trajectories. The high performance trajectories, however, pose an interesting problem. The high performance Earth to Venus trajectory and control history are shown in figures 5.6 and 5.7. The control goes to -1.5702 radians, which is very close to $-\frac{\pi}{2}$ or -1.5708 radians. However, because the change in control input is very slow, it may still be possible to control the sail close to this point.

A simulation is performed around the minimum control value. This result is shown in figure 5.8. Like the Earth-Mars simulation, the LQR gain matrix was calculated

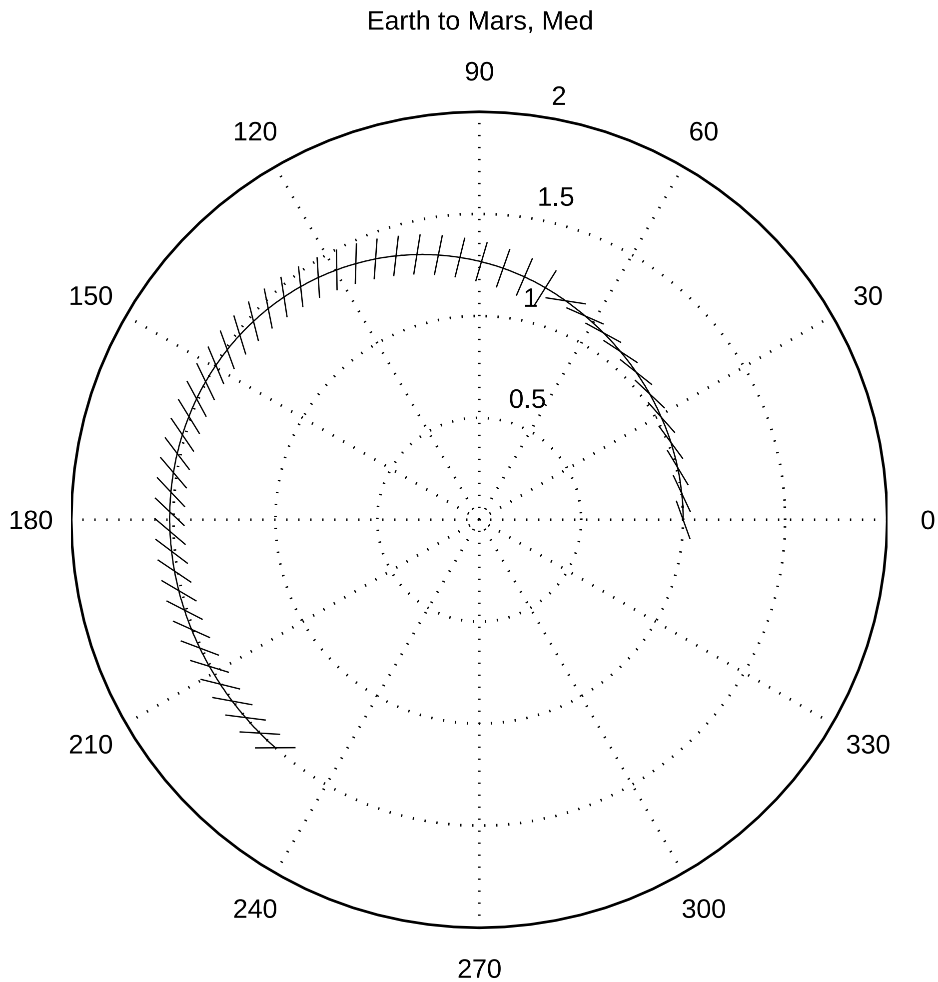


Figure 5.3: Medium performance Earth to Mars trajectory

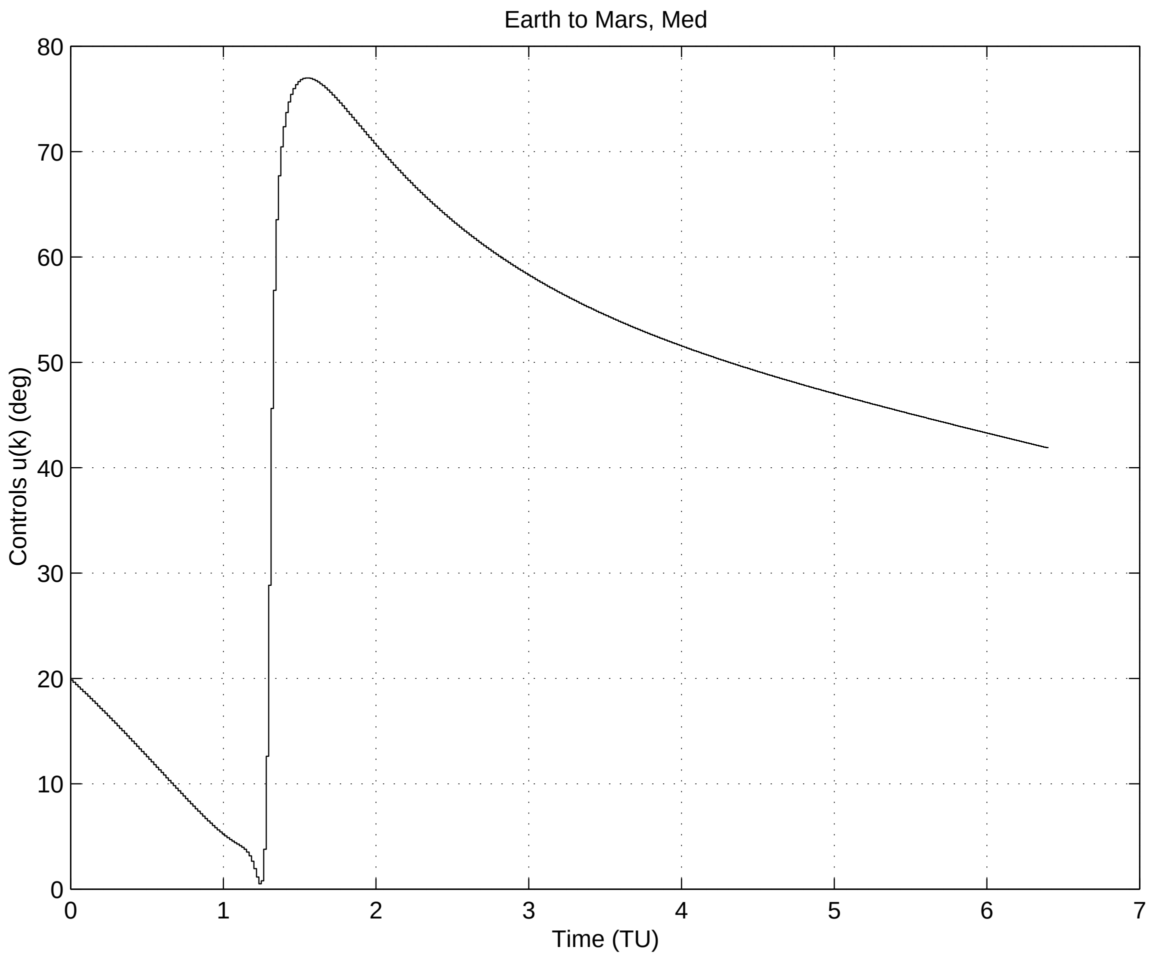


Figure 5.4: Medium performance Earth to Mars control

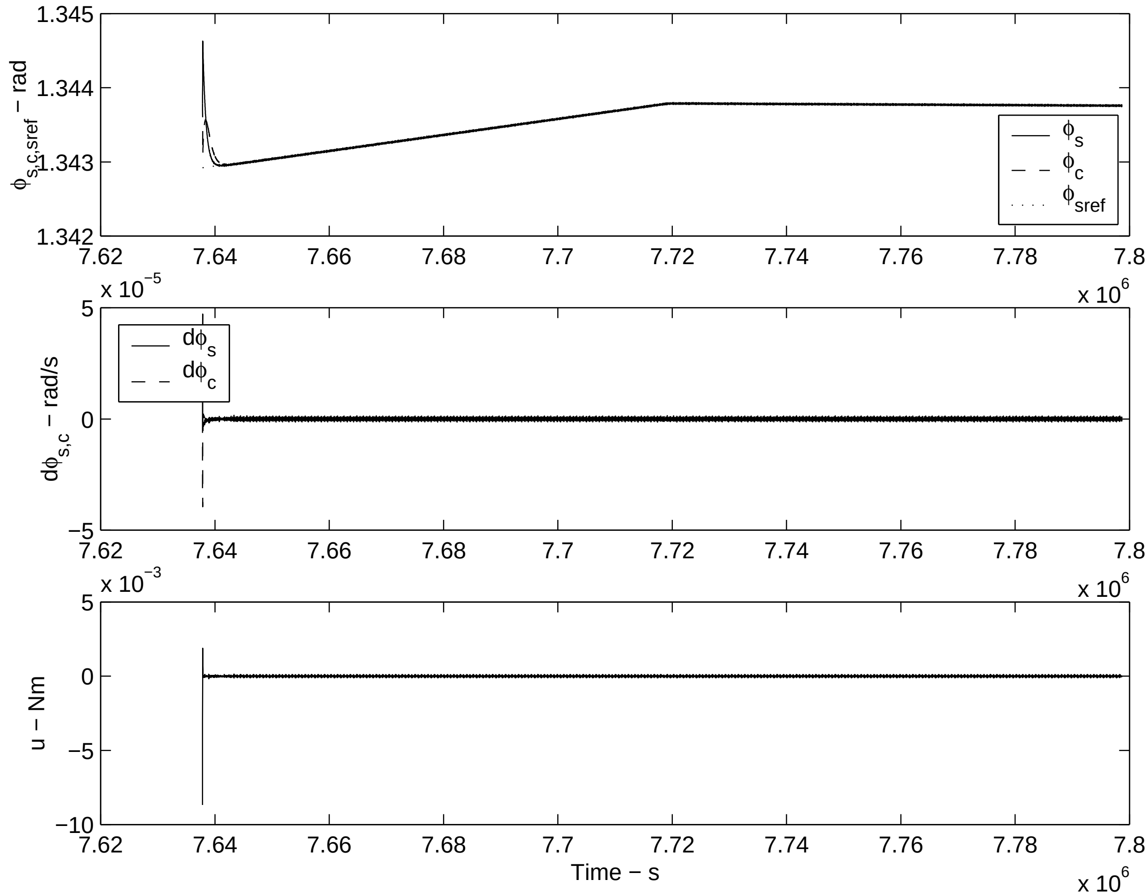


Figure 5.5: Medium performance Earth to Mars attitude control simulation

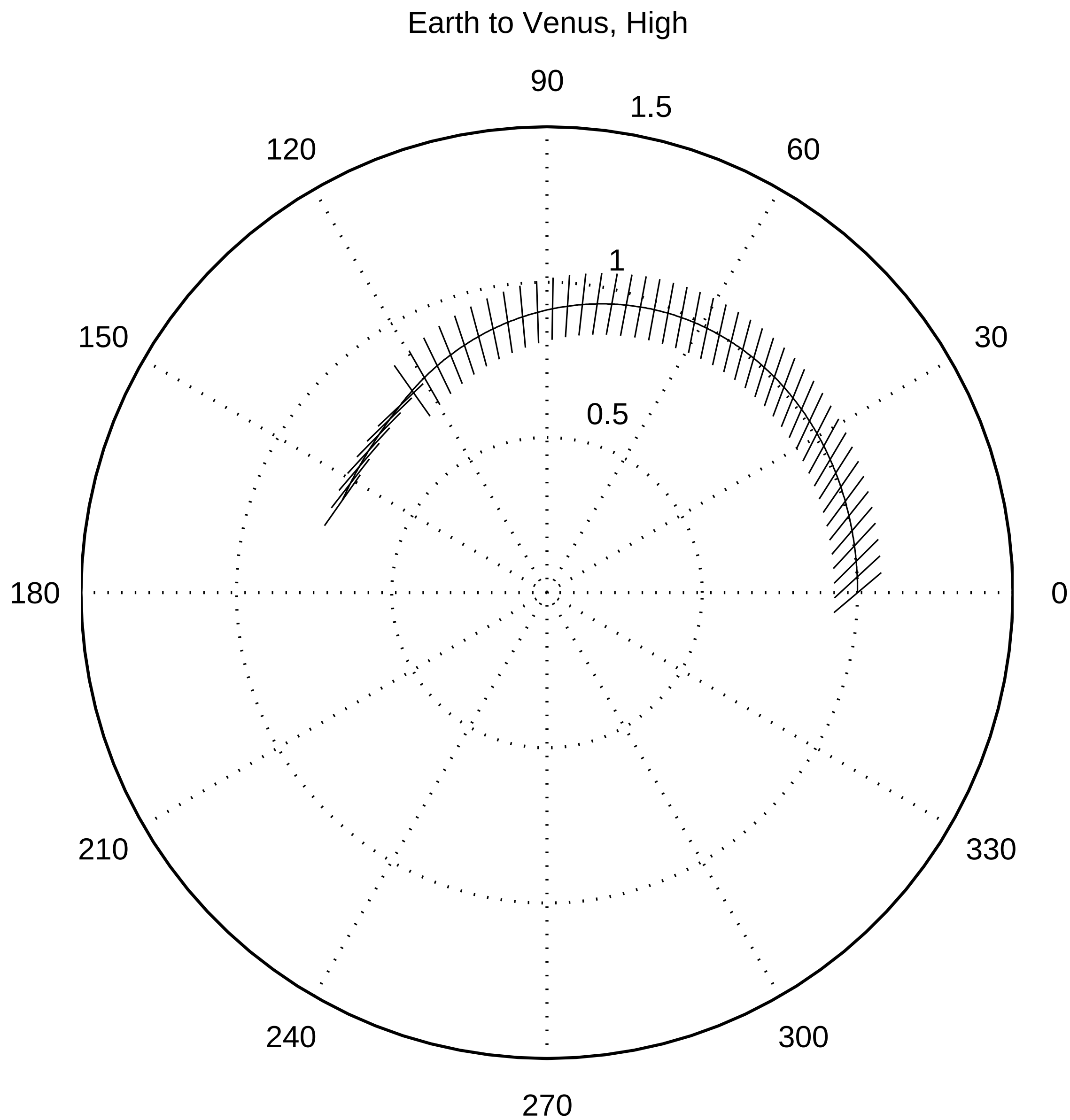


Figure 5.6: High performance Earth to Venus trajectory

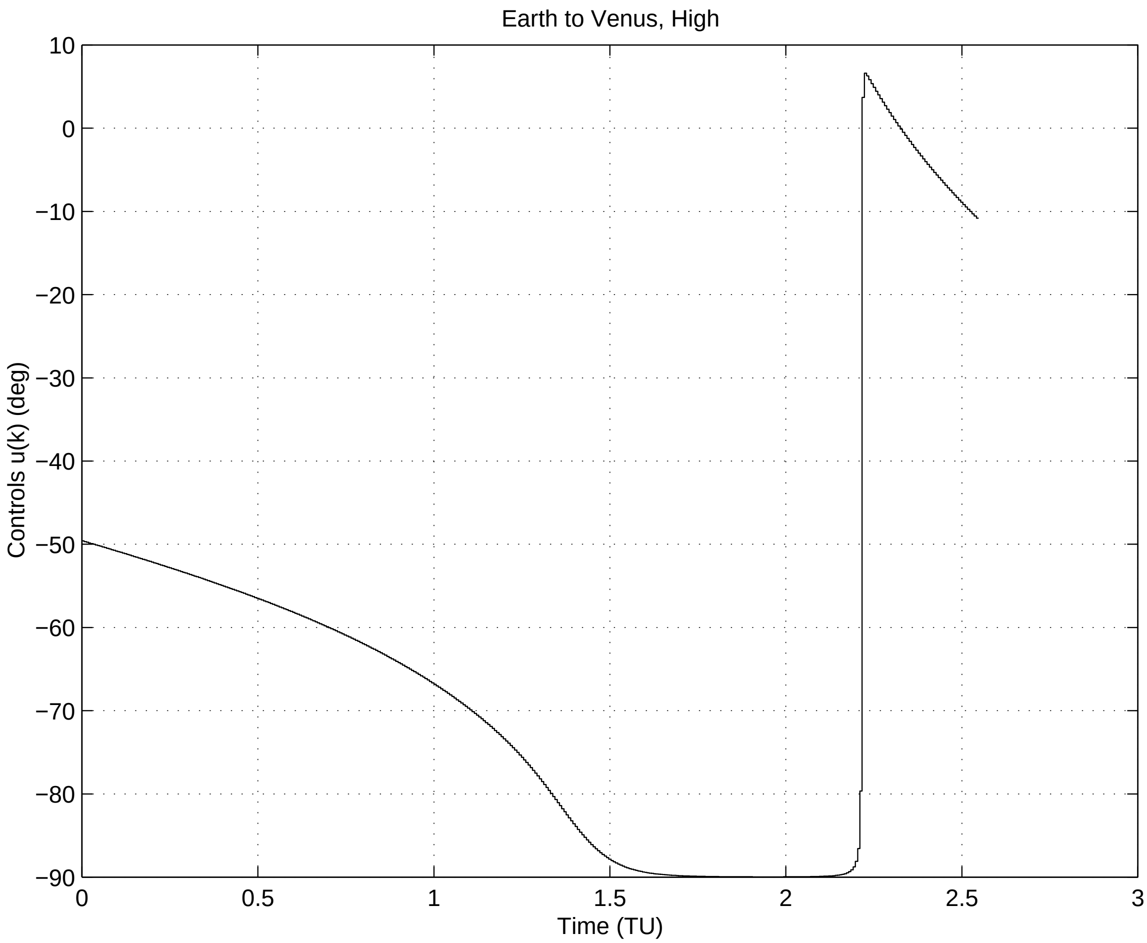


Figure 5.7: High performance Earth to Venus control

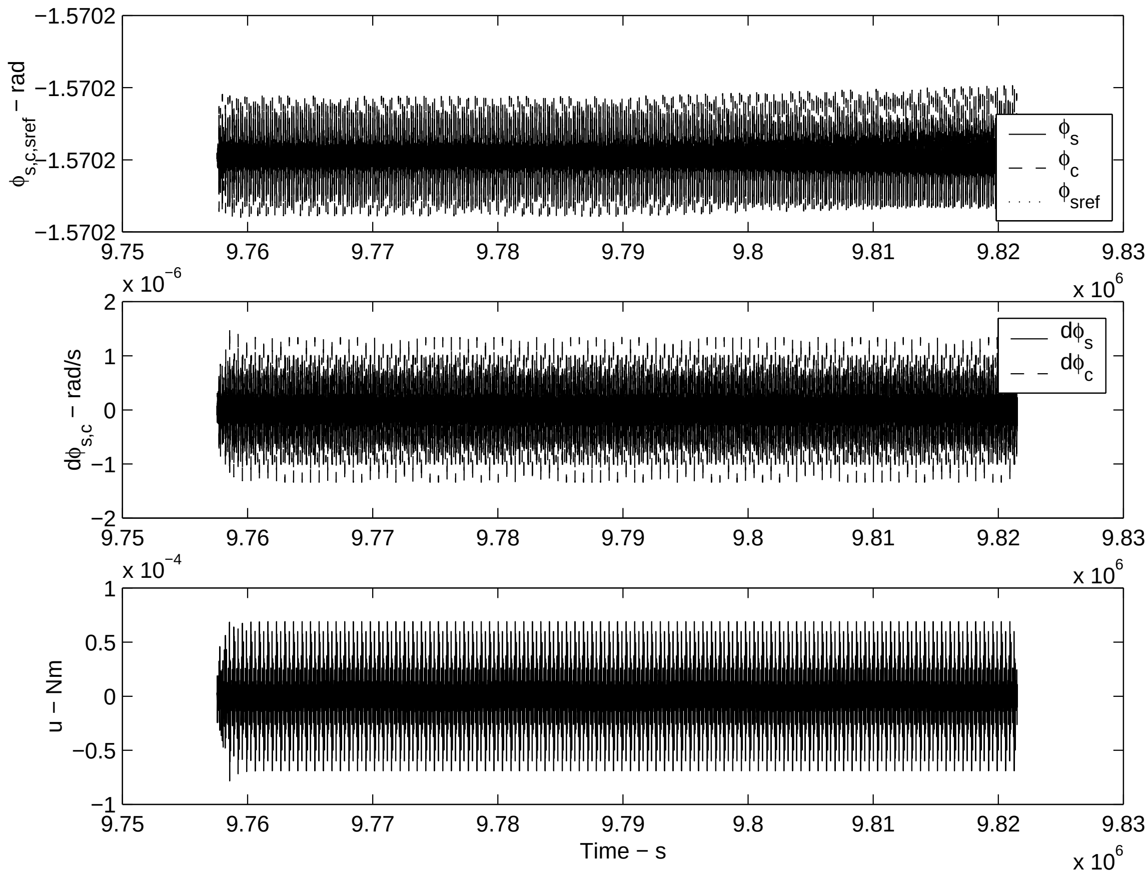


Figure 5.8: High performance Earth to Venus attitude control simulation

at the radius from the sun where the simulation was performed and an equilibrium position of $\varphi_{s,eq} = \varphi_{c,eq} = 0$. It appears that so long as disturbances and initial conditions are kept to a minimum, the attitude controller can operate very close to $\frac{\pi}{2}$. However, it may be desirable to place inequality constraints on the trajectory optimization, so that sail angles close to $\frac{\pi}{2}$ are avoided.

## *5.4 Earth–Jupiter Trajectories*

Because Jupiter is very far from the Earth–5 DU–only medium and high performance trajectories were found. Earth to Jupiter trajectories pose no great difficulties for the attitude control system. This is reflected in the trajectory and control histories for the medium performance trajectory given in figures 5.9 and 5.10. The high performance trajectory follows the same pattern.

Serious problems arise, however, for Jupiter to Earth trajectories. The medium and high performance Jupiter to Earth trajectories and control histories are shown in figures 5.11, 5.12, 5.14, and 5.14. There are significant areas of both trajectories where the required sail angle is exactly $\frac{\pi}{2}$. The portion of the high performance trajectory where the control input is larger than $\frac{\pi}{2}$ is an oddity of the numerical algorithm. These values actually correspond to negative sail angles. The attitude controller simply will not be able to track these regions, because the system becomes uncontrollable. A control method other than LQR is needed to maintain the sail at this position, or the optimization scheme will need to use inequality constraints to keep the control away from $\frac{\pi}{2}$.

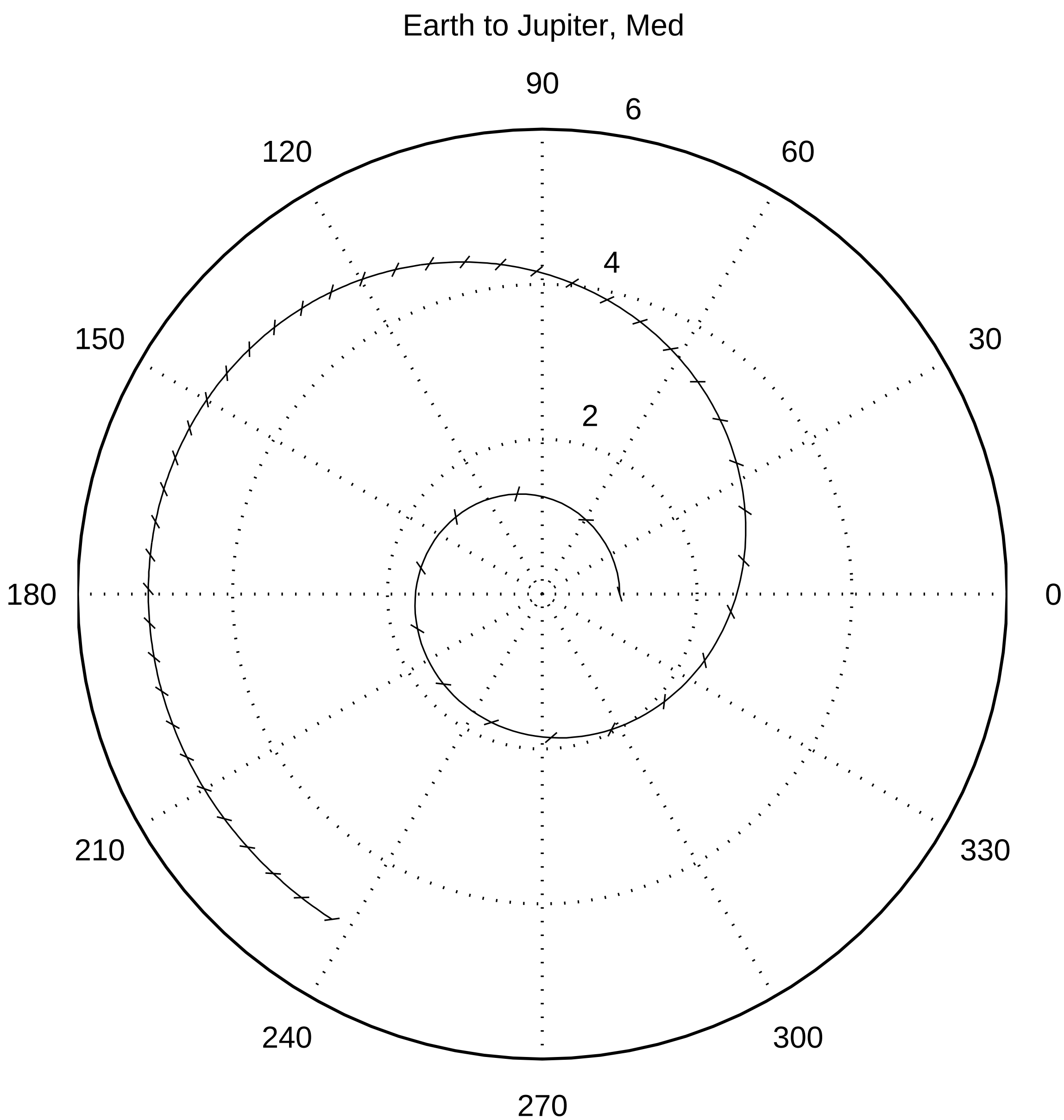


Figure 5.9: Medium performance Earth to Jupiter trajectory

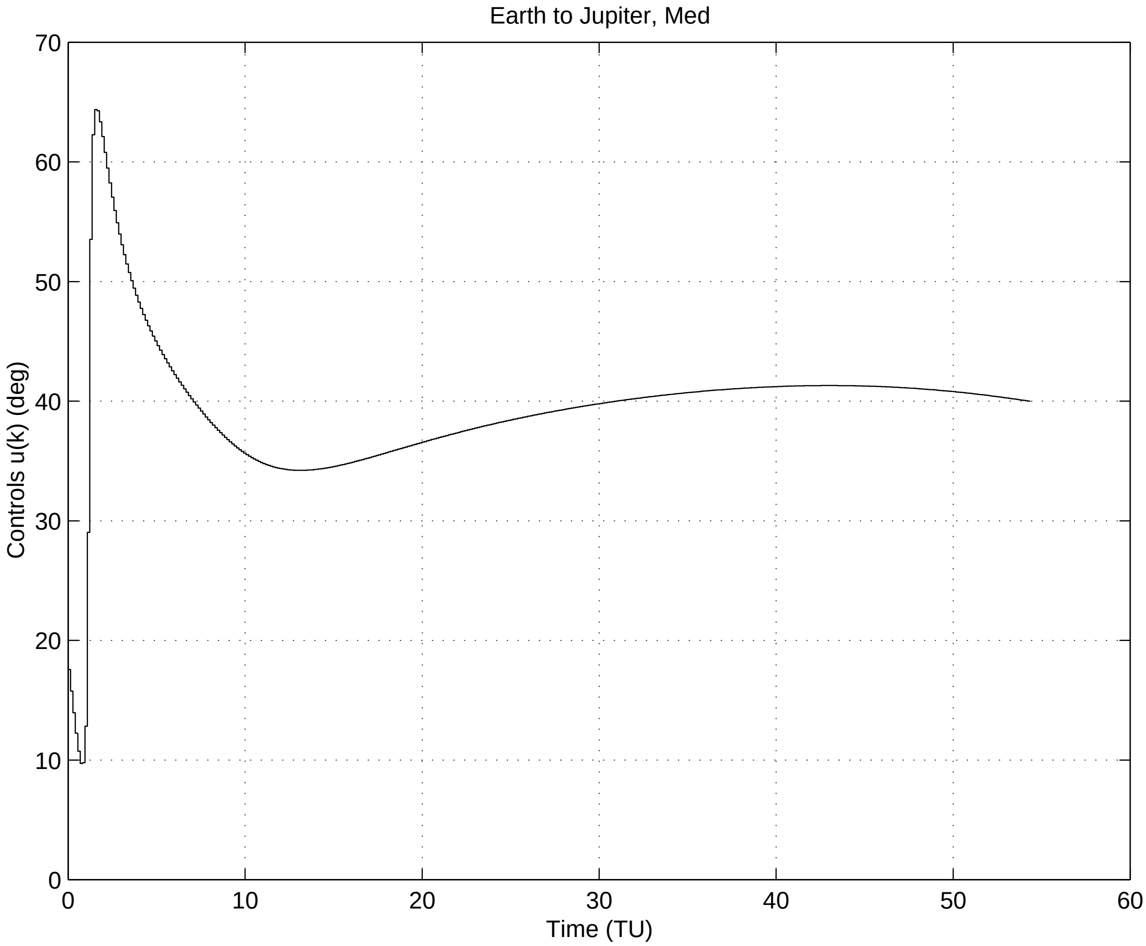


Figure 5.10: Medium performance Earth to Jupiter control

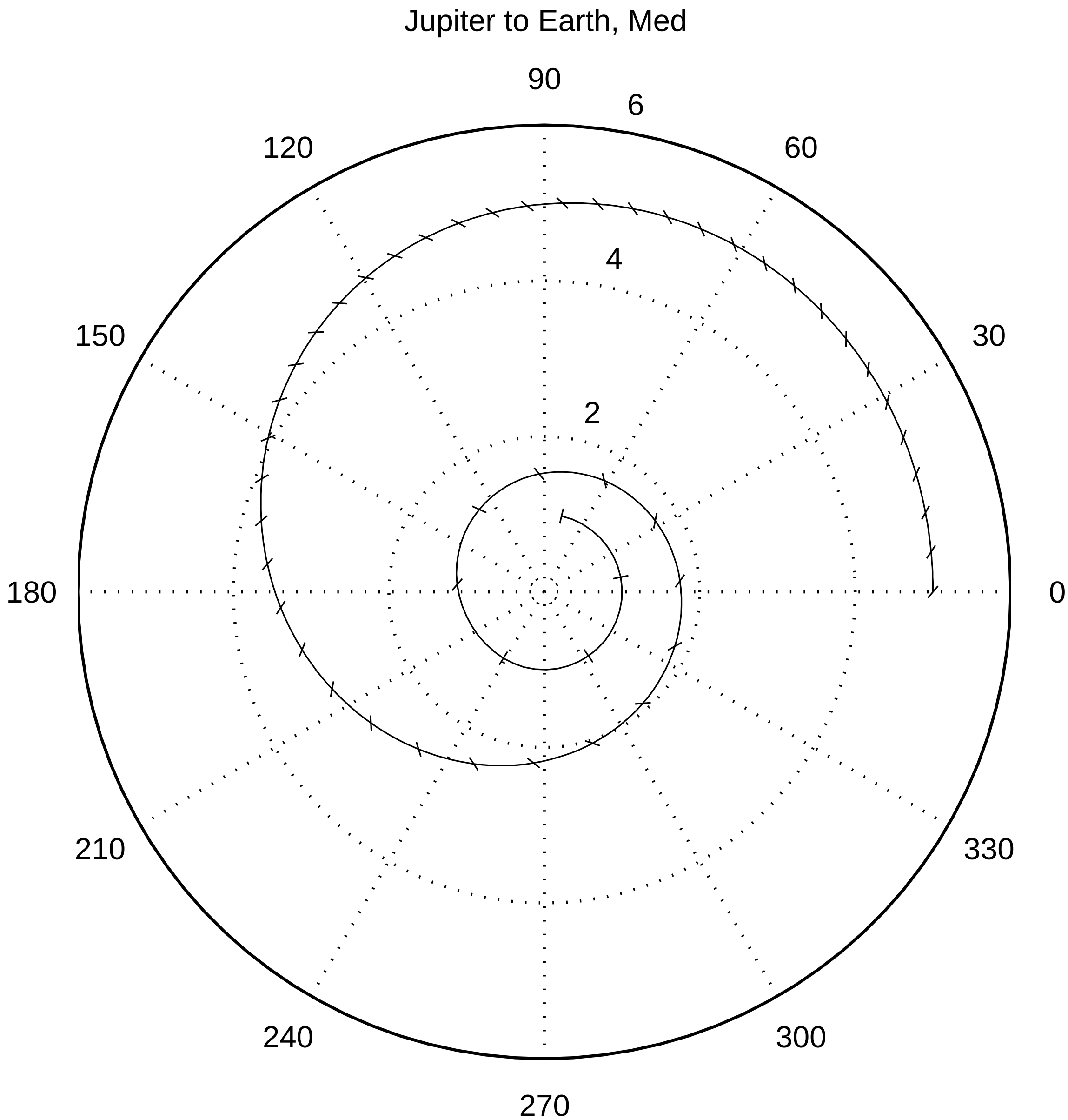


Figure 5.11: Medium performance Jupiter to Earth trajectory

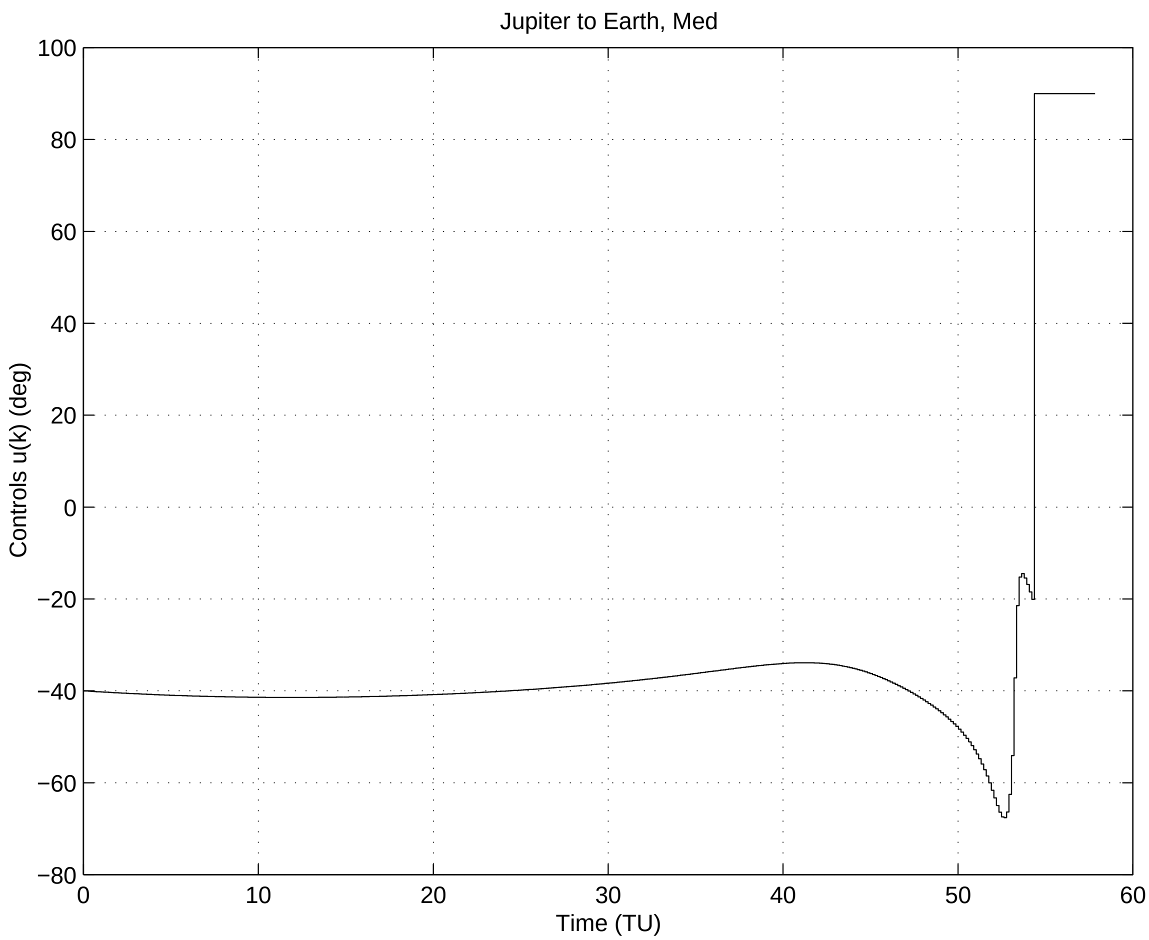


Figure 5.12: Medium performance Jupiter to Earth trajectory

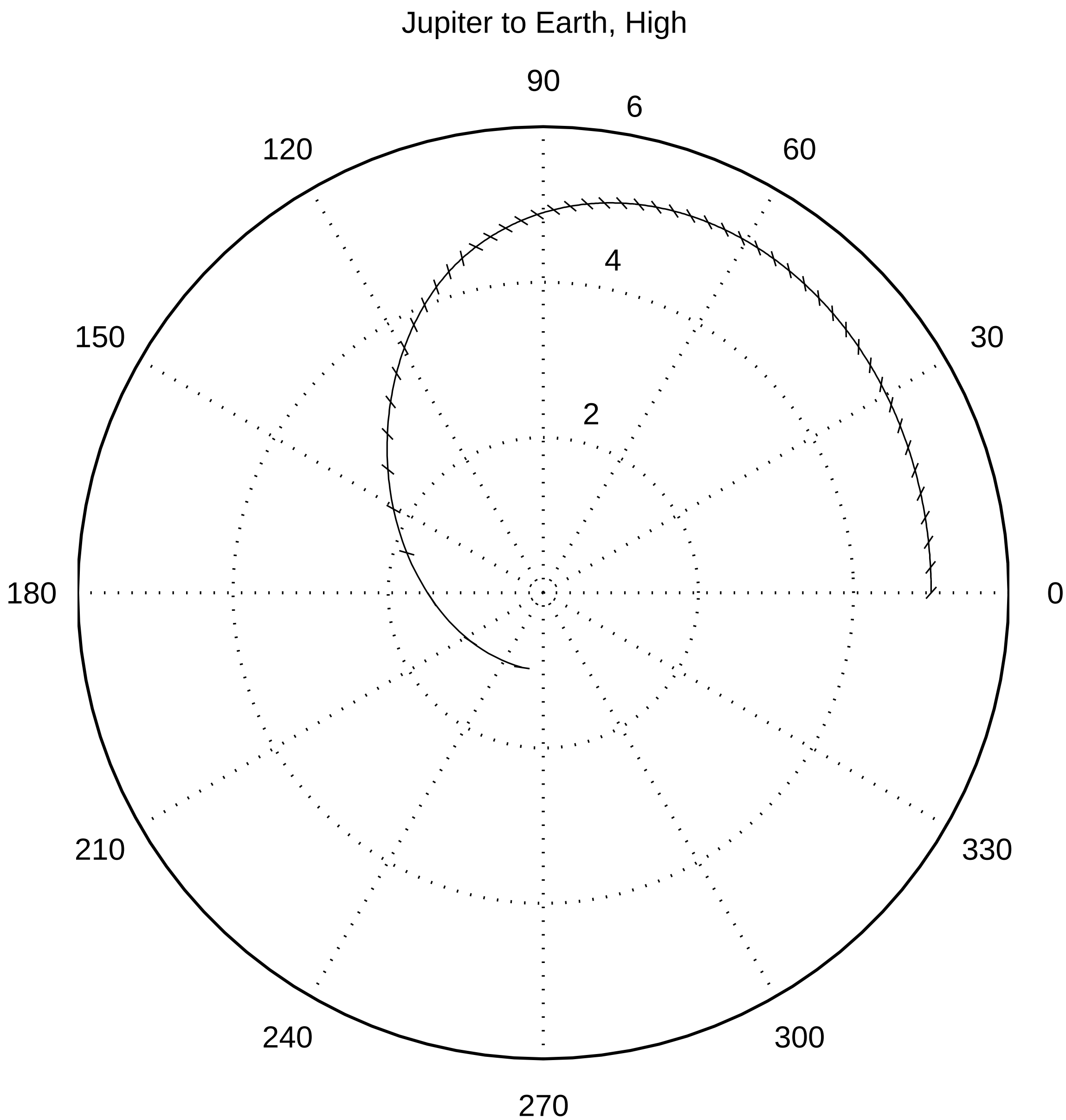


Figure 5.13: High performance Jupiter to Earth trajectory

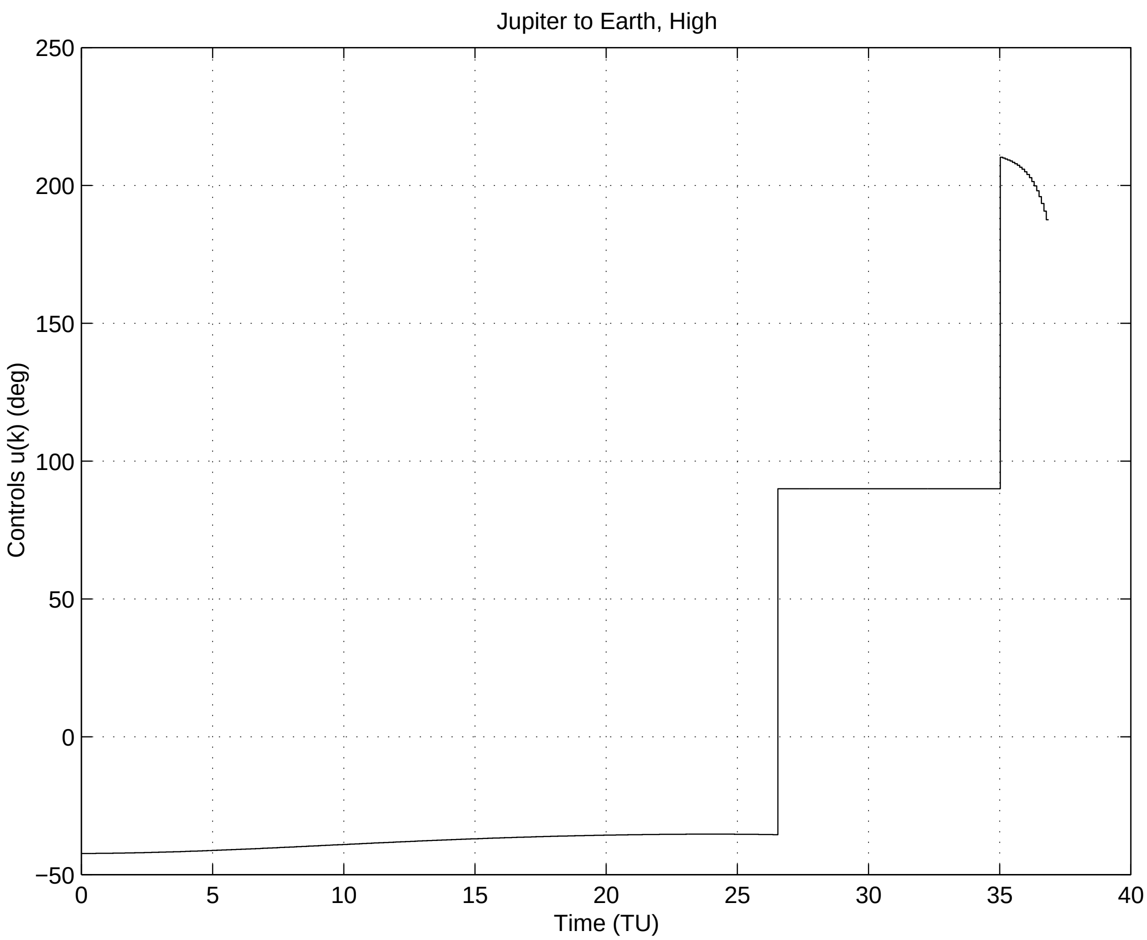


Figure 5.14: High performance Jupiter to Earth trajectory

# Chapter 6

# CONCLUSION

## 6.1 Summary of Results

A number of results were returned from this study. These may be separated into two parts. First, an approach to solar sail attitude control and dynamics modeling was presented. Second, there were a number of results regarding the unique behavior and characteristics of solar sail attitude control.

The design approach gave a sequence of steps to follow which can be followed for a variety of different problems in future work. This started in chapter 2 where the rotational dynamics of the sail were developed. Next, chapter 3 covered developing a state model and LQR attitude controller for the sail. Finally, chapters 4 and 5 present a variety of tests to evaluate solar sail performance.

Chapter 3 presented the result that the linear solar sail model is uncontrollable when the sail is edge-on to the sun.

Chapters 4 and 5 gave a variety of results from the tests they performed. One surprising result was the insensitivity of the controller to operating at sail orientation angles far from the equilibrium position about which the LQR controller was calculated. The controller was actually able to maintain the sail very close to being edge-on to the sun. The controller was also insensitive to large initial angular positions. The controller was sensitive, however, to large changes in the radius from the sun at which the LQR gain matrix was calculated. The controller's ability to respond to step inputs was severely degraded as the radius was changed. Initial angular velocities also posed a problem for the controller. Beyond a very small limit, initial angular velocities caused to system to become unstable.

Another result was the observation that the attitude control system was easily able to track optimal solar sail trajectories. This was because the time scale of the trajectories was very large compared to the time scale over which the control system was able to perform attitude maneuvers. However, there were some problems posed by the sail angle required to achieve certain trajectories, such as in Jupiter to Earth trajectories, which had periods where the sail needed to be edge-on to the sun.

In summary, the LQR method of control was able to provide effective attitude control for this solar sail model. A procedure for analysis and design was presented, and some characteristics important to the design of a solar sail attitude control system were identified.

## *6.2 Further Study*

This work was fairly limited in scope as this was a preliminary investigation. Therefore, there are a number of areas where further work is recommended.

First, the analysis and simulation were primarily performed in two dimensions. An identical study in three dimensions is very important.

The solar sail modeled was ideal, so more realistic modeling is required to identify the effect of non-ideal sail characteristics on the dynamics. A real sail has a variety of optical characteristics that will make the dynamics differ from a perfectly reflecting sail. The sail surface will be curved and not perfectly flat. There will be some uncertainties in the sail parameters due to manufacturing and imperfect sail shape after deployment. The flexible dynamics of the sail should be studied in order not to excite natural frequencies by the control system. The pressure of sunlight differs from a true inverse square law because the sun is an extended source of light and not a point source, as was assumed for this study. The sail will slowly degrade over time, which will need to be adapted to or accounted for. The state of a real sail sill need to be estimated from a set of sensors.

This study examined only one type of attitude control actuator, when there are a variety possible. One of these is the use of reflective steering vanes. Another is to shift the center of mass of a spinning sail relative to the center of pressure.

The orbital and attitude dynamics were derived under the assumption of a sail in orbit around the sun. A spacecraft in orbit around a planet or minor planet (asteroid) will be very different, because the source of gravity and sunlight will be from two completely different location, unlike with a solar orbit.

Finally, the trajectory optimization used assumed a sail capable of meeting any desired angle with respect to the sun, then sought to see if the attitude controller could meet it. Working the other way around, the trajectory optimization can be carried out with inequality constraints that limit the sail angle to those that the control system can provide.

# BIBLIOGRAPHY

[Bry99] Arthur Bryson. *Dynamic Optimization*. Addison-Wesley, 1999.

[Bur99] Jeffrey Burl. *Linear Optimal Control*. Addison-Wesley, 1999.

[Ly99a] Uy-Loi Ly. Nonlinear optimal control. University of Washington, Department of Aeronautics & Astronautics, 1999.

[Ly99b] Uy-Loi Ly. Principles of dynamics. University of Washington, Department of Aeronautics & Astronautics, 1999.

[Ly00] Uy-Loi Ly. Linear system theory. University of Washington, Department of Aeronautics & Astronautics, 2000.

[mat99] Matlab. The Mathworks, 1999. http://www.mathworks.com/.

[mat00] Mathematica. Wolfram Research, 2000. http://www.wolfram.com/.

[McI99] Colin McInnes. *Solar Sailing: Technology, Dynamics, and Mission Applications*. Springer-Praxis, 1999.

# Appendix A

# INERTIA TENSOR DERIVATION

## A.1 Physical Model

Inertia tensors are calculated for the two linked bodies which compose the solar sail spacecraft described in chapter 2, the control boom and the sail. The inertia tensors are calculated by performing triple-integrals over the volume of each part.

As was discussed in chapter 2, there is an $s$ frame for the sail and a $c$ frame for the control boom. The integrals are carried within these frames using the variables $x$, $y$, and $z$ for the $s_1$ and $c_1$, $s_2$ and $c_2$, and $s_3$ and $c_3$ directions.

The structural boom is composed of a slender boom and the payload mass at one end. The sail is composed of the square sail film and the four structural booms which support it. Each of these structures is assumed to be a rectangular solid of uniform density. Once the inertia tensors are derived for these shapes, they will be simplified by substituting out small terms like boom width, sail thickness, and payload mass width. This will be done by replacing the product of multiples of these dimensions and the volumetric density with linear boom densities, areal sail density, and payload mass. Areal density is defined as the mass of the sail film divided by the area. Linear density is defined as the mass of the boom divided by its length.

The control boom has a length of $l_b$, width and height of $g_c$, and volumetric density of $\rho_c$. The payload mass is a cube with a width of $g_p$ and density $\rho_p$. These dimensions and the $c$ frame are shown in figure A.1, along with the reference frame.

The sail has a thickness of $h$ and a volumetric density of $\rho_s$. The four structural booms each have a length of $w$, width and height of $g_b$, and a volumetric density of

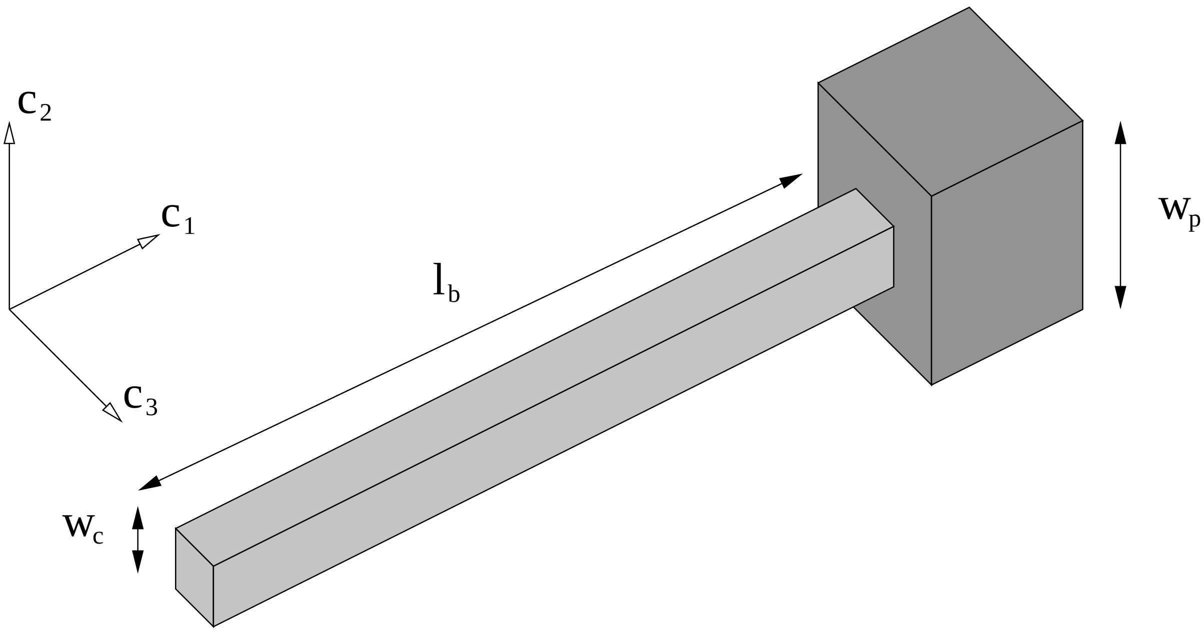


Figure A.1: Dimensions of control boom and payload

$\rho_b$. These dimensions and the $s$ frame are shown in figure A.2.

## *A.2 Integrals*

The inertia tensors are found by integrating in three dimensions over the entire volume of each of the four parts of the spacecraft - sail film, structural booms, control boom, and payload mass. These integrals are performed over limits defined by the dimensions of each part.

### *A.2.1 Sail*

*Sail Film*

The sail film integral is formed by two individual integrals over $y$ and $z$, because two continuous integrals can be carried out over two triangular halves of the sail. This integral is shown in equation A.1.

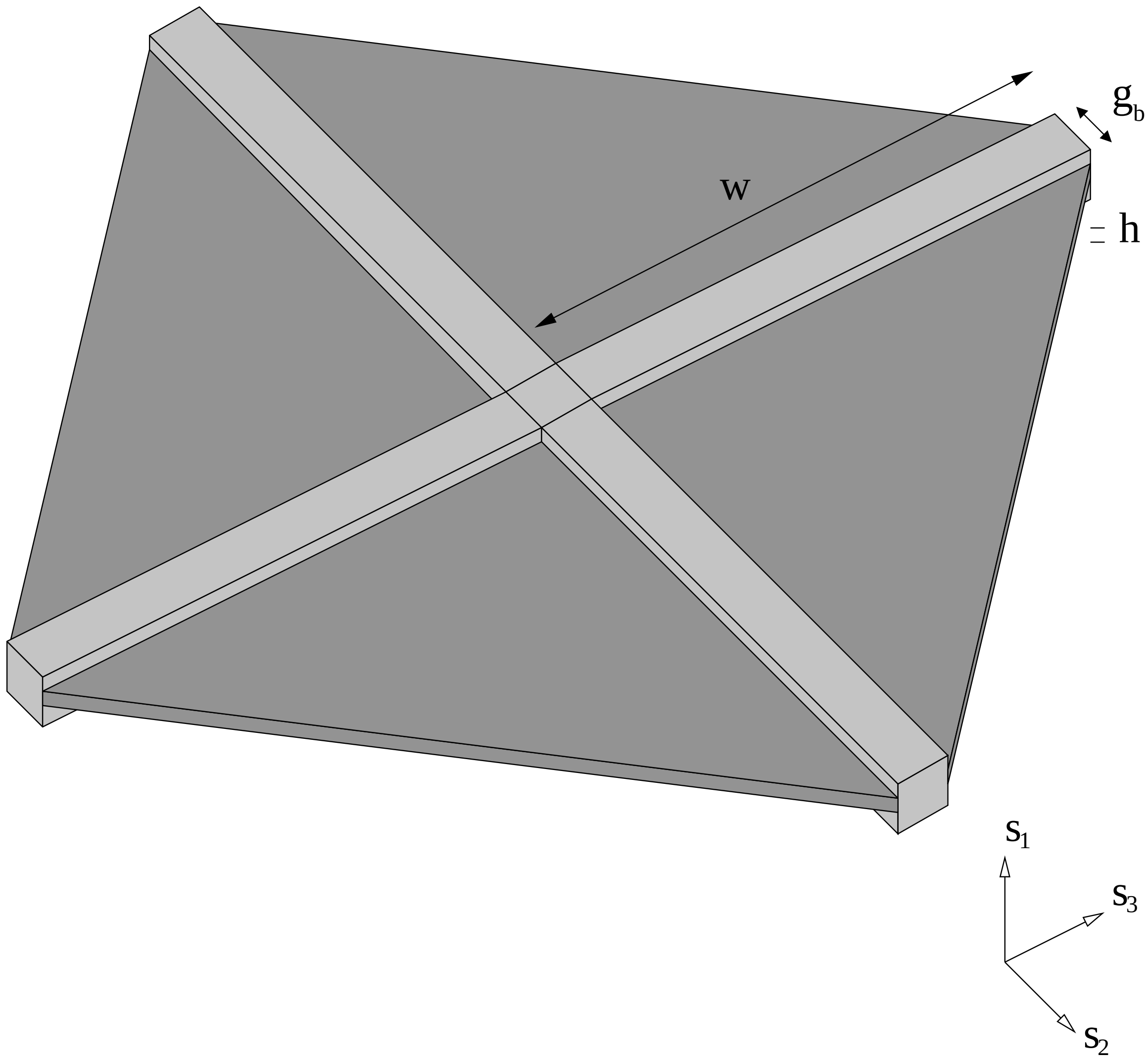


Figure A.2: Dimensions of sail film and structural booms

$$I_{s,f} = \rho_s \int_{\frac{-h}{2}}^{\frac{h}{2}} \left( \int_{-w}^{0} \int_{-z-w}^{w+z} R\, dy\, dz + \int_{w}^{0} \int_{z-w}^{w-z} R\, dy\, dz \right) dx \qquad \text{(A.1)}$$

where

$$R = \begin{bmatrix} x & y & z \end{bmatrix} \begin{bmatrix} x \\ y \\ z \end{bmatrix} I_{3\times3} - \begin{bmatrix} x \\ y \\ z \end{bmatrix} \begin{bmatrix} x & y & z \end{bmatrix}$$

*Structural Booms*

The integral for the structural booms is formed in three parts. The first integrates along the length of one boom beginning at the $-s_3$ end of the structure. The second integrates over the width of two booms. The third integrates along the length of the last boom in $+s_3$ direction. This integral is given in equation A.2. $R$ is defined the same as before.

$$\begin{aligned} I_{s,b} \;=\; & \rho_b \int_{\frac{g_b}{2}}^{\frac{-g_b}{2}} \left( \int_{-w}^{\frac{-g_b}{2}} \int_{\frac{-g_b}{2}}^{g_b/2} R\, dz\, dy + \right. \\ & \left. \int_{\frac{-g_b}{2}}^{\frac{g_b}{2}} \int_{-w}^{w} R\, dz\, dy + \int_{\frac{g_b}{2}}^{w} \int R\, dz\, dy \right) \end{aligned} \qquad \text{(A.2)}$$

### A.2.2 Control Boom

*Boom*

The integral for the boom part of the control boom is simply over the rectangular solid volume of the boom. This is shown in equation A.3. $R$ is defined as before.

$$I_{c,b} = \int_{0}^{l_b} \int_{\frac{-g_c}{2}}^{\frac{g_c}{2}} \int_{\frac{-g_c}{2}}^{\frac{g_c}{2}} R\, dz\, dy\, dx \qquad \text{(A.3)}$$

*Payload Mass*

The integral for the payload mass is simply over the cube shape, which is located at a distance $l_b$ from the origin. This is shown in equation A.4. $R$ is the same as before.

$$I_{c,p} = \int_{l_b-\frac{g_p}{2}}^{l_b+\frac{g_p}{2}} \int_{\frac{-g_p}{2}}^{\frac{g_p}{2}} \int_{\frac{-g_p}{2}}^{\frac{g_p}{2}} R\, dz\, dy\, dx \tag{A.4}$$

## A.3 Inertia Tensors

The integrals are now evaluated to produce the inertia tensor matrices. Then, they are simplified using assumptions of small boom width, sail thickness, and payload dimensions.

### *A.3.1 Sail*

*Sail Film*

The inertia tensor of the sail film is given in equation A.5.

$$I_{s,f} = \begin{bmatrix} \frac{2}{3}h\, w^4\, \rho_s & 0 & \\ 0 & \left(\frac{h^3\, w^2}{6} + \frac{h\, w^4}{3}\right) \rho_s & 0 \\ 0 & 0 & \left(\frac{h^3\, w^2}{6} + \frac{h\, w^4}{3}\right) \rho_s \end{bmatrix} \tag{A.5}$$

This can be simplified by assuming that $h$ is very small and that $h\, \rho_s = \sigma_s$, $\sigma_s$ is the areal density of the sail. Thus, $h^2$ and higher order terms can be neglected, and $h\, \rho_s$ can be replaced by $\sigma_s$. This result is shown in equation A.6.

$$I_{s,f} = \begin{bmatrix} \frac{2\, w^4\, \sigma_s}{3} & 0 & 0 \\ 0 & \frac{w^4\, \sigma_s}{3} & 0 \\ 0 & 0 & \frac{w^4\, \sigma_s}{3} \end{bmatrix} \tag{A.6}$$

*Structural Booms*

The structural boom inertia tensor is given in equation A.7.

$$I_{s,b} = \begin{bmatrix} \left(-\frac{g_b^5}{6} + \frac{g_b^4\, w}{3} + \frac{4\, g_b^2\, w^3}{3}\right)\rho_b & 0 & 0 \\ 0 & \left(-\frac{g_b^5}{6} + \frac{g_b^4\, w}{2} + \frac{2\, g_b^2\, w^3}{3}\right)\rho_b & 0 \\ 0 & 0 & \left(-\frac{g_b^5}{6} + \frac{g_b^4\, w}{2} + \frac{2\, g_b^2\, w^3}{3}\right)\rho_b \end{bmatrix} \tag{A.7}$$

This tensor can be simplified by assuming that the boom width $g_b$ is very small and that $g_b^2\,\rho_b = \sigma_b$, where $\sigma_b$ is the linear density of the control boom. This simplified inertia tensor is shown in equation A.8.

$$I_{s,b} = \begin{bmatrix} \frac{4\, w^3\, \sigma_b}{3} & 0 & 0 \\ 0 & \frac{2\, w^3\, \sigma_b}{3} & 0 \\ 0 & 0 & \frac{2\, w^3\, \sigma_b}{3} \end{bmatrix} \tag{A.8}$$

*Total*

The total inertia tensor for the sail is the sum of the sail film and structural boom tensors, given in equation A.9.

$$I_s = \begin{bmatrix} \frac{2}{3}w^4\sigma_s + \frac{4}{3}w^3\sigma_b & 0 & 0 \\ 0 & \frac{1}{3}w^4\sigma_s + \frac{2}{3}w^3\sigma_b & 0 \\ 0 & 0 & \frac{1}{3}w^4\sigma_s + \frac{2}{3}w^3\sigma_b \end{bmatrix} \tag{A.9}$$

### *A.3.2 Control Boom*

*Boom*

The inertia tensor for the boom portion of the control boom is given in equation A.10.

$$I_{c,b} = \begin{bmatrix} \frac{g_c^4\, l_b\, \rho_c}{6} & 0 & 0 \\ 0 & \left(\frac{g_c^4\, l_b}{12} + \frac{g_c^2\, l_b^3}{3}\right)\rho_c & 0 \\ 0 & 0 & \left(\frac{g_c^4\, l_b}{12} + \frac{g_c^2\, l_b^3}{3}\right)\rho_c \end{bmatrix} \tag{A.10}$$

This tensor is simplified by assuming that the boom width $g_c$ is small and that $g_c^2\,\rho_c = \sigma_c$ where $\sigma_c$ is the linear density of the boom. The result is given in equation A.11.

$$I_{c,b} = \begin{bmatrix} 0 & 0 & \\ 0 & \frac{l_c^3\,\sigma_c}{3} & 0 \\ 0 & 0 & \frac{l_c^3\,\sigma_c}{3} \end{bmatrix} \tag{A.11}$$

*Payload Mass*

The payload mass inertia tensor is given in equation A.12.

$$I_{c,p} = \begin{bmatrix} \frac{g_p^5\,\rho_p}{6} & 0 & 0 \\ 0 & \left(\frac{g_p^5}{6} + g_p^3\,l_b^2\right)\rho_p & 0 \\ 0 & 0 & \left(\frac{g_p^5}{6} + g_p^3\,l_b^2\right)\rho_p \end{bmatrix} \tag{A.12}$$

This is simplified by assuming that the width of the payload mass cube $g_p$ is small and $g_p^3\,\rho_p = m_p$, the payload mass. This result is given in equation A.13.

$$I_{c,p} = \begin{bmatrix} 0 & 0 & \\ 0 & l_b^2\,m_p & 0 \\ 0 & 0 & l_b^2\,m_p \end{bmatrix} \tag{A.13}$$

*Total*

The total control boom inertia tensor is the sum of the boom and payload mass tensors, which is given in equation A.14.

$$I_c = \begin{bmatrix} 0 & 0 & \\ 0 & l_b^2\,m_p + \frac{l_b^3\,\sigma_c}{3} & 0 \\ 0 & 0 & l_b^2\,m_p + \frac{l_b^3\,\sigma_c}{3} \end{bmatrix} \tag{A.14}$$

# Appendix B

# ORBITAL DYNAMICS

## B.1 Introduction

The orbital dynamics of a solar sail in orbit around the sun (heliocentric) are now developed. Newtonian dynamics are used to derive polar equations of motion of a solar sail, given initial conditions and the angular position of the sail with respect to the incident as a control input. This is the same angle, $\varphi_s(t)$, that a controller was developed for in chapter 3.

## B.2 Coordinate System

An inertial reference frame, called $E$, is centered at the center of the solar system. The sun is assumed to be co-incident with this location, so that the source of gravity and sunlight acting on the sail is centered at this point. A polar rotating reference frame, called $e$, is used to describe the position of the sail in the solar system.

The inertial reference frame is composed of the unit vectors shown in equation B.1.

$$E = (E_1, E_2, E_3) \tag{B.1}$$

The polar reference frame is shown in equation B.2. It is composed of three unit vectors, plus an angular velocity representing its rotation.

$$e = (e_1, e_2, e_2, \vec{\omega}_e(t)) \tag{B.2}$$

These reference frames are shown in figure B.1. The polar reference frame is

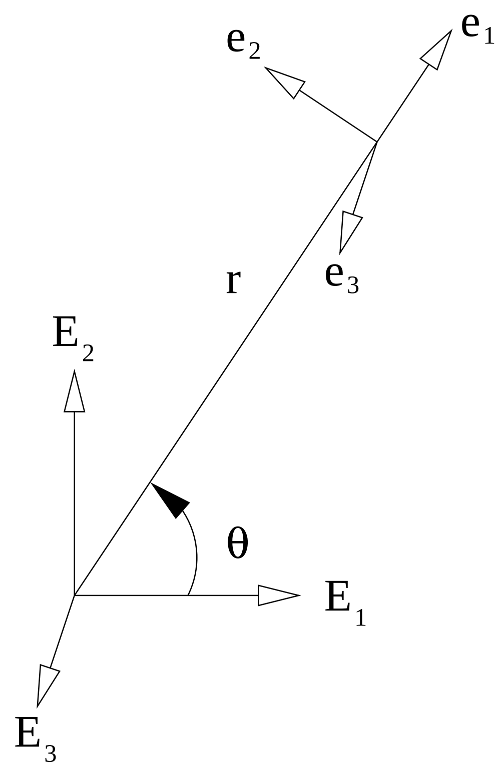


Figure B.1: 2D orbital dynamics reference frames

related to the inertial frame by the polar coordinates $r(t)$ and $\theta(t)$. Also, this gives the angular velocity of the polar frame, $\vec{\omega}_e(t)$, which is shown in equation B.3.

$$\vec{\omega}_e(t) = \dot{\theta}(t)\; E_3 = \dot{\theta}(t)\; e_3 \tag{B.3}$$

The transformation matrix between $E$ and $e$, $C_e$, is found from $\theta(t)$. A vector expressed in the $E$ frame, $\vec{r}_E$, is converted into a vector in the $e$ frame, $\vec{r}_e$, by the operation $\vec{r}_e = C_e\, \vec{r}_E$. $C_e$ is given in equation B.4.

$$C_e = \begin{bmatrix} \cos\theta & \sin\theta & 0 \\ -\sin\theta & cos\theta & 0 \\ 0 & 0 & 1 \end{bmatrix} \tag{B.4}$$

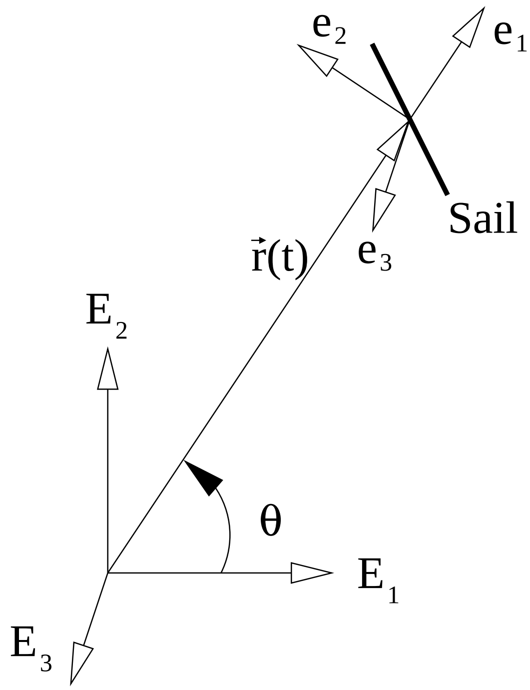


Figure B.2: 2D heliocentric position vector of solar sail

### B.3 Position Vector

The position vector of the solar sail spacecraft, $\vec{r}(t)$, is shown in figure B.2. Equation B.5 shows $\vec{r}(t)$ in polar coordinates.

$$\vec{r}(t) = r(t)\, e_1 \tag{B.5}$$

### B.4 Velocity Vector

The velocity vector, $\vec{v}(t)$, is found by taking the time derivative of the position, which is shown in equation B.6 Note that because the $e$ frame is rotating, the derivative of any unit vector in $e$ is the cross product of $\vec{\omega}(t)$ and that unit vector.

$$
\begin{aligned}
\vec{v}(t) &= \frac{d}{dt}\vec{r}(t) \\
&= \dot{r}\, e_1 + r\, \vec{\omega}_e(t) \times e_1 \\
&= \dot{r}\, e_1 + r\, \dot{\theta}\, e_3 \times e_1 \\
&= \dot{r}\, e_1 + r\, \dot{\theta}\, e_2 \qquad \text{(B.6)}
\end{aligned}
$$

### B.5 Acceleration Vector

The acceleration vector, $\vec{a}(t)$, is the time derivative of $\vec{v}(t)$. This is shown in equation B.7. Note that $r$, $\theta$, and their derivatives are all functions of time. The $(t)$ notation has been left off to make the equations less cumbersome.

$$
\begin{aligned}
\vec{a}(t) &= \frac{d}{dt}\vec{v}(t) \\
&= \ddot{r}\, e_1 + \dot{r}\, \vec{\omega}(t) \times e_1 + \dot{r}\, \dot{\theta}\, e_2 + r\, \ddot{\theta}\, e_2 + r\, \dot{\theta}\, \vec{\omega}(t) \times e_2 \\
&= \ddot{r}\, e_1 + \dot{r}\, \dot{\theta}\, e_2 + \dot{r}\, \dot{\theta}\, e_2 + r\, \ddot{\theta}\, e_2 - r\, \dot{\theta}^2\, e_1 \\
&= \left(\ddot{r} - r\, \dot{\theta}^2\right) e_1 + \left(2\, \dot{r}\, \dot{\theta} + r\, \ddot{\theta}\right) e_2 \qquad \text{(B.7)}
\end{aligned}
$$

The 2nd order derivatives of $r$ and $\theta$ can be eliminated by introducing two new variables representing the radial velocity, $v_r$, and the tangential velocity, $v_\theta$. These velocities are given by equations B.8 and B.9. The derivatives of these velocities are given by equations B.10 and B.11.

$$
\begin{aligned}
v_r &= \dot{r} \qquad \text{(B.8)} \\
v_\theta &= r\, \dot{\theta} \qquad \text{(B.9)} \\
\dot{v}_r &= \ddot{r} \qquad \text{(B.10)} \\
\dot{v}_\theta &= \dot{r}\, \dot{\theta} + r\, \ddot{\theta} \qquad \text{(B.11)}
\end{aligned}
$$

These substitutions provide a state vector for representing the solar sail as given in equation B.12.

$$\vec{x}(t) = \begin{bmatrix} r \\ \theta \\ v_r \\ v_\theta \end{bmatrix} \tag{B.12}$$

These velocities and their derivatives can be substituted into the acceleration so that only first order derivatives are present. This result is given in equation B.13.

$$\vec{a}(t) = \left(\dot{v}_r - \frac{v_\theta^2}{r}\right) e_1 + \left(\frac{v_r\, v_\theta}{r} + \dot{v}_\theta\right) e_2 \tag{B.13}$$

## *B.6 Free Body Diagram*

The free body diagram of the solar sail is shown in figure B.3. Gravity, $\vec{F}_g$, and solar radiation pressure, $\vec{F}_r$, are the two forces acting on the sail. $\vec{F}_r$ depends on the sail orientation angle, $\varphi_s$, which functions as a control input to this problem. These are the same forces that were calculated in section 2.4.5. They are given in equations B.14 and B.15.

$$\vec{F}_g(t) = -\frac{\mu_s\, m_s}{r^2}\, e_1 \tag{B.14}$$

$$\vec{F}_r(t) = \frac{\beta\, \mu_s\, m_s}{r^2} \cos^3 \varphi_s\, e_1 + \frac{\beta\, \mu_s\, m_s}{r^2} \cos^2 \varphi_s \sin \varphi_s\, e_2 \tag{B.15}$$

## *B.7 Newton's Third Law*

Next, Newton's third law is used to combine the acceleration and force vectors. The law is given in equation B.16. The combination of forces and accelerations for this problem are given in equation B.17.

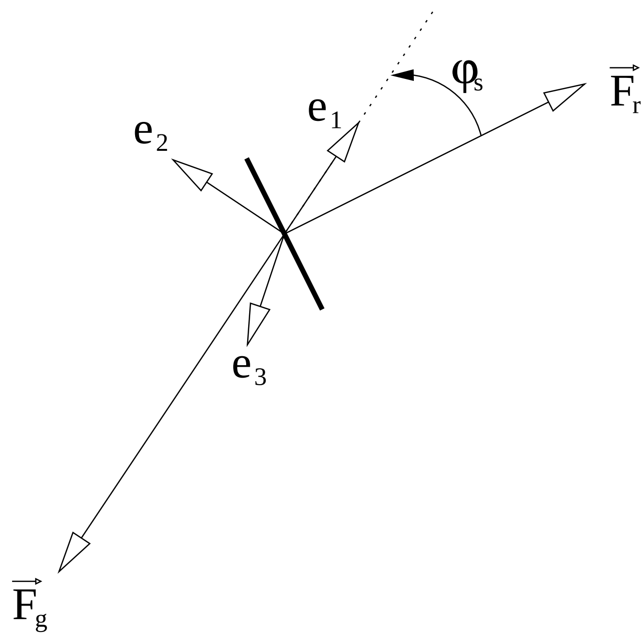


Figure B.3: 2D orbital dynamics free body diagram.

$$\sum \vec{F} = m\,\vec{a} \tag{B.16}$$

$$\begin{aligned} \frac{\beta\,\mu_s\,m_s}{r^2}\cos^3\varphi_s\,e_1 + \ldots & \\ \ldots + \frac{\beta\,\mu_s\,m_s}{r^2}\cos^2\varphi_s\sin\varphi_s\,e_2 + \ldots & \\ \ldots - \frac{\mu_s\,m_s}{r^2}\,e_1 &= \left(\dot{v}_r - \frac{v_\theta^2}{r}\right)e_1 + \ldots \\ & \ldots + \left(\frac{v_r\,v_\theta}{r} + \dot{v}_\theta\right)e_2 \end{aligned} \tag{B.17}$$

## B.8 Equations of Motion

Finally, a set of differential equations are found for each of the state variables–$r$, $\theta$, $v_r$, and $v_\theta$. The differential equations for $r$ and $\theta$ are found from equations B.8 and B.9.

The differential equations for $v_r$ and $v_\theta$ are found by splitting the vector equation B.17 into two scalar equations, then solving for $\dot{v}_r$ and $\dot{v}_\theta$.

The equations of motion are then given by equations B.18, B.19, B.20, and B.21.

$$\dot{r} = v_r \tag{B.18}$$

$$\dot{\theta} = \frac{v_\theta}{r} \tag{B.19}$$

$$\dot{v}_r = \frac{v_\theta^2}{r} + \frac{\mu_s}{r^2}\left(\beta \cos^3 \varphi_s - 1\right) \tag{B.20}$$

$$\dot{v}_\theta = \frac{\mu_s}{r^2}\beta \cos^2 \varphi_s \sin \varphi_s - \frac{v_r\, v_\theta}{r} \tag{B.21}$$

# Appendix C

# OPTIMAL TRAJECTORIES

## *C.1 Introduction*

This appendix briefly describes the procedure used to calculate the optimal trajectories. The technique for discrete dynamic optimization with terminal equality constraints and open final time described in [Ly99a] was used to carry out the optimization. This technique, as it was used for the solar sail trajectory optimization, is described in this chapter.

These trajectories are found using the dynamics derived in appendix B. The optimization is carried out to find the time history of the control input to the dynamics–the sail angle with respect to the incident sunlight–which gives the minimum time to transfer from one set of state values–the initial orbit–to a final set of state values–the destination orbit. As is discussed in chapter 5, the initial and final state vectors correspond to circular orbits located the mean orbital radii of Earth, Mars, Venus, and Jupiter.

The states of the dynamics, $\vec{x}$, are given in equation B.12. This is $\vec{x} = [\, r \quad \theta \quad v_r \quad v_\theta \,]^T$.

The continuous dynamic equations, given in equations B.18 to B.21, can be put into the form of a discrete vector, $\vec{f}(\vec{x}(k), u(k), k)$.

## *C.2 Basic Cost Function*

The problem is to find a time history of the sail angle, $u(k)$, at each time step $k = 0, 1, 2, \ldots, N-1$ to minimize the scalar cost function given in equation C.1. This is simply the time of flight between the initial and destination orbits.

$$J(u, t_f) = t_f \tag{C.1}$$

### C.3 Augmented Cost Function

The terminal equality constraints, $\vec{\psi}(\vec{x}(N), t_f) = 0$, are defined as the radius, radial velocity, and tangential velocity of the desired final orbit. These are shown in equation C.2.

$$\vec{\psi}(\vec{x}(N), t_F) = \begin{bmatrix} r(N) - r_f \\ v_r(N) \\ v_\theta(N) - v_{\theta,f} \end{bmatrix} \tag{C.2}$$

The discrete dynamic equations are formed as difference equations of the continuous dynamic equations found in equations B.18 to B.21. The continuous dynamic differential equations can be put into a vector form $\vec{f_c}(\vec{x}(t), u(k), t) = [\,\dot{r} \quad \dot{\theta} \quad \dot{v}_r \quad \dot{v}_\theta\,]$. The value of the time $t$ at each time step $k$ can be represented by $T(k)$. The discrete dynamic difference equation vector can then be formulated as $\vec{f_d}(\vec{x}(k), u(k), k) = \vec{x}(k+1) = \vec{x}(k) + \Delta T \vec{f_c}(\vec{x}(T(k)))$. $\Delta T$ is the time step size of the problem, for which an optimal value is found in addition to the control input, u(k). The difference equations are given in equation C.3.

$$\vec{f_d}(\vec{x}(k), u(k), k) = \begin{bmatrix} r(k) + \Delta T\, v_r(k) \\ \theta(k) + \Delta T \frac{v_\theta(k)}{r(k)} \\ v_r(k) + \Delta T \left[ \frac{v_\theta^2(k)}{r(k)} + \frac{\mu_s}{r^2(k)} \left( \beta \cos^3 u(k) - 1 \right) \right] \\ v_\theta(k) + \Delta T \left[ \frac{\mu_s}{r^2(k)} \beta \cos^2 u(k) \sin u(k) - \frac{v_r(k)\, v_\theta(k)}{r(k)} \right] \end{bmatrix} \tag{C.3}$$

The cost function $J$ is augmented with the terminal constraints and discrete dynamic difference equations using Lagrange multipliers. A scalar Lagrange multiplier vector $\nu$ is used for the terminal constraints, and a time varying vector $\vec{\lambda}(k)$ is used for the difference equations. The final augmented cost function can then be expressed by equation C.4.

$$\begin{aligned}\bar{J}(u, tf, \vec{x}_0) \quad = \quad & \phi(\vec{x}(N), t_f) + \\ & \vec{\nu}^T \vec{\psi}(\vec{x}(N), t_f) + \\ & \sum_{k=0}^{N-1} \vec{\lambda}^T(k+1) \left[ \vec{f}_d(\vec{x}(k), u(k), k) - \vec{x}(k+1) \right] + \\ & \vec{\lambda}^T(0) \left[ \vec{x}_0 - \vec{x}(0) \right] \end{aligned} \tag{C.4}$$

## *C.4 Conclusion*

This cost function can then be used with any appropriate optimization method–such as the gradient methods described in [Ly99a] and [Bry99]–to find and control input time history that will minimize the time of flight of a solar sail between any two circular, coplanar orbits around the sun.